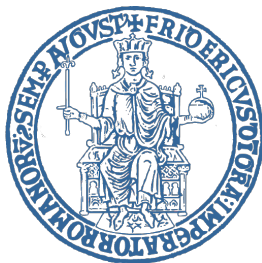# UNIVERSITY OF NAPLES "FEDERICO II"

Faculty of Maths, Physics and Natural Sciences
Department of Physics "E. Pancini"

PhD Thesis in Physics
XXXIII Cycle
Coordinator: Prof. S. Capozziello

Development of novel nano-structured materials for Enhanced Raman Spectroscopies: an insight in SERS and TERS applications

Tutors
Prof. Giulia Rusciano
Prof. Antonio Sasso

Candidate
Angela Capaccio

Academic Year: 2018/2021
SDS: FIS/03

...to my dear family,
to my beloved Alessandro,
for their patience, support and endless love...

Contents

Motivation and Objectives

The label-free detection of low-concentration analytes in complex biological environments is of relevant importance in many practical applications. In various cellular biological processes is essential to monitor in real time the structural and/or physical changes at molecular level induced by external stimulations. As a matter of fact, the selective extraction of the molecular dynamic information can contribute to a better understanding of the nature of cell functions and the pathogenesis of diseases. Owing to their ultrahigh selectivity and sensitivity, the plasmon-enhanced Raman spectroscopies (PERS) methods have emerged as diverse and exciting cutting-edge techniques for the investigation of biosystems at nanometric scales in air or water environments. On one hand, compared to other vibrational techniques, the Raman spectroscopy offers a rapid and high-throughput molecular selectivity thanks to its characteristic chemical "fingerprint" with minimal water interference, which is a great advantage for the analysis of the biological samples. On the other hand, the plasmonic properties of noble metal nanoparticles enable the PERS methods to remove the main obstacle of the Raman spectroscopy represented by the small Raman cross section ($\sim 10^{-30}$ $cm^2/molec$). The first observation that the Raman signal of molecules was extremely increased when adsorbed on roughened silver surfaces is due to Fleischmann *et al.*[1] in 1974, to whom we owe the birth of the surface-enhanced Raman spectroscopy (SERS). One of the interesting features of the SERS is that the huge amplification of inelastic Raman photons can reach up to 12 orders of magnitude allowing even the detection at single-molecule level. In addition, the strong distance dependence of the

plasmonic near-field effect (~ 10-20 *nm*) make effective the SERS only for molecules in proximity to the metal surface and, thus, suitable not only for the bio-analysis of membranes but also for the surface characterization in science materials.

Anyway, beyond the high sensitivity, the spatial resolution of SERS is diffracted-limited, i.e. of the order of ~ 250 *nm* (Abbe limit for green light) which is small compared to most biological cells (1 *μm* to 100 *μm*) but large compared to proteins or less complex molecules (< 10 *nm*). A significant improvement to the diffraction-limited spatial resolution of SERS is given by the tip-enhanced Raman spectroscopy (TERS). By combining the high resolution of scanning-probe microscope (SPM) technology and the sensitivity of SERS, TERS is capable to correlate topographical and chemical information of a sample at nanoscale level. In fact, the Raman signal coming from the probed molecules is strongly enhanced via SERS effect when they are in proximity of the apex of a metallized or metallic SPM tips. The spatial resolution of TERS signals is mainly ruled by the tip-radius, which is typically of few tens of nanometers, therefore allowing to reach lateral resolution in the range of 10-50 *nm*, far beyond the diffraction limit. The TERS technique overturns the paradigm of the SERS technique: the hot-spots located in the various sites of a SERS substrate are now localized at the apex of the TERS tip which behaves like a real nano-antenna. In particular, the characteristics of the tip, such as material, size and morphology, play a significant role for both field amplification and spatial resolution. Therefore, significant experimental and theoretical efforts have been directed to the development of cost-effective and highly sensitive plasmonic tips.

In this frame, the current thesis work aims to present an effective and simple method to develop adequate tips for TERS applications. Nowadays, the most used processes for the production of active TERS tips consist in applying a controlled electrochemical etching to the metal wires (mainly for STM-based TERS), or in binding plasmonic nanoparticles (NPs) to commercial tips. For AFM-based TERS, tips are also produced by metal coating AFM tips by sputtering/vapor deposition. The most of these methods,

however, do not always ensure optimal control on the size and repro-ducibility of the tips. Moreover, simple metal coating produces rather smooth tips, which result less performant in terms of the Enhancement Factor (EF). Herein, we explore an innovative method able to induce a thin texture in a *Ag*-film covering the TERS tip. The physics of this process is not yet fully understood also by looking at the recent literature. We attempt to explain the mechanism by assuming that the thin metal film behaves as a metastable structure and in presence of external perturbation, it can give rise to a complex mechanism that destabilizes the metallic layer and lead to a nano-structured pattern (spinodal solid-state dewetting). In our case, the external perturbation is represented by an inductively coupled plasma (ICP) produced by a radio-frequency (RF) discharge in synthetic air-atmosphere. Atomic oxygen present in the feeding gas produces oxida-tion of the outer part of the *Ag*-film and the different diffusivity of oxides and metal can create breaking and vacancies inside the oxide-metal layer (Kirkendall effect). All these mechanisms determine a very porous mor-phology that resembles to a *coral-like* structure. The so-produced probes have shown an amplification up to 10^6 and a spatial resolution down to 10 *nm*, which render these devices particularly attractive for nanometer chemical characterization. In addition, this method has been successfully implemented for the fabrication of broad-band SERS-active platforms. Our protocol have shown to be effective to produce substrates with EF of the order of 10^7. Finally, another method for the fabrication of SERS substrates, based on the self-assembly of block copolymer (BCP) loaded with *Ag*-NPs, is proposed. The sensitivity of the so-prepared substrates has been tested by revealing the over-expression of target proteins in membranes of cancer cells.

The thesis is composed as follows:

- The Chapters 1 and 2 concern a theoretical introduction to the Raman spectroscopy and the SERS/TERS mechanisms, respectively;

- The Chapter 3 describes the instrumentation and important proce-dures used throughout the work;

- The Chapter 4 is focused on the fabrication of TERS probes through the ICP treatment;

- In the Chapter 5, the method described in the Chapter 4 is implemented for the fabrication of SERS substrates;

- The Chapter 6 describes a different method for the preparation of SERS substrate and report a SERS sensing application.

Chapter 1

Fundamentals of the Raman Spectroscopy

1.1 Introduction

Since being found in the 1928 by C.V. Raman and K. Krishnan [2, 3], the Raman effect has been widely studied and employed for the development of the advanced spectroscopic techniques. The phenomenon is based on the inelastic scattering of the light by molecules. When a molecule scatters the incoming light, most of the outgoing radiation is scattered elastically at the same energy (*i.e.* frequency) of the incident one, giving rise to the so-called Rayleigh scattering. A small fraction of the incident light is, instead, scattered inelastically at a frequency that is shifted with respect to the incoming one: this process is known as Raman scattering. The various frequency shifts are associated to the different vibrational modes of the molecule and give rise to the Raman spectrum. Thus, since the molecular vibrations are distinct for every molecule, the Raman spectrum represents the chemical fingerprint of a specific compound. That's why the Raman spectroscopy is referred as a "fingerprint" spectroscopic technique.

The Raman spectroscopy is often compared to another complementary vibrational method noted as the infra-red (IR) absorption spectroscopy. Following the Beer-Lambert law, the IR spectroscopy measures the ab-

sorption spectrum of the samples when irradiated by IR radiation (the IR wavelengths range from 0.8 to 10^3 *μm*). In the Raman spectroscopy, the vibrational motion of the molecule induces a change in its polarizability. Whereas, in the IR spectroscopy, when the incident frequency matches the vibrational frequency of the molecule, the IR radiation causes a net change in its electric dipole moment. As result, some vibrational modes will be only Raman-active and others only IR-active. An example is given by the molecules with a center of simmetry that are Raman-active (mutual exclusion rule) and, thus, detectable only by Raman spectroscopy [4, 5].

The vibrational spectroscopy is used for the qualitative and quantitative analysis of inorganic, organic and biological samples in different research areas such as chemistry, biology, material and life sciences [6, 7]. However, the large IR absorption cross-section of the water strongly limits the application of IR spectroscopy for biological samples. On the contrary, the Raman spectra are free from the water background influence due to its low scattering cross-section. This renders the Raman spectroscopy a perfect candidate for in vivo label-free investigations at molecular level [8]. As a matter of facts, the Raman approach does not require any particular pre-treatment for the study of the living cells and tissues, thereby making it a label-free technique. Nevertheless, the fluorescent labels [9] or aptamers [10] are often carefully used in Raman spectroscopy to support the localisation of specific areas of the sample. Other advantages of the Raman spectroscopy for life science investigation are related to the fact that it's non-disruptive, can be performed under any sample environment and, of course, is quantitative because the scattering intensity is proportional to the number of the scatters [11]. Finally, compared to the IR absorption spectroscopy, the Raman spectroscopy can be performed by combining a confocal microscopy to the Raman spectrometer allowing the Raman imaging with sub-micron resolution [12].

Anyway, one of the main drawback of Raman spectroscopy is the poor efficiency of the Raman effect: when the light interacts with the material, only a small fraction of the scatterd photons are inelastically scatterd (about $1 : 10^6$). Furthermore, for some molecular systems the quantum yield for

the generation of fluorescence can be high enough to overcome the weak Raman signal [13]. The Raman scattering cross sections are of the order of 10^{-30} *cm²* compared to the fluorescence cross section that reaches 10^{-16} *cm²* [14].

To overcome these limitations and improve the sensitivity of the Raman scattering, several Raman signal-enhancing techniques have been developed in last years. These methods include the resonance Raman effect, non-linear Raman effects and the plasmon-enhanced Raman effect [15–17]. In this chapter will be briefly discussed the basis of the spontaneous Raman scattering and some of its variants. The next chapter, instead, will be focused on the plasmon-enhanced Raman spectroscopies that play the central role in this work thesis.

1.2 Spontaneous Raman Scattering

The complete description and fundamental theory of the Raman effect has been extensively discussed in literature and can be found in details in many textbooks [18, 19]. Herein, the classical and quantum theories are introduced to explain the origin of the Raman effect. In both the descriptions the scattered radiation arises from the oscillating electric and magnetic multipole moments induced in a molecule when irradiated by the electromagnetic field. Anyway, the main contribution to the light scattering is due to the oscillating dipole moment for which the intensity is several order of magnitude greater with respect to the others multipole moments. So, the interaction light-matter induce an electric dipole moment $\mathbf{p}^{ind}$ proportional to the incident electric field $\mathbf{E}$. If the interaction between the molecule and the electric field $\mathbf{E}$ is weak, $\mathbf{p}^{ind}$ can be expanded in Taylor series about $\mathbf{E}$ as follows:

$$\mathbf{p}^{ind} = \mathbf{p}^{(1)} + \mathbf{p}^{(2)} + ... =$$
$$= \alpha\mathbf{E} + \frac{1}{2}\beta\mathbf{E}\mathbf{E} + ... \tag{1.1}$$

where α and β are, respectively, the polarizability and hyper-polarizability tensors. For the simple description of the origin of the Raman and Rayleigh scattering, we can consider only the linear term in **E** neglecting the non-linear terms which are involved in higher-order scattering processes [13, 20]. Let's apply an oscillating electric field $\mathbf{E} = \mathbf{E}_0 cos(\omega_0 t)$ of frequency ω_0 to a neutral molecule (with no permanent electric dipole momentum). As result, the linear term of electric dipole moment in Eq. 1.2 can be explicited as:

$$\begin{aligned}
\mathbf{p}^{(1)} &= \alpha\mathbf{E} \\
&= \alpha\mathbf{E}_0 cos(\omega_0 t)
\end{aligned} \tag{1.2}$$

The polarizability tensor α is, in general, dependent from the nuclear coordinates and any nuclear motion can, in principle, modify the polarizability. Supposing that the nuclei are free to vibrate while rotations are freezed and the molecule is space-fixed in the equilibrium configuration, the variation of polarizability with vibrations of the molecule can be expressed by expanding each term $\alpha_{\rho\sigma}$ of the tensor α in Taylor series with respect to the equilibrium nuclear configuration (indicated with the subscript '0'):

$$\alpha_{\rho\sigma} = (\alpha_{\rho\sigma})_0 + \sum_{k=1}^{M}\left(\frac{\partial\alpha_{\rho\sigma}}{\partial Q_k}\right)_0 Q_k + ... \tag{1.3}$$

where Q_k is the normal coordinate correlated to the vibrational frequencies ω_k. The Eq. 1.3 can be reformulated as:

$$(\alpha_{\rho\sigma})_k = (\alpha_{\rho\sigma})_0 + (\alpha'_{\rho\sigma})_k Q_k \tag{1.4}$$

where $(\alpha'_{\rho\sigma})_k = \left(\frac{\partial\alpha_{\rho\sigma}}{\partial Q_k}\right)_0$ are the components of a new tensor α'_k, called Raman tensor [21]. This formulation is valid for all the components and we may, simply, rewrite the Eq. 1.4 as:

$$\alpha_k = \alpha_0 + \alpha'_k Q_k \tag{1.5}$$

A generic time dependence of the normal coordinate Q_k can be expressed as:

$$Q_k = Q_{k_0} cos(\omega_k t + \phi_k) \tag{1.6}$$

where Q_{k_0} is the equilibrium normal coordinate and ϕ_k an arbitrary phase. Combining the Eq. 1.2, 1.5 and 1.6, we obtain the resulting linear term of the electric dipole moment:

$$\mathbf{p}^{(1)} = \alpha_0 \mathbf{E}_0 cos(\omega_0 t) + \alpha'_k Q_{k_0} cos(\omega_k t + \phi_k) \mathbf{E}_0 cos(\omega_0 t)$$

$$= \underbrace{\alpha_0 \mathbf{E}_0 cos(\omega_0 t)}_{1} + \underbrace{\frac{1}{2} \alpha'_k Q_{k_0} \mathbf{E}_0 \{cos[(\omega_0 + \omega_k) + \phi_k] + cos[(\omega_0 - \omega_k) + \phi_k]\}}_{2}$$

$$\tag{1.7}$$

This expression contains the two main contributions to the scattered light:

1. The first term gives rise to light scattered at same frequency and phase with respect to the incident radiation (Rayleigh scattering);

2. The second term corresponds to Raman radiation that is shifted in frequency from the frequency of the incident radiation: the frequencies $\omega_0 - \omega_k$ and $\omega_0 + \omega_k$ give rise to Stokes and anti-Stokes Raman scattering, respectively.

The Eq. 1.7 implies that the Raman effect is possible only if α'_k is non-zero. The vibrational mode $\mathbf{Q}_k$ that induces the polarizability change is called Raman-active mode. The Stokes-Raman scattering intensity can be estimated by expressing the total power emitted by a Hertzian dipole [15]:

$$I_{Stokes} \propto \left[\frac{\partial \alpha}{\partial Q_k} \right]_0^2 (\omega_0 - \omega_k)^4 I_0 \tag{1.8}$$

This expression is useful to highlight the dependence of the signal intensity from the square of the Raman tensor, the intensity of the incident radiation I_0 and the 4th-power of the frequency of the scattered light. However, it does not explain the experimentally observed difference in intensities between the Stokes and anti-Stokes lines. To overcome these limitations

the quantum mechanical description should be used where the Raman effect is described as an inelastic scattering of a photon from the quantized molecular system via an extremely short-lived virtual state. According to Boltzmann statistics the lowest level of any vibrational mode with $h\nu > k_B T$ are more populated with respect to the excited states. This is why the Stokes lines, for which the initial state is the ground state, are more intense respect to the Anti-Stokes ones [22]. The Rayleigh and Raman processes
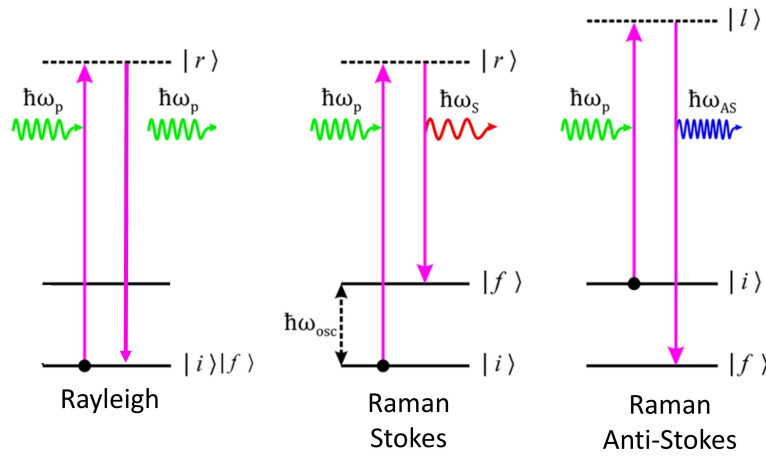
Figure 1.1: Energy transfer process in Rayleigh (left), Spontaneous Stokes (center) and Anti-Stokes (right) Raman Scattering [16].

schematized in the Jablonski diagram of Fig. 1.1 can be described by the transition probabilities between an initial state $|i\rangle$ (with energy $\hbar\omega_P$) and a final state $|f\rangle$ (with energy $\hbar\omega_f$ where $f = P, S, AS$), which are typically derived from the perturbation theory. It is worth noting that we are in semi-classical approach where the molecules are treated quantistically and the electromagnetic field classically. Thus, the polarizability tensor of components $\rho\sigma$ can defined as [21]:

$$(\alpha_{\rho\sigma})_{fi} = \frac{1}{\hbar} \sum_{r \neq i,f} \left\{ \frac{\langle f|\hat{p}_\rho|r\rangle \langle r|\hat{p}_\sigma|i\rangle}{\omega_{ri} - \omega_P - i\Gamma_r} + \frac{\langle f|\hat{p}_\sigma|r\rangle \langle r|\hat{p}_\rho|i\rangle}{\omega_{rf} + \omega_P + i\Gamma_r} \right\} \quad (1.9)$$

where the sum is done over all possible states $|r\rangle$ of the molecule of energy $\hbar\omega_r$ and broading $\sim \hbar\Gamma_r$, $\hat{p}_\rho$ is the electric dipole operator along the

molecular axis $\rho = x, y, z$, $\hbar\omega_P$ is the excitation energy and $\hbar\omega_{ri}$ is the energy of the transition $|i\rangle \to |r\rangle$. The numerator of the Eq. 1.9 is characterized by the transition dipole moment integrals between initial state $|i\rangle$ and the final state $|f\rangle$. In particular, it shows qualitatively that the Raman process occurs as a two-step transition through an intermediate state $|r\rangle$ that does not correspond to an effective electronic state of the system and is said virtual energy state. For this reason the non-resonant Raman scattering is not dependent on the wavelength of excitation source.

1.3 Resonance Raman Scattering

The spontaneous Raman scattering is based on the fact that the energy of the incident photon does not have to match necessarily to that of an electronic transition of the molecule system. However, as the energy of the incident photon approaches that of any electronically excited state, the intensity of resulting Raman scattering can be enhanced by two to six orders of magnitude. This process is called Resonance Raman Scattering (RRS) [23]. The mechanism can be qualitatively explained by looking at the expression for the polarizability seen in Eq. 1.9. In resonance condition, the excitation frequency ω_P approaches the transition frequency ω_{ri} of an electronic absorption band of the molecule: the denominator of the first term becomes small increasing the value of the first term. In such condition, the first term dominates on the second term reducing the expression of the polarizability as:

$$(\alpha_{\rho\sigma})_{fi} = \frac{1}{\hbar} \sum_{r \neq i,f} \left\{ \frac{\langle f|\hat{p}_\rho|r\rangle \langle r|\hat{p}_\sigma|i\rangle}{\omega_{ri} - \omega_P - i\Gamma_r} \right\} \tag{1.10}$$

This increment in the polarizability brings to an enhancement in the intensity of Raman peak. Considering that in semi-classical approximation, the $\left[\frac{\partial\alpha}{\partial Q_k}\right]_0^2$ is replaced by the square modulus of the polarizability tensor $|\alpha|^2$, the expression for the scattered Stokes intensity seen in Eq. 1.8 becomes:

$$I_{Stokes} \propto |\alpha|^2 (\omega_0 - \omega_k)^4 I_0 \tag{1.11}$$

where $\omega_0 = \omega_P$ and $\omega_k = \omega_{osc}$ as shown in Fig.1.1. This explains the Raman signal enhancement up to six orders of magnitude for resonance Raman compared with normal Raman scattering [15].

An important characteristic of this phenomenon is that it selectively enhances Raman signals from the chemical groups of the molecules with a strong absorption band. Such groups are called chromophores and are responsible for the color of the samples. As matter of fact, the Raman signals of the chromophoric component will dominate the spectrum with respect to the remainder. This property renders RRS particularly useful for applications regarding the detection of natural pigments, such as carotenoids, in arts and life science areas [24–26].

In the last years, there have been ongoing efforts to improve the sensitivity and selectivity of this technique. One of the limitations of RRS is that it can not be applied to all molecules and all electronic transitions. The technique requires the use of a laser with a broad tuning range to better match the electronic transition of the molecule under investigation [27, 28]. Another drawback is represented by the fluorescence background. For comparison, the Fig. 1.2 illustrates the Jablonski energy diagram of fluorescence process (right) with resonant Raman scattering (center). Both the processes take place with the absorption of a photon whose energy corresponds to an electronic transition but the main differentiation is related to the lifetime of resonantly excited state $|e\rangle$, as well as, to the nature of the intermediate states [29]. Once the electron is in the excited state, a photon can be emitted through the fluorescence only after the vibrational relaxation of the excited electronic state $|e\rangle_1$ to the ground vibrational state $|e\rangle_0$. This process occurs in a time scale of 10^{-9} s, whereas light scattering is a fast process taking place with no delay in 10^{-13} s [30, 31]. Nevertheless, the fluorescence interference can be overcome by working at longer excitation wavelengths. As seen from the Eq. 1.11, the Stokes intensity scales in general according to the inverse of fourth power of the excitation wavelength. Although the employment of longer excitation wavelength decreases the scattered intensity, the advantage is that few molecules adsorb in the near-IR region compared to the visible region. Thus, this
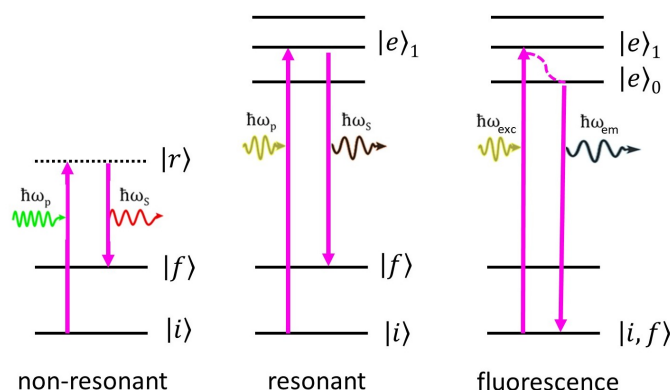
Figure 1.2: Energy transfer process in non-resonant (left) and resonant (center) Raman scattering. In both scattering processes, the lifetime of the excited state is probabilistic and spontaneous. The fluorescence process (left) typically has the lifetime of several *ns* and when the excitation energy overlaps with the first electronic transition, the fluorescence emission from the molecule is likely to interfere with that one of RRS.

solution can be adopted in standard Raman scattering case when the fluorescence is extremely high and the sample damage for the high power is minimal. In the RRS case, instead, the best alternative approach to reduce the fluorescence and increase the scattering efficiency can be found by using the deep UV range from $180 - 260$ *nm*. In addition in this region many molecules have absorption bands, which is a prerogative for the RRS to be effective. The UV-RRS is a useful tool to study the secondary structures of proteins [32, 33] or nucleic acids [34] because the amide vibrations and aromatic amino acids bands are selectivity enhanced in the Raman spectra by using UV excitation wavelength [23].

1.4   Non-linear Raman Processes

The scattering processes considered so far involve two photons overall, one incident and one scattered. However, multiple incident photons can interact simultaneously with the scatter sample under the excitation of high-power lasers (usually pulsed lasers). In this case, the resulting Raman

signal will be enhanced because the signal intensity increases non-linearly with the laser power. The most prominent non-linear optical scattering processes include the Stimulated Raman Scattering (SRS) and Coherent Anti-Stokes Raman Scattering (CARS). The SRS and CARS are coherent four-wave mixing techniques that produce directional beams with small divergences and a well defined phase relationship. The Fig.1.3 shows the two processes schematically. The excitation radiation consists of the over-lap of two monochromatic beams of frequency ω_p (pump) and ω_s (Stokes), where $\omega_p > \omega_s$. The interference between these two beams generates a beating with the frequency $\Omega = \omega_p - \omega_s$ [14]. If the frequency Ω matches
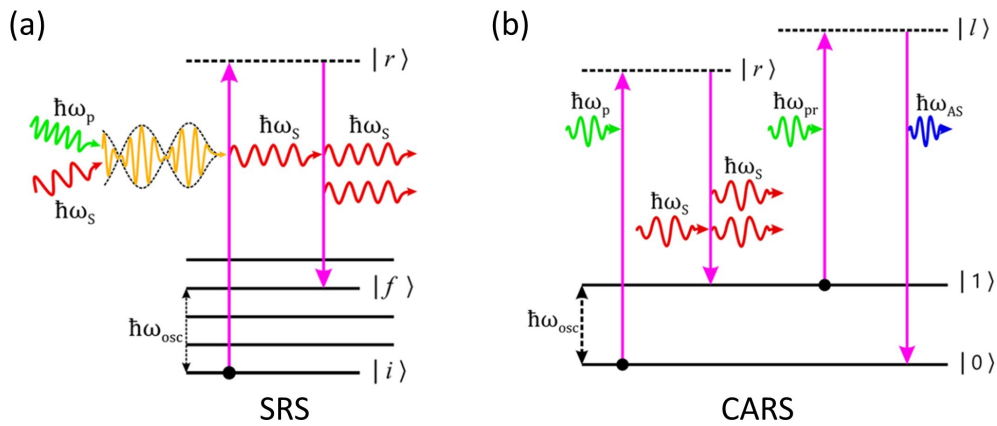
Figure 1.3: (a) Coherent Anti-Stokes Raman Scattering (CARS) and (b) Stimulated Raman Scattering (SRS) processes [16].

the frequency ω_{osc} of a Raman active vibrational mode, the Raman mode enters in resonance with the wave beating and stimulated excitation of the vibrational transition can be produced. The frequency ω_s is, generally, tuned to satisfy this condition.

In the SRS process, the molecule scatters a photon with the same energy and phase of the incident light of frequency ω_s. As result, the outgoing Stokes beam will show a gain in intensity, denoted as Stimulated Raman Gain (SRG), compared to the pump beam that will show a loss, known as Stimulated Raman Loss (SRL) [35]. This intensity difference of the

pump beam is commonly extracted using radio-frequency lock-in amplifier and can give quantitative information of the chemical bonds. In fact, the intensity of the SRS signal scales linearly with the concentration N of the molecules:

$$\Delta I_{SRG} \propto \left(\frac{\partial \alpha}{\partial Q_k}\right)_0^2 NI_pI_s$$
$$\Delta I_{SRL} \propto -\left(\frac{\partial \alpha}{\partial Q_k}\right)_0^2 NI_pI_s$$

(1.12)

where I_p and I_s are the intensities of the pump and Stokes beam, respectively [15]. Since SRS signal is revealed at the same wavelength of excitation Stokes radiation, it is not affected by fluorescence. The ability of SRS to time-resolve the evolution and dephasing of coherent (ro-)vibrational motion is largely used to enhance the weak signals associated with spontaneous Raman imaging of living cells [36].

Unlike the SRS process, CARS requires the interaction of the sample with a third incident beam of frequency ω_{pr} (probe). As described earlier, the process involves the beating between the pump and the Stokes beam of frequency Ω that is resonant with the molecular vibration at frequency ω_{osc}. This molecular vibration is further probed by the probe beam (pulsed laser) to generate radiation at Anti-Stokes frequency $\omega_{AS} = \omega_{pr} + \omega_p - \omega_s$. This second excitation can be also provided by the pump beam giving rise to radiation of frequency $\omega_{AS} = 2\omega_p - \omega_s$ [16, 18]. This expression results from the energy conservation, whereas the direction of the coherent CARS signal is determined by the momentum conservation. Compared to the SRS process where the phase matching is always satisfied, the CARS signal is maximized when the following condition is fulfilled:

$$\Delta k = k_{AS} - (2k_P - k_S) = 0 \qquad (1.13)$$

The phase-matching condition can be achieved experimentally by special laser beam arrangements. In addition, high numerical aperture (NA) lenses or microscope objectives (confocal light) are commonly employed

to satisfy the phase-matching condition without the need for complex mechanical systems. A drawback of CARS is the presence of a non-resonant background signal that can interfere with the resonant CARS signal at low sample concentrations. This signal is usually caused by off-resonant transitions due to the electronic structure of the medium and several methods have been developed to suppress it. Nevertheless, the CARS process can produce resonant signals with an amplification up to 10^6 respect with the spontaneous Raman scattering. This amplification combined to the directed emission with no fluorescence background, makes this approach very attractive in biophotonics as Raman imaging providing chemically-specific contrast [15, 16].

Chapter 2

Plasmon-Enhanced Raman Spectroscopy

The most fascinating example of plasmonic effect in ancient history is probably attributed to the fourth-century Roman chalice, the Lycurgus cup (see Fig. 2.1). At natural light, the cup appears jade green, whereas when it is illuminated from the inside (transmitted light) it turns in a ruby color. Today we know that this intriguing change of color is caused by the presence of gold and silver nanoparticles in the glass matrix, known as dichroic glass [37, 38]. The optical response of the metals is connected

Figure 2.1: The Lycurgus Cup in (a) reflected and (b) transmitted light. Department of Prehistory and Europe, The British Museum, London [39].

to the relative dielectric function $\epsilon(\omega)$ which depends on the frequency

of incident radiation. According to Drude model, in the visible region the noble metals are characterized by small $Im(\epsilon(\omega))$ (i.e. small losses) values and negative $Re(\epsilon(\omega))$ which causes their high reflectivity. These are the conditions that make possible the sustainment of surface and volume charge density oscillations, called plasmon-polaritons (PPs), with specific resonant frequencies.

For a planar metallic interface, the surface PPs (SPPs) propagate as a surface wave along the interface metal/dielectric for distances ranging from tens to hundreds of microns. Such wave decays evanescently in the direction perpendicular to the surface interface within distance of few hundreds of nanometers (Fig. 2.2(a)). Thus, special phase-matching techniques such
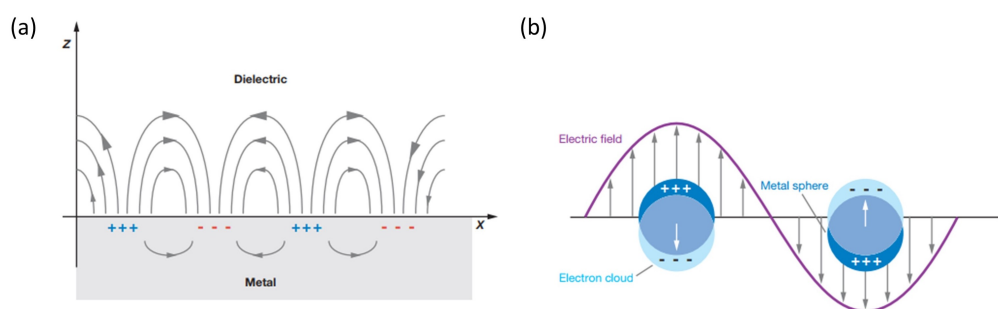
Figure 2.2: Schematic diagrams illustrating (a) a propagating surface plasmon-polariton (SPP) and (b) a localized surface plasmon (LSP) [40].

as grating or prism coupling are required to excite SPPs. The propagation length of SPPs sets the upper size limit for the SPP-based photonic circuitry [41]. In fact, the application of the planar plasmonic structures which confine the SPP along the interface acting as waveguides, has paved the way for the next-generation circuits that use light to overcome the speed limit of electronics [42]. Another characteristic of the SPPs is based on their high sensitivity to any change of the refractive index of the surrounding medium that make them suitable for sensing and detection applications. The change of the local dielectric properties results in a noticeable and detectable shift in SPP resonance (SPR). Thus, for example, the SPR-based techniques can be used for the measurement in real-time of the kinetics of

ligand-receptor interactions or antibody characterization [43].

Another form of the SPP, called localized surface plasmon (LSP), originates when the SPP is confined on small metallic nanoparticles (NPs) which have dimensions smaller than the wavelength of the incident light ($400 - 700$ *nm*). The overall displacement of the electrons with respect to the positively charged lattice leads to a restoring force which in turn gives rise to specific particle plasmon resonances depending on the geometry of the particle (see Fig. 2.2(b)). The resonance response of the LSP (LSPR) can give rise to a strongly enhanced optical near-field localized on the metallic surface. Thus, when a molecule is in the proximity of such nano-structure and is invested from visible radiation, the resulting inelastic scattered light can be amplified thanks to the near-field effect [21, 40]. The Plasmon-Enhanced Raman Spectroscopies (PERS) are based on this mechanism. They include the Surface Enhanced Raman Spectroscopy (SERS) and the Tip Enhanced Raman Spectroscopy (TERS) that will be described in detail in this chapter. Since the dominant mechanism that enables this form of spectroscopies is the LSPR, the first part of the chapter is focused on its description.

2.1 Localized Surface Plasmon Resonance (LSPR)

Let's considering the simpler case of a spherical nanoparticle of radius a and dielectric constant ϵ irradiated by z-polarized light of wavelength λ (with $a < \lambda$) as shown in Fig. 2.3.
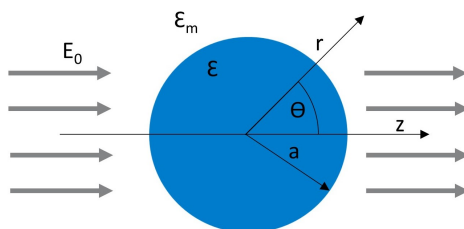

Figure 2.3: Sketch of a spherical nanoparticle placed into the electrostatic field E_0.

The Maxwell's equations can be solved in a quasi-static approximation *i.e.* neglecting retardation and assuming that the electric field $\mathbf{E} = E_0\hat{z}$ is static around the particle. The electromagnetic field surrounding the sphere can be represented by a potential as $\mathbf{E} = -\nabla\Phi$ that satisfy the Laplace's equation $\nabla^2\Phi = 0$. By considering the boundary conditions that both Φ and the normal component of the electric displacement $D = \epsilon_0 E_0$ are continuous, the solution for the potentials Φ_{in} inside and Φ_{out} outside the particle are [44]:

$$
\begin{aligned}
\Phi_{in} &= -\frac{3\epsilon_m}{\epsilon + 2\epsilon_m} E_0 r \cos\theta \\
\Phi_{out} &= -E_0 r \cos\theta + \frac{\epsilon - \epsilon_m}{\epsilon + 2\epsilon_m} E_0 a^3 \frac{\cos\theta}{r^2}
\end{aligned}
\tag{2.1}
$$

The external radiation on the metallic nanoparticle induces the polarization of the surface particle free conduction electrons. In fact Φ_{out} shows the superposition of the applied field and that of the electric dipole located in the center of the sphere. By introducing the dipole moment $\mathbf{p}$ we obtain:

$$
\begin{aligned}
\Phi_{out} &= -E_0 r \cos\theta + \frac{\mathbf{p} \cdot \mathbf{r}}{4\pi\epsilon_0\epsilon_m r^3} \\
\mathbf{p} &= 4\pi\epsilon_0\epsilon_m a^3 \frac{\epsilon - \epsilon_m}{\epsilon + 2\epsilon_m} \mathbf{E}_0
\end{aligned}
\tag{2.2}
$$

We can calculate the expression for the polarizability α of the sphere in the electrostatic approximation considering that $\mathbf{p} = \epsilon_0\epsilon_m\alpha\mathbf{E}_0$:

$$
\alpha = 4\pi a^3 \frac{\epsilon - \epsilon_m}{\epsilon + 2\epsilon_m}
\tag{2.3}
$$

where ϵ is the complex, frequency dependent dielectric function of the metal and ϵ_m the dielectric constant of surrounding medium. It is worth noting that the Eq.2.3 shows the same functional form as the Clausius-Mossotti relation. By solving the equation $\mathbf{E} = -\nabla\Phi$, the electromagnetic

field inside and outside the particle is, thus, given by:

$$\mathbf{E}_{in} = \frac{3\epsilon_m}{\epsilon + 2\epsilon_m}\mathbf{E}_0$$

$$\mathbf{E}_{out} = \mathbf{E}_0 + \frac{3\hat{\mathbf{n}}(\hat{\mathbf{n}} \cdot \mathbf{p}) - \mathbf{p}}{4\pi\epsilon_0\epsilon_m}\frac{1}{r^3} \tag{2.4}$$

As we can see, the solutions for both the fields and the polarizability are characterized by the denominator $\epsilon + 2\epsilon_m$. If the quantity $|\epsilon + 2\epsilon_m|$ is minimized, the fields and the polarizability are enhanced. Thus, this condition can be satisfied at specific frequencies (resonances) when the real part of dielectric function $Re(\epsilon(\omega))$ is close to $-2\epsilon_m$ (Fröhlich condition) and the imaginary part $Im(\epsilon(\omega))$ is very small. This represents the resonance condition for a non-propagating surface plasmon that oscillates locally around the nanoparticle known as localized surface plasmon resonance (LSPR) [44]. The frequency and the shape of LSPRs are strongly dependent on the optical material functions. The noble metals is a class of materials that exhibit strong plasmonic response in the visible region and, for this reason, largely employed in LSPR applications. The behaviour of dielectric function can be predicted by the Drude model that, for an ideal metal with negligible damping ($\gamma_0 \approx 0$), is composed by:

$$Re(\epsilon(\omega)) \cong \epsilon_\infty\left(1 - \frac{\omega_p^2}{\omega^2}\right) \qquad Im(\epsilon(\omega)) \cong \frac{\epsilon_\infty\omega_p^2\gamma_0}{\omega^3} \tag{2.5}$$

where $\omega_p = \sqrt{\dfrac{ne^2}{m\epsilon_0\epsilon_\infty}}$ is the plasma frequency of the metal and ϵ_∞ is the background permittivity i.e. the polarization response from the core electrons. At $\omega < \omega_p$, the real part of dielectric function become negative, whereas the imaginary part smaller. Since the frequency plasma ω_p of most of metals lies in UV region, the metal becomes reflective and shows the plasmonic behaviour at optical frequencies. In fact, the real part of $\epsilon(\omega)$ represents the strength of polarization induced from the external field and determines the resonance condition. The imaginary part of $\epsilon(\omega)$ describes the system losses that occur during the polarization and, so, it limits the

height of the resonance [21]. The Fig. 2.4 shows the imaginary and real part of the dielectric function for some metals.
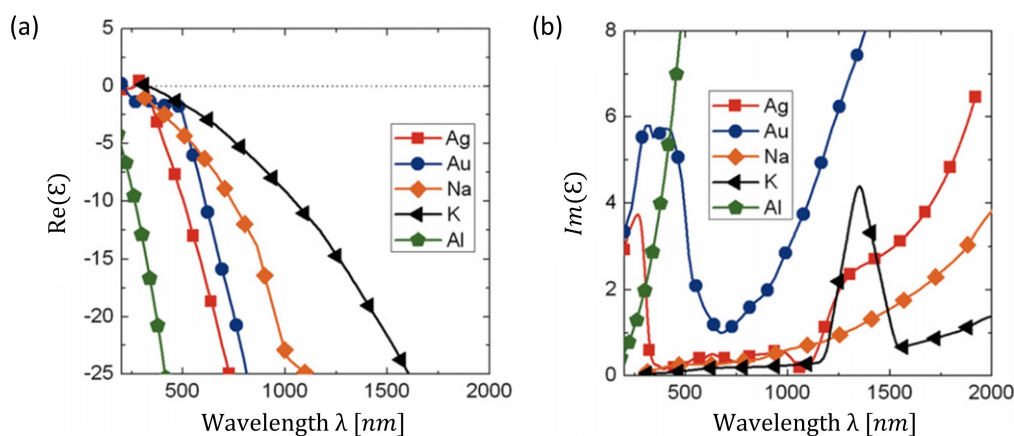

Figure 2.4: The real (left) and imaginary (right) parts of dielectric function $\epsilon(\omega)$ of *Ag*, *Au*, *Na*, *K* and *Al* are plotted against wavelength [45].

In the visible and NIR region the sodium, potassium and silver have the lowest losses. Nevertheless, compared to the silver, the sodium and potassium in elementary form are much more reactive to water and air. Because of their high reactvity, the development of alkali-based devices requires specific treatments to be processed and stored and, thus, it has been limited. Lately, Wang et al. [46] have developed a thermo-assisted spincoating process for fabricating stable performant sodium films operating in NIR that offer opportunities for plasmonic applications. Among all the metals, the silver is known to exhibit broad efficient plasmonic response covering both visible and NIR region and for this property is largely employed [47]. Similarly, the gold is very used, above all, for its low reactivity to external environment even if at frequencies below or about 500 *nm* is affected by high interband losses [48]. Recently, a broad variety of new materials have been explored as alternative to the noble metals. The challenge is finding materials with metal-like optical properties but with much smaller losses. Even if limited at specific wavelength ranges and applications, some solutions for the moment have been found in semiconductors, 2D materials such as graphene, trasparent conductive oxides (TCOs) and

alloyed metals [45].

2.1.1   Enviroment, size and shape effect

An important consequence of the resonance condition is that the LSPRs are very sensitive to the environment surrounding the nanoparticle. According to the Fröhlich condition, the negativity of the dielectric function $\epsilon(\omega)$ grows as the dielectric constant of the medium ϵ_m increases. In other terms as the dielectric constant gets larger, the spectral position of the plasmon resonance is red-shifted (see Fig. 2.4(a)).

Another interesting outcome that can be derived from the quasi-static approximation is related to the far-field optical properties of the nanoparticles. Up till now, we have assumed that the electromagnetic field outside the sphere was produced by the moment of a static dipole. The results previously derived in the limit that $a < \lambda$ can be adapted in the case of an incident time-varying electric field (neglecting spatial retardation effects). This field induces an oscillating dipole, with the same polarizability α of Eq. 2.3, that in turns leads to the scattering of incident radiation from the sphere. The interaction of the light with the nanoparticle can be quantified by the scattering cross-section of the sphere that is related to the polarizability through:

$$\sigma_{scatt} = \frac{k^4}{6\pi}|\alpha(\omega)|^2 = \frac{8\pi k^4 a^6}{3}\left|\frac{\epsilon - \epsilon_m}{\epsilon + 2\epsilon_m}\right|^2 \qquad (2.6)$$

The scattering of the nanoparticle is resonantly enhanced when the Fröhlich condition is satisfied. Similar results are obtained for the absorption (and thus the extinction) of the nanoparticle [44]. We should note that quasi-static approximation is scale-invariant *i.e.* it does not predict any size-related effect. In fact, the resonance condition depends only on the wavelength through the dielectric function and not from size of the object [21]. Moreover, the quasi-static approximation is valid only for particles very small ($\approx 20 - 40nm$). To take into account the size effects, other models have to be considered. This can be done in an analytic (and approximate) way

using the modified long-wavelength approach [49] or by the most accurate Mie theory [50]. The Mie theory provides the full electromagnetic optical solution for a homogeneous sphere of arbitrary size in an homogeneous medium. It fully describes the effects of retardation, including radiative damping and higher-order multipole resonances necessary for the study of the scattering from larger particles. The resonance condition is much more complex showing explicitly a size-dependent quantity. This method predicts a red-shift of the plasmonic resonance as the particle dimension increases. An example of this behaviour is shown in Fig. 2.5(a) where the plot of the optical density of Ag particles at different size are shown.
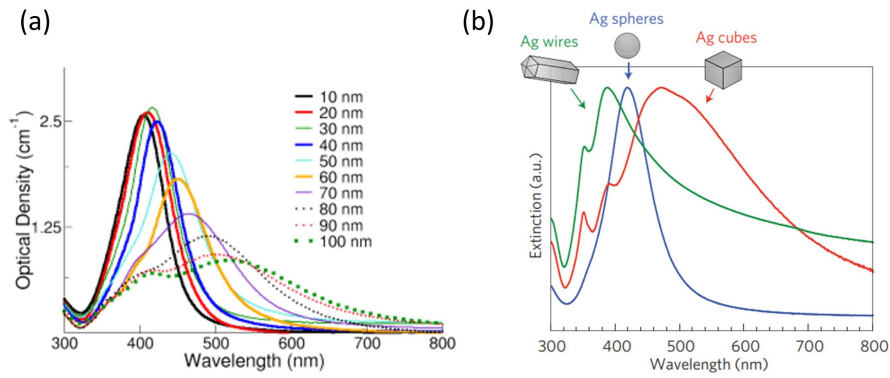
Figure 2.5: (a) Optical Density of silver nanoparticles with different diameter [51]; (b) Normalized extinction spectra for Ag wire ($d = 90 \pm 12nm$), cube ($l = 79 \pm 12nm$) and sphere nanoparticles ($d = 38 \pm 12nm$) [52].

Up to now, we have considered the optical response from a spherical particle. Anyway, when the geometry of a nanoparticle is distorted from that of a sphere, additional resonances appear for each axis of the asymmetric particle. The more general shape that can be described in electrostatic approximation is represented by the ellipsoid. So, let's consider an ellipsoidal metallic particle with semiaxes $a_x \leq a_y \leq a_z$ ($a_i < \lambda$) and dielectric function $\epsilon(\omega)$. The treatment of the scattering problem in ellipsoidal coordinates leads to the following expression for the components of

polarizability tensor α [44]:

$$\alpha_i = v \frac{\epsilon(\omega) - \epsilon_m}{\epsilon_m + L_i(\epsilon(\omega) - \epsilon_m)} \quad i = x, y, z \tag{2.7}$$

where $v = \dfrac{4\pi a_x a_y a_z}{3}$ is the volume of the particle, ϵ_m is dielectric constant of the surrounding medium and L_i is the geometrical factor given by:

$$L_i = \frac{a_x a_y a_z}{2} \int_0^\infty \frac{dq}{(a_i^2 + q)\sqrt{\prod_{i=x,y,z}(q + a_i^2)}} \tag{2.8}$$

that satisfies the sum rule $L_i = \sum_i L_1 = 1$. For the sphere ($a_x = a_y = a_z$) the factor $L_i = 1/3$ in all the directions and the Eq. 2.7 is reduced to the Eq. 2.3. In other cases, the Eq. 2.7 reveals that a spheroidal metal nanoparticle, such as the prolate ($a_y = a_z$) or oblate ($a_x = a_y$) shape, exhibits two spectrally separated plasmon resonances, corresponding to oscillations of its conduction electrons along the major (longitudinal mode) or minor (transverse mode) axis, respectively. The resonance of the longitudinal mode can show a spectral red-shift compared to a sphere of same volume. The analytical treatment of the scattering problem from other geometries is difficult to solve. Consequently, different computational methods such as the discrete dipole approximation or the finite-difference time-domain method (FDTD) are generally used to solve the Maxwell's equations and provide accurate predictions of the optical properties of complicated nanoscale metal systems [45]. The Fig. 2.5(b) illustrates an example of the shape-dependence in the case of three different silver objects. The spectra are characterized by the presence of secondary peaks and shoulders corresponding to the multipolar excitations [53, 54].

2.1.2 Coupling effect

In addition to the previous effects, the LSPR is also sensitive to the presence of other nearby metal nanoparticles. In fact, as discrete nanoparticles aggregate, the plasmonic resonance is greatly modified. The assembling

generates effects of higher multipoles resulting from the irregular particles shape and the dipole-dipole interactions. In general, a red-shift of LSPR of the nanoparticles system is observed due to the inhomogenous polarization of the nanoparticles [55]. In addition, the plasmon coupling generates a strongly confined and enhanced electric field, noted as hotspot, within the gap between coupled particles. These properties, in particular the presence of the hotspots, enable applications such as the single molecule detection using SERS (as will be described in next section) and the synthesis of composite materials exhibiting an enhanced nonlinear optical response [56]. For a comprehensive understanding of the coupling mechanism, let us consider the simplest case of two nanoparticles placed at distance d. Depending on the interparticle spacing d, we can identify four regimes of plamonic coupling [45]:

1. **Far-field coupling**: when the nanoparticles are enough distant from one to another, the coupling takes place by the interaction of the two light scattered fields in far-field;

2. **Near-field coupling**: when the nanoparticles are in close proximity, the coupling can be described in terms of the hybridization of plasmon modes. In this model the dimer plasmons can be viewed as bonding (bright modes) and antibonding (dark modes) combinations, i.e., hybridization of the individual nanoparticle plasmons. The Fig. 2.6(b) shows the distance dependence of the near-field interaction between two nanoparticles. At intermediate distances (5 $nm < d < 10$ nm), the plasmon coupling follows the bonding interaction of two classical dipoles ($1/d^3$) and a single peak is shown in the scattering spectra. As the distance decreases, the coupling become more intense because of the interaction and mixing of surface plasmons with higher multipole oscillations. Such near-field interaction introduces minor scattering peak at shorter wavelength and red-shifts the main peak as the distance becomes smaller. The stronger localization of the near-field gives rise to the hotspots in the interparticle gap. This is, therefore, the regime of particular interest

for the SERS applications [57];

3. **Quantum tunneling**: when the gap distance becomes very small ($d < 0.3\ nm$), the plasmon response is affected by quantum mechanical effects and the quantum tunnelling becomes possible. A classical approach is not more valid and quantum mechanical considerations are necessary [58]. Unlike the near-field regime, a blue-shift is observed in the plasmon resonance as the interparticle distance decreases;

4. **Conductive contact**: when the the nanoparticles are in contact, the coupling is conductive and the excitation of the plasmon resonances induces a net charge on each particle.
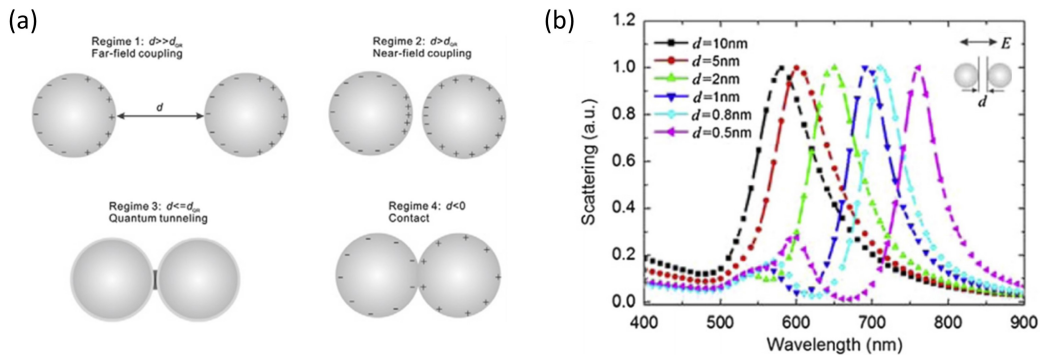
Figure 2.6: (a) Evolution of the plasmonic interaction as a function of spacing d. The value d_{QR} indicates the distance at which the plasmon interactions enter the quantum regime; (2) Scattering spectra of coupled nanosphere dimers for different spacings in regime of near-field coupling. The diameter of each particle is 64 nm. The incident light is polarized along the major axis of the dimer [45].

Polarization dependence

It is worth noticing that for the most of plasmonic structures (dimers or more complex systems), the resonances depend from the polarization of the incident radiation. In the case of a dimer, if the incident radiation is polarized in direction parallel to the major axis, the scattering spectra of the

plasmon resonance exhibit a strong intensity accompanied by a red-shift of the peak and a hotspot concentrated at the gap of the nanosphere dimer. In contrast, the intensity of scattering peak is lower when the polarization is directed perpendicularly to the major axis of the dimer (Fig. 2.7(a)). Anyway, it was observed that assembled structures with high simmetry exhibit spectra with polarization-indipendent characteristics. An example is given in Fig. 2.7(b) where the scattering spectra in function of polarization angle of a 3D hexamer are shown. All the scattering spectra overlap (black line) by changing the polarization direction, highlighting the optical stability of the structure. In addition, also the extinction spectra are in-plane polarization-independent, so only the extinction curve with polarization angle 0° (purple line) has been plotted. Nevertheless, a small difference in the interparticle separation can lead to a symmetry breaking and, thus, large changes in the scattering spectra [45].
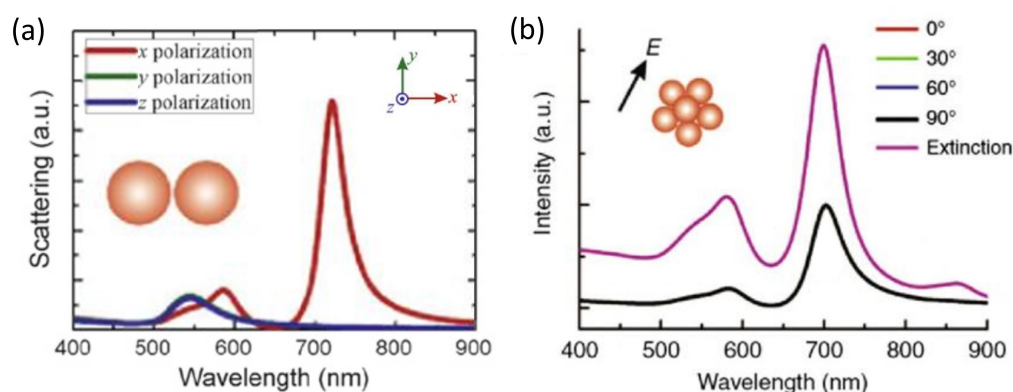
Figure 2.7: (a) Calculated scattering spectra of the 2D dimer for three typical polarization cases (x, y, and z polarizations); (b) Calculated scattering spectra of a 3D hexamer under s-polarized light. Arrow direction indicates polarization direction for 0° [45].

2.2 Surface-Enhanced Raman Spectroscopy

The LSPRs play a central role in the field of ultrahigh-sensitive spectroscopic techniques. Among them, the Surface Enhanced Raman Spec-

troscopy (SERS) is certainly the most important in terms of the number of applications in many fields of science (physics, chemistry, and biomedicine). The first experimental observation of SERS effect is attributed to Fleischmann *et al.* in 1974, who observed an unexpected strong Raman signals coming from pyridine molecules adsorbed on a rough silver electrode [1]. This discovery promoted numerous experimental and theoretical approaches to explain the physical nature of the phenomenon expanding the area of the research from roughened electrode surfaces to more complex plasmonic nanostructures. Nowdays, it is well known that SERS permits to amplify the weak Raman signals of molecules that are very close or attached to specific SERS-active nanostructures [59]. The high sensitivity and molecular specificity of SERS has attracted interest in many research fields such as the chemical and biological sensing applications, the study of the electron transfer reactions, the detection of explosives/chemical weapons or aerosol pollutants [16].

2.2.1 SERS enhancement Mechanism

It is widely accepted that the SERS effect can be attributed to two enhancement mechanisms: electromagnetic (EM) and chemical (CE). Both the mechanisms contributes to the SERS enhancement but the EM mechanism plays a predominant role. The EM mechanism can increase the Raman signal by a factor up to 10^8 to 10^{11}, whereas the CE enhancement contributes with a factor of the order of 10^2-10^3 [16]. Formally, the Raman and SERS signals are related by the following relation [60]:

$$P_{SERS} = M_{SERS}P_{Raman} = M_{EM}M_{CE}P_{Raman} \tag{2.9}$$

where M_{SERS} represents the SERS enhancement factor comprising the two multiplicative contributions coming from the EM enhancement M_{EM} and CE enhancement M_{CE}. The origin of these two contributions is described below.

Chemical Enhancement

The CE enhancement is a short-range effect that arises from the modification of the polarizability when the molecule interacts with the metallic surface. The physical-chemical adsorption alters the electronic and geometrical structure of the molecule. In particular, the Raman cross-section of the k-th vibrational mode is modified respect to that of the free molecules. This changing defines the CE enhancement as [60]:

$$M_{CE} = \frac{\sigma_k^{ads}}{\sigma_k^{free}} \tag{2.10}$$

Although the exact mechanism of CE enhancement is still controversial, some hypothesis have been proposed. In particular, Jensen *et al.* [61] have identified three distinct contributions to the chemical mechanism, that may happen separately:

- An enhancement due to the ground state chemical interaction molecule-metal: it's not associated to any excitation of adsorbate-surface system. The presence of the metallic surface causes only a redistribution of electron cloud of the molecule. The polarizability is, thus, modified leading to a variation of both the Raman shift and intensity of the vibrational modes (Fig. 2.8(a)) [17, 60];

- An enhancement due to the interaction metal-molecule that forms an adsorbate-metal nanostructure complex which may lead to a change in the Raman polarizability, spatial orientation and symmetry of the adsorbate molecule. If the new created transition state of this complex is in resonance with the laser, a resonant Raman enhancement can occur (Fig. 2.8(b)) [17, 62];

- Another contribution comes from a resonance Raman-like process in which charge transfer (CT) between metal and adsorbate is the intermediate stage of the resonance Raman scattering. A charge transfer can occur as an exchange of electrons between the Fermi level

of the metal and the lowest unoccupied molecular orbital (LUMO) or the highest occupied molecular orbital (HOMO) of the molecule (Fig. 2.8(c)) [62].
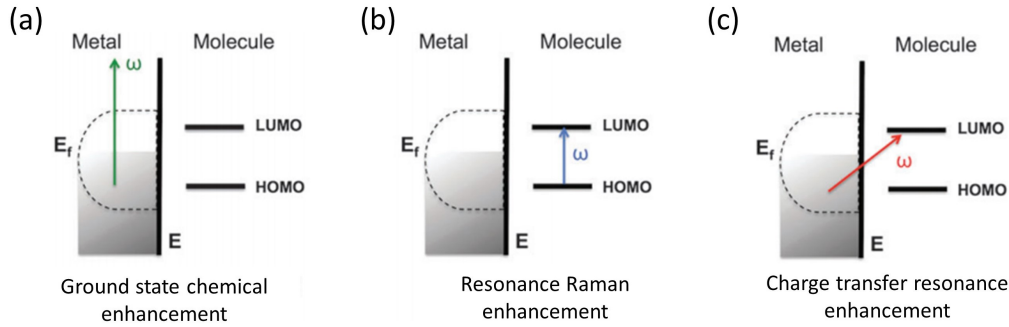

Figure 2.8: Illustration of the three chemical enhancement mechanisms in SERS [63].

It should be noted that the chemical mechanism may result in either a quenching or an enhancement of the scattering process [62]. Although the chemical mechanism contributes a far smaller to the SERS enhancement with respect to the EM one, it can change the spectral pattern considerably, including peak positions and their relative intensities [17].

Electromagnetic Enhancement

The EM enhancement mechanism can be explained by considering the case of a molecule placed in vicinity of a metallic nanoparticle surface. As described in Sec. 2.1, when the LSPRs are excited by an incident radiation of frequency ω_0, free electrons accumulate on the metallic surface increasing the density of surface charges. This leads to the strong confined and enhanced electric field $\mathbf{E}_{out}(\omega_0)$ outside the particle which is stronger of the incident field $\mathbf{E}_0(\omega_0)$. The local field intensity enhancement experienced by the molecule near to the surface can be, thus, defined as:

$$M_{loc}(\omega_0) = \frac{|\mathbf{E}_{out}(\omega_0)|^2}{|\mathbf{E}_0(\omega_0)|^2} \tag{2.11}$$

In addition, the same field associated to the inelastic Raman scattering undergoes a second process, called re-radiation enhancement. The Raman scattering is, thus, amplified of a factor:

$$M_{sc}(\omega_{sc}) = \frac{|\mathbf{E}_{out}(\omega_{sc})|^2}{|\mathbf{E}_0(\omega_{sc})|^2} \tag{2.12}$$

The re-radiation enhancement can be seen as a local field enhancement problem with an exciting laser at frequency ω_{sc} rather than ω_0. Finally, the total EM enhancement, due to both excitation and re-emitted radiation enhancement, can be expressed as [17]:

$$M_{EM} = M_{ex} \times M_{sc} \tag{2.13}$$

For small Raman shifts ($\omega_0 \cong \omega_{sc}$), we can suppose that $M_{sc} \approx M_{ex}$ and, thus, $M_{EM} \approx M_{ex}^2 \approx |\mathbf{E}_{out}(\omega_{sc})|^4/|\mathbf{E}_0(\omega_{sc})|^4$. It explains why it is commonly admitted that the SERS enhancement scales as fourth power of the ratio between the field near the nanoparticle and the incident one [64]. Although this approximation, noted as $|E|^4$ approximation, is widely used in SERS, it has not a general validity in specific situations and a more rigorous approach is required. One example of this situation is the study of polarization effects or surface selection rules in SERS [21, 60].

In practical situations, the EF is experimentally calculated taking into account the number of molecules that contribute to the SERS signal. The EF is calculated as:

$$EF = \frac{I_{SERS}/N_{SERS}}{I_{RAMAN}/N_{RAMAN}} \tag{2.14}$$

where I_{SERS} and I_{RAMAN} represent the intensity of a given Raman band of the SERS and spontaneous Raman spectra, respectively, whereas N_{SERS} is the number of molecules in the scattering area denoted by the laser spot and N_{RAMAN} are the molecules in the scattering volume [65]. Actually, as we will see in the expermental part of this work thesis, the EF depends also on other factors wich are the power laser and the time integration of the acquired spectra.

2.2.2 Distance Dependence

As discussed above, the total SERS signal is dominated by the electromagnetic enhancement, which strongly depends on the local geometry of the metal nanostructures and the properties of the interparticle gap. The previous theoretical treatment predicts that the SERS enhancement depends on the distance of the molecule from the metal surface. Indeed, according to the Eq. 2.4, the local field around a nanoparticle decays as with r^{-3}. Following the $|E^4|$ approximation, the overall distance dependence should scale with r^{-12}. Actually, the theoretical distance-dependent Raman intensity I_{SERS} can be obtained taking into account the scaling factor r^2 of the shell of molecules at an increased distance from the nanoparticle [65]:

$$I_{SERS} \propto \left(1 + \frac{r}{a}\right)^{-10} \tag{2.15}$$

Experimentally, this type of dependence has been obtained by measuring the SERS signal of different spacer layers, such as Langmuir-Blodget (LB) films [66] or self-assembled monolayer (SAM) [67], deposited on the plasmonic nanostructure. Recently, Masango *et al.* [68] have used the atomic layer deposition (ALD) to deposit ultra-thin metal oxide films on a plasmonic substrate (a silver film over nanosphere (AgFON)). This deposition method enables to produce a highly uniform films whose thickness can be controlled with Å-level precision and to obtain, thus, a distance dependence function with higher resolution. Their experimental results suggested that SERS distance dependence should take in account the short- and long-range SERS effects, by using a two-term phenomenological expression:

$$I_{SERS} = C_1\left(1 + \frac{r}{a_1}\right)^{-10} + C_2\left(1 + \frac{r}{a_2}\right)^{-10} \tag{2.16}$$

where a_1, a_2 are the short-range and long-range radii of curvature of AgFON features, respectively, and C_1, C_2 are constants that account for the relative contributions of the two terms. The experimental and theoretical SERS distance dependence are reported in Fig. 2.9(a).
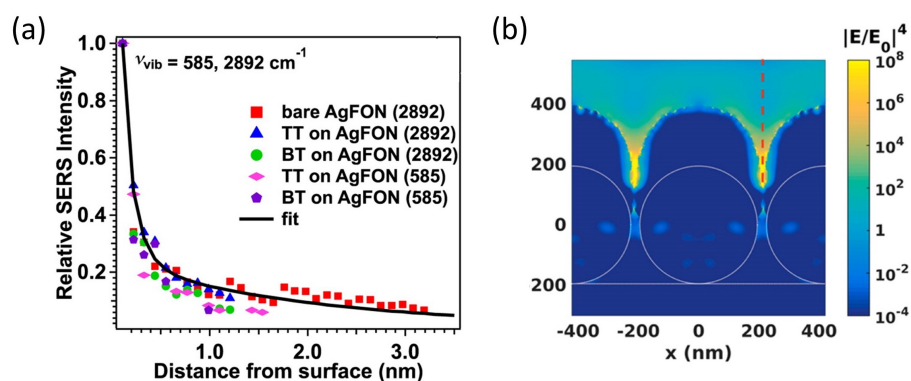
Figure 2.9: (a) Normalized SERS intensity decay of two Raman bands ($2892\ cm^{-1}$ and $585\ cm^{-1}$) as function of the distance from a bare AgFON and AgFONs functionalized with thiol SAMs. The black solid line is the fit to the data using Eq. 2.16; (b) Spatial distribution of local electric field enhancement from FDTD calculations of simulated AgFON surface [68].

2.2.3 The role of hotspots

The case of a single metallic nanoparticle produces an EM enhancement too low to have practical application. A stronger EM amplification is achieved when more nanoparticles aggregate. As described in the paragraph 2.1.2, the plasmon coupling occurring in near-field regime generates an intense electromagnetic field (hotspot) confined in the interparticle gap that can even support the detection of a single-molecule [69]. The hotspots, in particular, can be classified depending on the type of nanostructure.

A first generation is identified in the hotspots produced on single nanostructures (nanosphere, nanocubes or nanorods). This group of hotspots exhibits a moderate SERS-activity. Anyway, the design of single nanostructure with a more intriguing shapes, such as nanostars, can produce a stronger SERS-activity near the sharp corners. The second generation of SERS hotspots arises on coupled nanostructures with controllable interparticle nanogaps (dimers, arrays, oligomers). This type of nanostructures are widely employed because they can assure higher SERS amplification. For example, they are used for the trace-molecule detection and biomolecule analysis. In general, these two generations of hotspots are

well suited for the study of probe molecules that can be "trapped" in the nanogaps but not for the surface analysis of many materials. So, a third generation of hotspots have been designed in last years. They are generated by hybrid structures consisting of plasmonic nanostructures and the probe materials [69]. An example for each generation of hotspots is shown in Fig. 2.10.
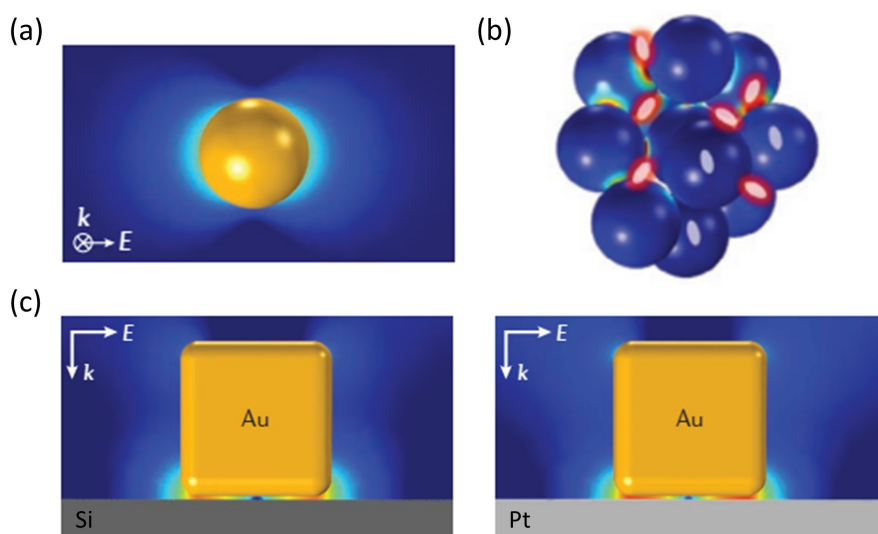
Figure 2.10: Finite-element simulations of surface-enhanced Raman spectroscopy (SERS)-enhancement distribution for: (a) an *Au* nanosphere; (b) an *Au* nanoparticles aggregate; (c) an hybride structure formed by an *Au* nanocube coupled to a semiconductor (left) and metal (right) substrate [69].

2.3 Tip-Enhanced Raman Spectroscopy

In addition to various metal nanostructures with SERS hotspots, metal or metallized tips on Scanning Probe Microscopes (SPM) are also used to enhance the Raman scattering, giving rise to a new technique called Tip Enhanced Raman Spectroscopy (TERS). A highly localized surface charge density can be induced in proximity of the tip when a laser beam is

properly focused on the apex of the sharp tip having radius of curvature of $10 - 50$ *nm*. So, the tip becomes a source of the localized electric field enhancement that can amplify the Raman signal of a molecule placed underneath the tip. If the molecule is localized on a metallic surface (gap-mode configuration), the coupling tip-surface can produce a strong confined electric field (hotspot). The distance tip-surface is controlled to (sub-) nanometers by the feedback system of the SPM microscope used. The small size of the tip enables to achieve higher spatial resolution (few nanometers) with respect to the diffracted-limited SERS spectroscopy. The maximum spatial resolution of conventional optical microscopy is limited to approximately 200 nm according to the Abbe formula:

$$\Delta x = 0.61\lambda/NA \qquad (2.17)$$

where λ is the wavelength of the incident light and NA is the numerical aperture of the objective. It is worth noting that although a larger area is illuminated, only the area around the gap is enhanced. Thus, the TERS technique offers spatial resolution of $1 - 10$ *nm*. The idea to combine SPM technologies with the Raman spectroscopy came up in 1985 by Wessel [70]. Later, other four groups [71–74] performed TERS experiments in 2000, demonstrating the usefulness of this technique. Since then, TERS has been growing a great interest in different research areas thanks to the high spatial resolution and high sensitivity and the possibility to acquire simultaneously both the topography and the corresponding spectral information of the analyte [75].

2.3.1 TERS enhancement mechanism

Similarly to the SERS, the enhancement mechanism of TERS involves both the EM and CE enhancement. Nevertheless, the main contribution is due to the EM enhancement that includes different effects. One of these is the lightning rod effect (LRE) that is based on the generation of a highly confined electric field at the apex of an illuminated sharp metallic tip. It is
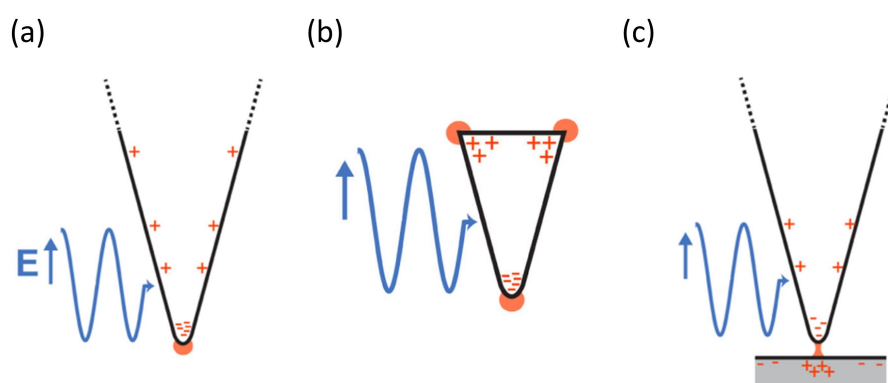
Figure 2.11: Sketch of the different types of mechanisms for EM enhancement at the apex of a metallic tip: (a) Lightning-rod effect (LRE); (b) Localized surface plasmon resonance (LSPR); (c) Gap plasmon effect [76].

due to the shape of the tip that leads to an higher concentration of charge surface density at the apex of the tip. Therefore, it is a non-resonant process depending only on the geometry and the conductivity of the tip material at the frequency of light that drives the surface charge density (Fig. 2.11(a)). It is a resonant mechanism, instead, the excitation of the LSPR on the metallic tip that creates a hotspot at the apex of the tip (Fig. 2.11(b)). Indeed, the nano-antenna can resonate, if the length of the tip is a multiple of one-half of incident wavelength [77]. It should be noted that at optical frequencies the antenna resonances are excited by a shorter effective wavelength λ_{eff} which depends on the material properties [78]. Another type of resonant mechanism in the EM enhancement can be obtained in the gap-mode configuration, *i.e.* when the analyte is placed between the metallic tip and a metallic substrate (Fig. 2.11(c)).

Gap-mode configuration As seen before, the lightning rod effect induces a surface charge density at the apex of the tip that can be seen as a point dipole. As a result, mirror charges accumulate on the substrate that can be described as an image dipole. By the combination of the tip-apex mode and the surface plasmon modes, a new hybrid mode is formed which is called gap-plasmon mode [77]. The enhancement factor in a

gap-mode configuration can reach up to $10^6 - 10^8$ and can be three orders of magnitude higher than that of non-gap-mode TERS. The width of the confined field in the gap-mode TERS configuration is strongly related with the tip radius R and the tip-sample gap d. This dependence can be easily obtained considering the tip-substrate configuration as a system of two spheres separated of a distance d (see inset in the Fig. 2.12). By assuming
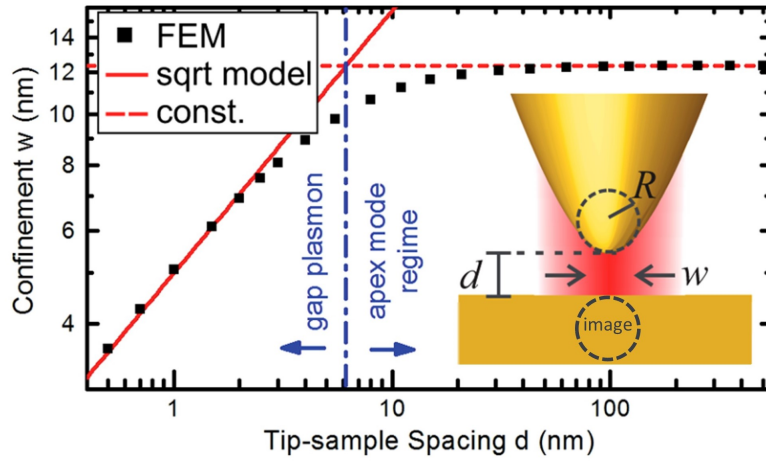
Figure 2.12: Lateral confinement w of the local filed intensity $|E_{loc}|^2$ obtained as FWHM from cross-sections through finite element method (FEM) simulations. The inset shows the system tip-substrate as a system with two spheres at distance d [77].

that the two spheres (original and images dipoles) are equipotential, the local field can be related to the incident field by $\Delta V = |E_{loc}|d = |E_{inc}|(2R + d)$. Thus, the lateral offset of the electric field from the center can be written as:

$$|E_{loc}(x)| = \frac{\Delta V}{2R + d - 2\sqrt{R^2 - x^2}} \tag{2.18}$$

The FWHM of the local field is, thus, given by $w = 2\sqrt{Rd}$. This result is similar to that obtained in more accurate calculations that lead to a local field confined in a region $w \propto \sqrt{Rd}$ [79]. For a qualitative discussion, in the Fig. 2.12 is shown the simulation of the lateral FWHM in function of the distance tip-substrate estimated for tunnel junction between taper probes

and flat surfaces [80]. Fixed $R = 10$ *nm*, at distances of less than 10 *nm*, the gap-mode plasmon is formed and the lateral confinement w rapidly decreases as the distance d. The maximum lateral optical resolution w achievable is ≈ 2.5 *nm* that corresponds to the lower reasonable value of $d = 0.5$ *nm*. At lower distance we enter in the quantum tunnelling regime that can significantly modify the plasmonic response of the system (see Sec. 2.1.2). For distances d larger than 10 *nm*, the confinement w becomes constant. The local electric field is not influenced by the gap and only determined by the tip radius. Therefore, by decreasing the gap distance is possible to improve both the local field enhancement and the lateral confined region, apart from the tip radius [81].

Contrast and enhancement factor

Considering that the main contribution to the TERS enhancement is electromagnetic, the electric field enhancement can be written as:

$$g = E_{tip}/E_0 \tag{2.19}$$

where E_{tip} and E_0 are the enhanced electric field underneath the tip and the incident electric field without the tip in contact, respectively. The light intensity is proportional to the square of the EM and the enhancement is dependent on both the wavelength of the incident radiation and the Raman scattered one. Thus, the enhancement factor (EF) can be defined as:

$$EF = g_{\lambda_L}^2 \times g_{\lambda_R}^2 \approx g^4 \tag{2.20}$$

where $g_{\lambda_L}^2$ can be approximated to $g_{\lambda_R}^2$ if the Raman shift is small. The EF is dependent on the excitation wavelength and on the material, the size and shape of the tip [75]. From an experimental point of the view, the enhancement factor depends on two factors: the contrast and geometry factor. The contrast is defined as the ratio of near-field Raman intensity to

the far-field Raman signal intensity, and is given by:

$$C = \frac{I_{NF}}{I_{FF}} = \frac{I_{tip} - I_0}{I_0} = \frac{I_{tip}}{I_0} - 1 \tag{2.21}$$

where I_{NF} indicates the intensity of the near-field Raman signal from the region just below the tip and I_{FF} is the far-field Raman signal intensity when the tip is not in contact. A high contrast value implies a strong plasmonic TERS enhancement at the apex of the tip. The intensity I_{tip} is the TERS experimentally detected Raman intensity which is superimposed on a relatively large non-enhanced background I_0. In TERS spectrum, the Raman bands become visible thanks to the strong localized electric field near the tip that enhances the Raman signal even coming from a small number of the target molecules. In this case, I_0 cannot be detected and is calculated based on the noise level in the far-field spectrum. So, the total TERS EF is determined taking into account the contrast and the difference in source volume (or area) of the near- and far-field signal and is expressed as:

$$EF_{ters} = C \frac{V_{FF}}{V_{NF}} \approx C \frac{A_{FF}}{A_{NF}} \tag{2.22}$$

where V_{FF} and V_{NF} are the volumes containing the molecules that contribute to the far- and near-field signal, respectively. In the case of bulky samples with a considerable optical penetration depth, the source of far- and near-field is represented by the volumes expressed as $V = hA$, where the height h is given by the focus or the optical penetration depth. In the case of thin film or opaque samples, V can be approximated with the source areas A. The far-field area depends on the whole laser focus and can be calculated as $A_{FF} = r_{laser}^2 \pi$, where r_{laser} is the radius of the excitation laser focus spot. The near-field area, instead, is often approximated to $A_{NN} = r_{tip}^2 \pi$ where r_{tip} is the tip radius. However, it is demonstrated experimentally that the enhancing region is, at least in some cases, smaller than the tip apex. A more precise way for the determination of the radius of both areas would be to determine the lateral resolution of both, confocal Raman and TERS images [82–84].

2.3.2 TERS setup

The efficient excitation of electromagnetic-field in TERS experiments requires a complex and challenging setup capable to combine SPM technology with Raman microscopy. Different configurations have already been proposed in the literature. These configurations can be distinguished mostly by the type of microscopy/tip and the illumination geometry. Among the various SPM technologies, the Scanning Tunneling Microscopy (STM) and Atomic Force Microscopy (AFM) are the most used. One of the first configuration for TERS experiments was based on the AFM [73, 74]. The AFM employs a sharp tip placed at the end of a cantilever to scan the sample surface and obtain topographical information. The distance tip-substrate is force-controlled using a feedback-loop mechanism. The feedback signal can be detected by the deflection of the cantilever that provides the morphology information of the sample surface. This setup can be used on any surface and it does not require a conductive surface as in STM. In AFM-TERS experiments the tips are, generally, covered with either a continuous metal film (*Au* or *Ag*) or metal nanoparticles [75]. In this context, the Chap. 4.1 will provide a in-depth discussion on the tip manufacturing. In TERS configuration the AFM is, mostly, used in contact mode. The constant distance from the surface can provide a constant near-field enhancement [85]. Nevertheless this mode is not suitable for analysing sensitive biomaterials. Thus in other cases the tapping mode (or AC mode) where the tip oscillates close to its resonance frequency is preferred. This modality is considered to be more "gentle" on the sample surface. Moreover, it is interesting to note that it can be also used for estimating the tip-sample distance dependence of the TERS signals. As mentioned before, another distance control method in TERS is the STM. The STM is a microscopy for imaging surface at an atomic resolution (0.1 *nm*). At the contrary of the AFM, the distance tip-substrate is controlled by keeping constant the electron tunneling current between a metallic tip and a conductive substrate. Thus to maintain the electron flow, only very thin non-conductive samples (few nanometers) can be investigated limiting the technique to

the study of only ultrathin or conductive samples. Moreover, the STM tips are obviously made of metal in order to sustain the tunneling current. Anyway, STM-TERS set-ups can provide better vibration information and spectroscopic resolution, up to the mapping of a single molecule. Another important characteristic is that the employment of golden or silver films enables the gap-mode effect which further enhances the Raman signal as discussed beforehand [86].

Illumination geometry

Depending on the configuration of the SPM system and the sample properties, it is important using the appropriate optical geometry. Moreover, the choice of the geometry design determines the properties of the objective lens that can be used. The most used types are essentially the bottom-, side- and top-illumination [75, 85, 86]:

1. **Bottom-illumination**: the incident laser is tightly focused with an high numerical aperture (NA) objective from below through a transparent support onto the tip and the sample (Fig. 2.13(a)). The backscattered light is usually collected by the same objective even if different collection direction would in theory also be possible. Using high NA (oil immersion) objectives ($NA = 1.4 - 1.6$) allows a tighter focusing and, thus, a more confined laser energy where the far-field background contribution from the confocal volume is minimized. Moreover, such objective in bottom configuration provides a higher collection efficiency compared to the other optical geometries. The signal can be further amplified using the proper polarized laser light. The enhancement can be improved when the electric field component is parallel to the tip axis (p-polarization). It has been demonstrated that a radial polarized beam laser can produce a stronger p-polarization component. Thus, in this configuration is preferable the employment of this polarization to generate larger field enhancement and improve the TERS contrast. The back-reflection geometry can be used only for transparent samples and is ideally suited to
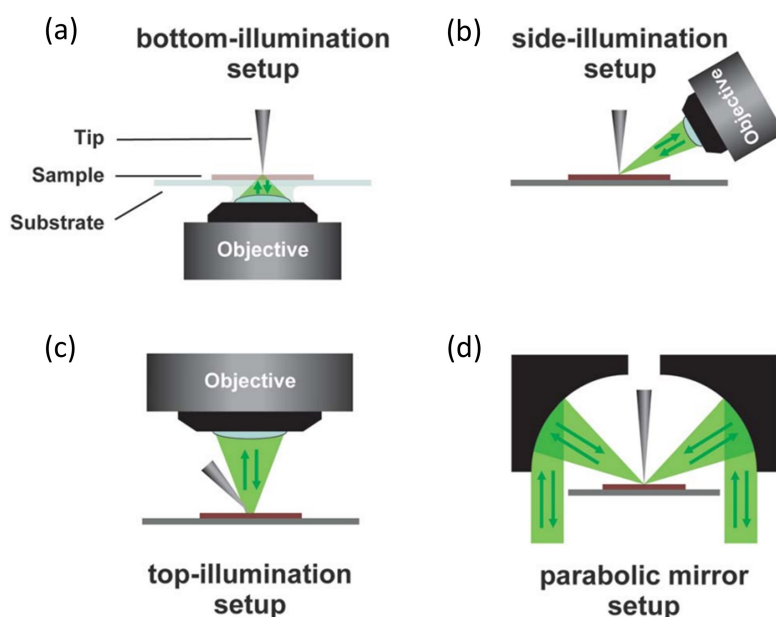
Figure 2.13: Illustration of the different illumination and detection geometries for TERS experiments [85].

investigate biological samples. This optical geometry is used mostly in AFM configuration even if conducting substrates like indium tin oxide (ITO) or thin gold films have extend it also to STM feedback;

2. **Side-illumination**: the sample is illuminated at an angle ($45° - 80°$) from above the sample (Fig. 2.13(b)). In this case, objectives with considerable working distance have to be used to reach the tip and the sample ($NA = 0.28 - 0.55$). Due to the angle between the excitation beam and the sample surface, the focused beam results elliptical and enlarged of $\approx 2 - 3\ mm$. Thus, it requires the use of higher power laser that if on one hand it compensates the decreased efficiency, on the other hand it leads to heating effects and possible damage of the samples. Anyway, the advantage is the possibility to investigate opaque samples. The small values of NAs can be compensated by working in gap-mode configuration. Moreover, the linearly polarized light can excite stronger p-polarization component with respect

to the bottom illumination. The side-illuminated is generally used in STM and SFM systems;

3. **Top-illumination**: the sample is illuminated from the top along the direction of the tip. It combines the advantages of the two previous geometries by using NAs ranging from 0.3 to 0.7 and allowing the investigation of both transparent and opaque samples. High NA can be employed to tightly focus the light on the tip and excite the local field enhancement with a longitudinal wave. Anyway, one the main drawback is the shadowing effect produced by the location of the tip between the objective and the sample. To overcome this limitation, higher order laser modes such as the so-called doughnut modes have been used. Moreover, a parabolic mirror ($NA \approx 1$) as shown in Fig. 2.13(d) can be employed to increase the excitation and collection efficiency. The top-illumination geometry is used in both AFM and STM configuration.

Chapter 3

Experimental Methods and Equipments

This Chapter is dedicated to the methods and the experimental set-ups used for the fabrication of the plasmonic devices with the approach described in the Sec. 4.2. In particular, the deposition process (Magnetron Sputtering) and the plasma treatment system used to induce the formation of *coral-like* structures are first discussed. Finally, the apparatus including the micro-Raman and Atomic Force Microscope which represents the heart of SERS and TERS investigations will be discussed.

3.1 Magnetron Sputtering

The magnetron sputtering is a thin-film deposition method belonging to the class of the physical vapour deposition (PVD) processes. Compared to chemical-vapor depositions (CVD), PVD approaches are preferred because they do not require high deposition temperatures and the use of specialized precursor materials. Some of these materials are corrosive, flammable or even toxic [87]. Actually, the most two common PVD processes are based on the evaporation and sputtering phenomena. Atoms can be evaporated or ejected from a solid source (target) and, subsequently, deposited on substrates placed at a proper distance. In particular, the evaporation

methods (resistive, e-beam, etc.) are usually employed for the preparation of thicker layers and coatings with lower surface morphological requirements. In fact, during the deposition, the melting material can release larger grains and some contaminant particles which can affect the uniformity and the purity of the films, respectively. On the other hand, the sputtering methods (magnetron, ion beam, etc.) are suited for thinner coatings requiring higher purity and uniformity. In particular, the magnetron sputtering offers a higher deposition rate and a better control on the uniformity of substrates [88].
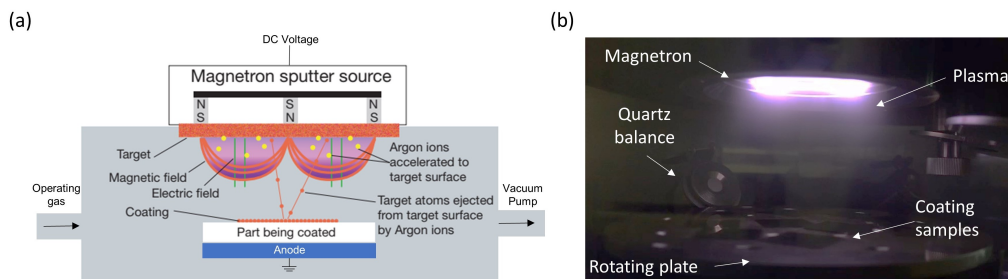

Figure 3.1: (a) Scheme of the operating process of the magnetron sputtering [89]; (b) Photograph of the Q300T D circular magnetron during operation in Argon gas discharge. The formation of the dense plasma is well visible.

The operation principle of the magnetron sputtering is shown schematically in Fig. 3.1(a). To avoid any film contamination, the deposition process occurs in an evacuated chamber (at vacuum level of the order of 10^{-3} *mBar*) which is then filled with a low-pressure inert gas (feeding gas). The best choice as operating gas is represented by the Argon because is particularly efficient for sputtering metals in the middle of the periodic table (*Au*, *Ag*, *Cr*...). By applying a DC voltage between the metal target (or cathode) and the conductive plate upon which substrates are deposited (anode), the atoms of the feeding gas are ionized and a glow discharge (plasma) is formed. The ions and electrons forming the plasma are, thus, accelerated impacting on the target. The bombardment process causes the sputtering of the atoms from the target through an energy and momentum transfer: if the atoms gain enough energy to break the binding forces of the mate-

rials, they can leave the target and be sent into the gas phase. Therefore, sputtered atoms start to accumulate at the surface of the substrates placed in front of the target giving place to the film formation. The sustainment of discharge is maintaining thanks to the secondary electrons which are also emitted from the target after the ions bombardment. In order to intensify the ion bombardment and to increase the ionization efficiency, a permanent magnet is placed in front of the target. One pole is positioned in the center of the target whereas the second pole, composed of a series of magnets, is located along the outer ring of the target. This configuration creates a magnetic field capable to keep the secondary electrons and generate a dense plasma in proximity of the target. As result, the gas discharge can be broken down at operating pressure (typically 10^{-3} mbar, compared to 10^{-2} mbar) and discharge voltage (typically ~ 500 *V*, compared to $\sim 2-5$ *V*) lower than in basic sputtering process [90, 91].

The magnetron sputtering system used in the laboratory is the model Q300T-D provided by *Quorum Technologies*, which allows the sequential sputtering of two metals without breaking the vacuum [92]. The Fig. 3.1(b) shows the instrument during operation in Argon gas discharge. The samples are placed on a rotating plate whose velocity can be regulated from 14 *rpm* to 38 *rpm*. The rotation assures a uniform deposition on the surface of the substrates to be coated. The deposition is controlled by a quartz crystal microbalance which measures the coating thickness in real-time. The system allows setting different profiles in which is possible to change the target sequence, the time deposition, and the current used during the process. The most used one is the dual film monitor (FTM) profile in which the deposition stops when the required thickness is achieved.

3.2 Plasma Treatment System

As discussed in the Sec. 4.2, the plasma treatment of smooth metallic surfaces played the central role in the formation of the nano-structured silver films. The instrument used for this scope is the Basic Plasma Cleaner

(model PDC-32G-2) provided by *Harrick Plasma* which is based on the generation of an Inductively Coupled Plasma (ICP) by a RF power supply. The plasma system is generally used for cleaning processes but in last years it has also great interest in other research areas such as biomaterials [93, 94], nanotechnology processes [95–97], photovoltaic/solar cell materials [98] and PDMS surface modification [99, 100]. Indeed, the type of interaction between the plasma and the surface is dependent of many parameters: the RF power used to exited the plasma, the pressure, the type of process gas, the nature of the sample and the amount of the time the surface is exposed to the plasma.
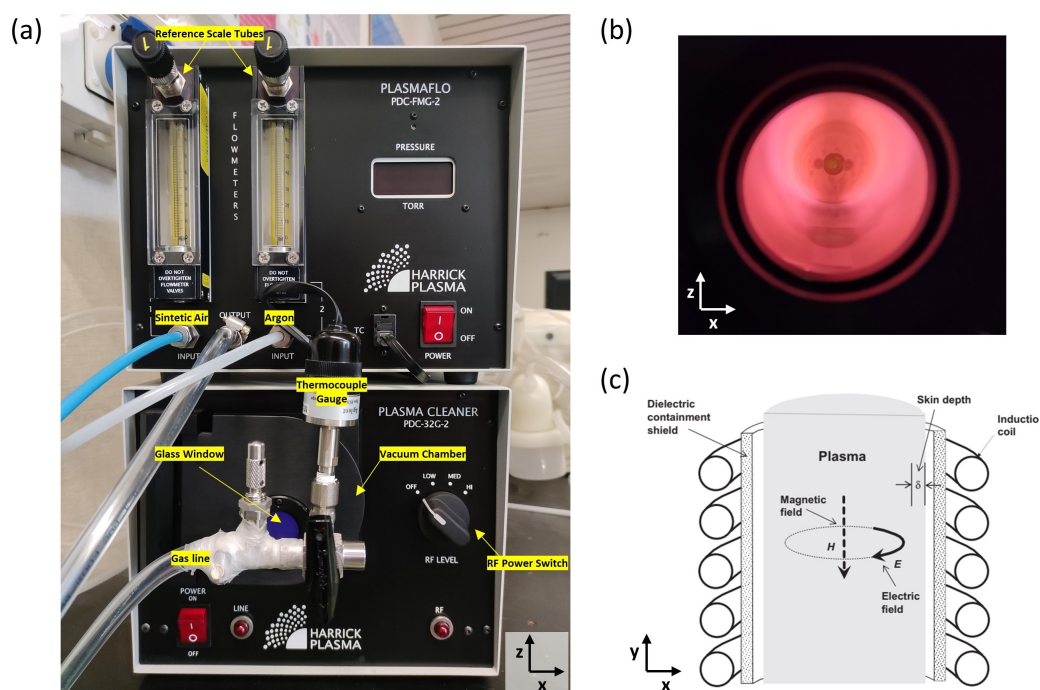
Figure 3.2: (a) Plasma system connected to the flowmeter PlasmaFlow (*Harrick Plasma*); (b) Photograph of the plasma seen from the glass window and produced using Synthetic Air as process gas. In this case, the glow discharge takes the typical pale red colour; (c) RF magnetic field (**H**) and RF electric field (**E**) created inside the vacuum chamber by applying RF power to the helical coil through the cylindrical dielectric tube [101].

The working operation of the plasma system is simple and briefly de-

scribed below. The samples are placed on a quartz tray in a cylindrical chamber that is firstly evacuated and then filled with a process gas. As shown in Fig. 3.2(a), the chamber is connected via a gas line to a flowmeter (PlasmaFlow by *Harrick Plasma*) which enables the quantitative control of the gas flow rate (in our case Synthetic Air or Argon). As a matter of fact, it is possible to make a single gas flows or a mixture of both through the corresponding flow regulator. The flow rate is read in *mm* from a 65 *mm* reference scale tube: this value is then converted in *mL/min* through a conversion table for the most common process gases used, metered at the pressure of 10 *psig*. The indirect-read scale allows the use of the instrument to a wide number of gases. The Table 3.1 shows the correlation

Table 3.1: Conversion table for Scale Reading of Flow Rate.

Scale Reading (mm)	Air 10 psig* Flow (mL/min)	Argon 10 psig* Flow (mL/min)
65	77.1	67.3
60	68.3	58.3
55	59.0	50.9
50	51.5	43.4
45	44.8	37.4
40	38.9	31.5
35	30.7	25.0
30	25.7	20.4
25	20.4	16.6
20	16.2	13.2
15	12.3	9.5
10	9.2	7.3
5	5.7	4.1

*The pounds per square inch gauge (psig) indicates the pressure relative to the atmospheric pressure resulting from a force of one pound-force applied to an area of one square inch. 0 psig =1 atm; 10 psig ≈ 1.7 atm.

table to convert the floating position (*mm*) to a flowrate (*mL/min*) for the

gases used: Air and Argon. The process gas is, thus, injected in the vacuum chamber and kept at low pressures (typically around 0.5 *torr*) through the vacuum pumping. The obtained pressure is displayed directly on the flowmeter and monitored via a thermocouple gauge connected directly to the chamber. Once the pressure in chamber is stabilized, the glow discharge can be generated selecting the proper radio-frequency (RF) power (see Fig. 3.2(b)). The RF power level can be adjusted using a three-way selector switch: Low (6.8 *W*), Medium (10.5 *W*) and High (18 *W*) [102]. Throughout all the process, the plasma is maintained on the continuum gas flow to render more efficient the transport of ion species towards the sample.

The mechanism behind the formation of the plasma in the chamber is summarized in Fig. 3.2(c). The inductive source arrangement installed in the instrument is based on a cylindrical geometry. When the RF power is applied, an alternating current of $8 - 12$ *MHz* is supplied to a helical coil surrounding the chamber. According to Ampere-Maxwell law, the flowing of RF current through the coil induces a time-varying magnetic field **H** within the chamber. In turn, the variation of **H** induces a variable electric field **E** by Faraday's law, which accelerates the free electrons and sustains the plasma. The main energy transfer mechanism from electric fields to plasma electrons occurs within a skin depth layer of thickness δ near the chamber's walls by two effects: (a) Joule heating (collisional dissipation) in which the electrons are accelerated by electric field **E** and collide many times, and (b) stochastic heating (collisionaless process) in which the accelerated electrons in skin depth layer can penetrate the bulk plasma and contribute to ionization [103–105].

3.3 Confocal Raman Microscopy and Atomic Force Microscopy

The setup used throughout the thesis for the spectroscopic and topographical measurements of the nanostructures is an integrated system (alpha300

RA, *Witec*) that combines an Atomic Force Microscope (AFM) along with an inverted confocal Raman Microscope. The microscopes can operate individually for Raman/AFM measurements or in conjunction for TERS ones. The single parts of this equipments are briefly described below.

3.3.1 AFM Configuration

The principle operation of the AFM is well known and can be found in details in various references [106–108]. This section will describe the main components of the system when used in AFM mode. As shown in Fig. 3.3, the upper part of the microscope is equipped with an XY positioner (U1) for coarse alignment of the sample in the x- and y-directions. The positioner
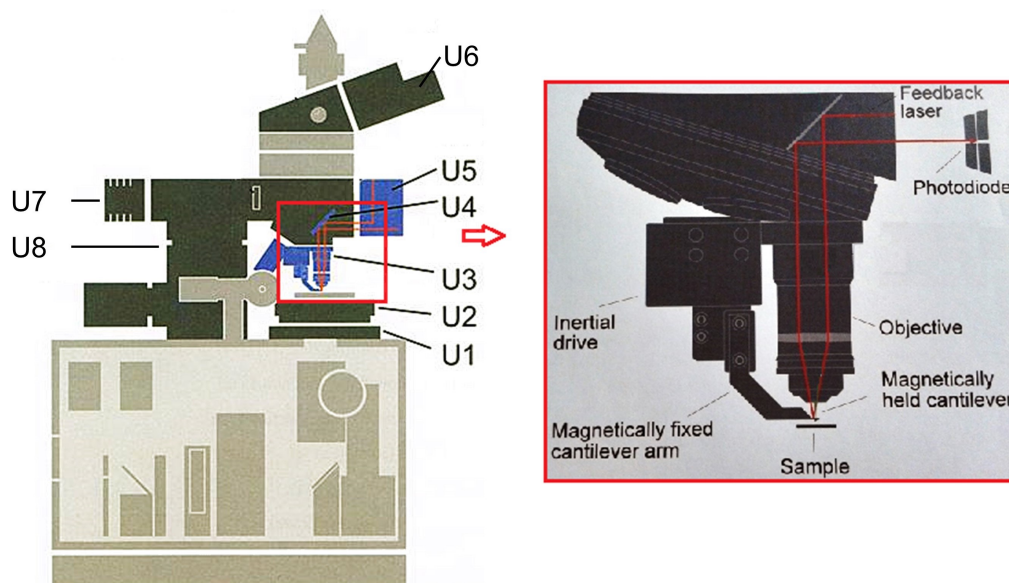

Figure 3.3: Schematics of the upper microscope of the Witec alpha300 RA. The inset shows the beam path of the beam deflection laser highlighted in red.

is mounted underneath the scan stage (U2) on which the sample is placed. The scan stage can be moved by manual micrometers for 20 *mm* in both directions or automatically by a piezo-electrical motor along the 3-axis for a maximum scan range of 100 *μm* in x- and y-direction and 20 *μm* in

the z-direction. The sample is top-illuminated (U7-Light Source) through an objective 20×/0, 4, ∞/0, 17 with WD 3,8 mm (U3) connected to a CCD video camera (U6). The video camera image is fed to the video control window. To perform AFM measurements, the tip is magnetically held to the cantilever. In turn, the cantilever arm is magnetically fixed to an inertial drive that allows its highly precise positioning in the x, y and z directions. In the approach process, the AFM tip is neared to a certain distance upon the sample surface by the microscope z stage (U8). The stage moves the entire upper microscope with a minimum step of 10 *nm* and for a maximum range of 30 *mm*.

AFM operation modes

During an AFM scan, the interaction of the tip with the surface of the sample causes a deflection of cantilever that is measured by beam deflection (OBD) method: a feedback laser beam with wavelength of 980 *nm* is focused on the cantilever, reflected and guided through a dicroic mirror (U4) to a quadrant photodiode (U5) that detects the signal. While the cantilever is at rest, the laser spot is positioned in the center of the four quadrants. When the tip interacts with the sample, the cantilever bends and the position of the laser spot changes. The system monitors the change of this position in real-time and a feedback system uses it to correct the vertical position of the sample with respect to the tip. Depending on the nature of tip-surface interactions, the AFM can operate in three modes to acquire the topography of the sample[106, 109]:

(*i*) **Contact mode**: In contact mode, the tip is kept at constant distance from the sample by the feedback mechanism. This feed-back signal is then used to reconstruct the topography of the surface. The vertical deflection of the cantilever Δx is directly proportional to forces acting on the tip, according to Hooke's law ($F = -k\Delta x$). In fact, as the tip approaches the surface, it normally feels first an attractive force, becomes unstable and, then, jumps into contact with the surface. As the tip continues to be pushed towards the surface, the interaction

moves into the repulsive regime, that is the region where the contact mode operates (Fig. 3.4(a)). This weak force is revealed by using soft cantilevers with a spring constant typically small as $0.01 - 1\ N/m$. For TERS microscopy, the contact-mode AFM is widely employed due to its simplicity and versatility. In fact, the reduced tip-sample distance promotes a highest near-field Raman enhancement. On the other hand, the strong contact can easily damage the tip during raster scans. In addition, the samples need to be fixed on the substrate to avoid a dragging by the tip and, thus, this operation is not suitable for soft materials;
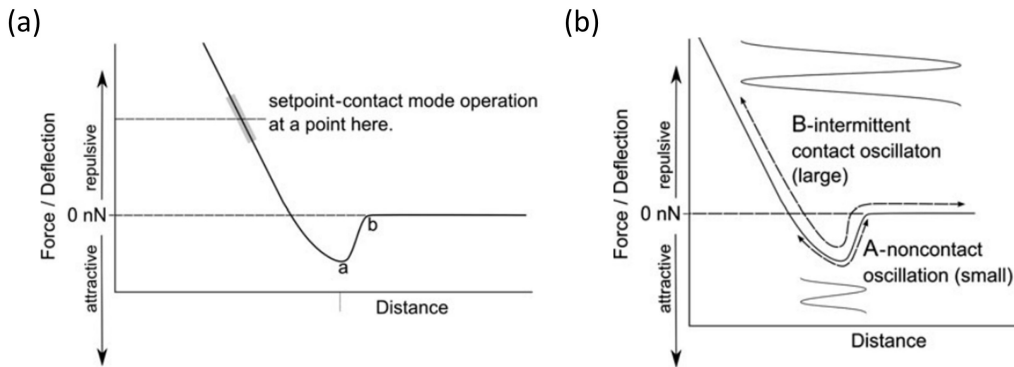

Figure 3.4: Force-distance curve showing (a) contact (repulsive region) scanning regime and (b) different operating oscillating regime [106].

(*ii*) **Intermittent oscillating mode**: In the intermittent/tapping/AC mode, the cantilever is forced to oscillates close to its resonant frequency with a free amplitude A_0. In this case, the standard cantilever arm is substituted with one that incorporates a piezo actuator for the modulation of the cantilever z position. As the cantilever approaches the surface, the oscillating amplitude is damped to a value A, which depends on the distance to the surface. The ratio $r = A/A_0$ defines the damping of the amplitude while the tip is in contact with the surface and is proportional to the applied force. The detected change in amplitude is used in the feedback circuit to maintain the tip at a fixed distance from the sample surface. In this mode the tip oscillates

with a large amplitude and, thus, the tip-sample interaction passes through the attractive regime into the repulsive regime at each oscillation cycle (see arrow B in Fig. 3.4(b)). So, in order to detach the tip from the surface, the AC cantilevers are stiffer than those for contact mode with elastic constant $k > 1 \, N/m$. In addition, in order to not be resonant with any other mechanical component of the instrument the resonance frequency of cantilever has always values $f_0 > 50 \, kHz$. In addition to the amplitude signal, the tapping mode enables to acquire the delay in the phase of the probe oscillation. The phase shift depends on the visco-elastic properties of the sample as well as on the adhesive potential between the sample and the tip. Thus, the phase image is a useful tool to identify eventually domains of varying material properties and is usually used to characterize soft samples at high resolution.

Because of the large oscillating amplitude, TERS enhancement occurs only at the moment when the tip contacts the sample in one oscillation cycle. As a result, the observed Raman scattering intensity in one oscillation cycle tends to become small compared to that seen in the contact-mode-based TERS. Anyway, it is widely used because it reduce the damage of tip and sample;

(*iii*) **Non-contact mode**: In the non-contact mode the cantilever oscillates at its resonance frequency with a small amplitude to remain in the attractive region (see arrow A in Fig. 3.4(b)). The interaction tip-sample causes a resonance frequency shift of the oscillating cantilever. The measurement of the resonance frequency shift provides a precise measurement of the tip-sample force both in attractive and repulsive force region. To realize the stable resonance oscillation, the Q factor of the cantilever resonator is required to be as high as $1000 - 10000$. In air, typical Q factor of *Si* cantilever decreases down to the orders of 100 due to the friction of air. Thus, high vacuum condition is usually preferred for the operation. This limits the use of non-contact-mode in TERS microscopy which is in most cases performed in air.

3.3.2   Spectroscopy Configuration

The Fig. 3.5 shows the schematics of the beam path when the inverted confocal Raman microscope is used.
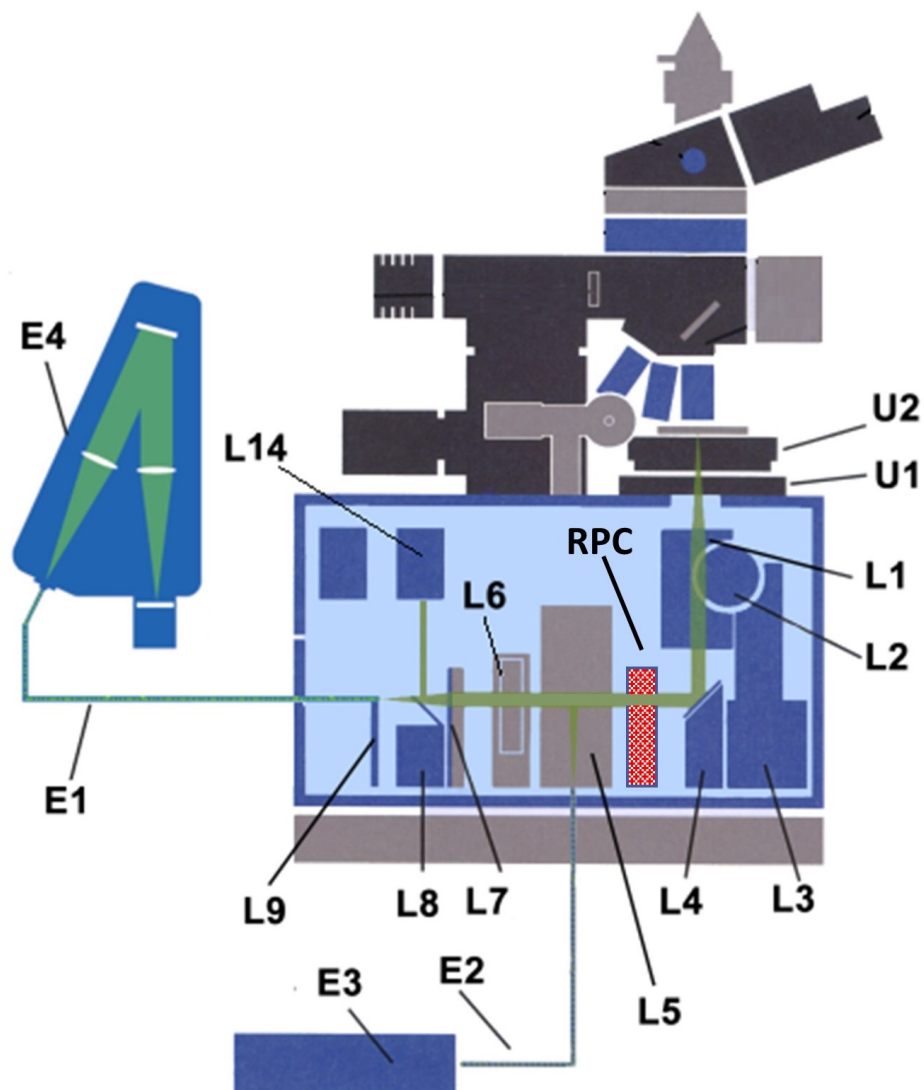

Figure 3.5: Schematics of the beam path of the Witec alpha300 RA in spectroscopy mode. The red highlighted unit (RPC) is introduced when the microscope operates in TERS configuration.

As in AFM mode, the sample to be analysed is positioned on the scan

stage (U2) that can be moved by the XY positioner (U1). The excitation source (E3) is provided by a frequency-doubled Nd-YAG laser (λ = 532 *nm*) and coupled (L5) to the instrument through an optical fiber (E2). The laser beam is collimated and directed by a mirror (L4) to an objective (L1) that can be manually moved along z-direction by the adjustment knob (L2) or automatically by a motorized x, y, z positioning unit (L3). The stepper motor has a step size < 0.1 μm along the x- and y-axis and a minimum step size < 0.05 μm along the z-axis. Back-scattered photons are collected by the same objective and filtered by an edge filter (L6). So, the inelastic Raman photons are focused through the tube lens (L7) to a flip mirror (L8) that allows directing the light to a fiber connector (L9) or to a CCD (L14) for the video visualization of the samples on the computer. The fiber connector is located such that the multi-mode fiber (E1) is situated with its core in the focal position of the tube lens. The system is equipped with three different multi-mode fibers with core diameters of 25, 50 and 100 μm. The core diameter acts as the pinhole of the confocal microscope. The fiber guides the radiation to the spectrometer (E4) which is supplied with a rotatable turret with two gratings of diffraction: a 600 g/mm and 1800 g/mm grating. The spectrometer fits two types of back-illuminated CCD cameras (1024x127 pixel array with pixel size 26 $\times$ 26 μm^2) operating in visible range (DV401-BV) and in near-infrared (DV401-BR-DD). The CCD cameras are cooled thermoelectrically at $-60°C$ to minimize the noise level.

TERS Configuration

When the system is used in TERS configuration, an additional unit comprised of a Radial Polarization Converter or RPC (*ARCoptix*) is introduced into the beam path (see Fig. 3.5). The device converts the incident linearly polarized light into a beam with radial or azimuthal polarization distribution by using the twisted nematic effect (TN-effect) [110]. As shown in Fig. 3.6(a), the unit is composed of three elements:

- the phase shifter introduces phase retardation between both sides of the RPC. This element is AC power supplied and can produce a

phase shift when a proper voltage in the range of $0 - 10$ V is applied;

- the polarization rotator acts as a half-wave plate. It is a TN cell that can rotate the entrance polarization by $90°$. When a bias of 8.8 V is applied, instead, the direction of the incident polarization does not change;
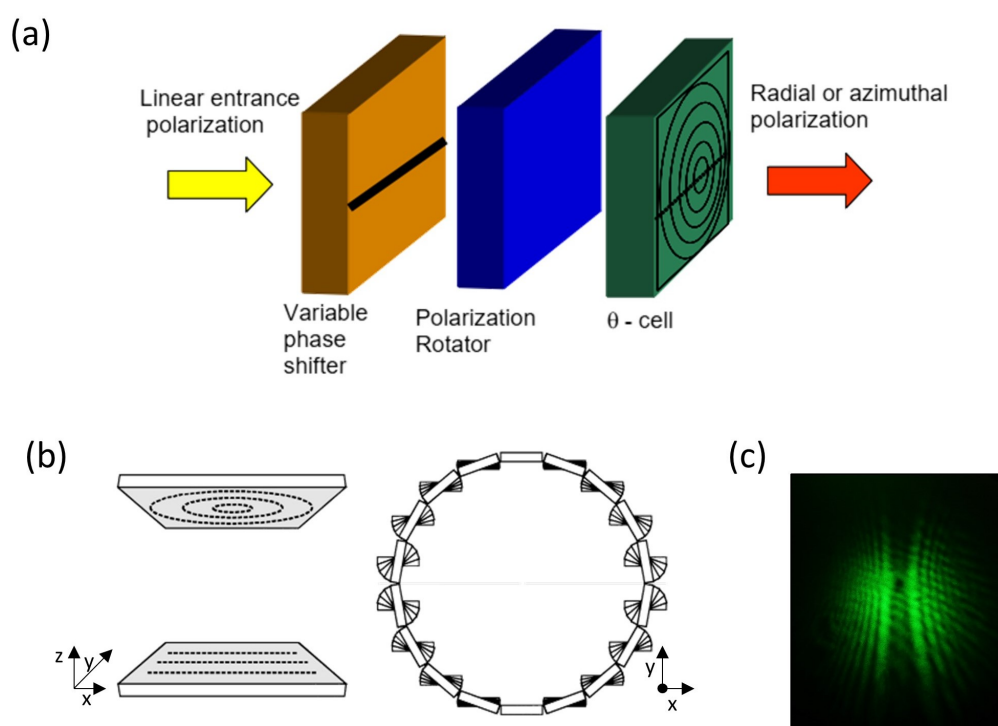
(a)

(b)   (c)

Figure 3.6: (a) Configuration of the radial polarization converter (RPC). The laser beam enters from the phase shifter and exits from the θ-cell either radial or azimuthal polarized [111]; (b)Alignment layers of the θ-cell (left) and the resulting orientation of the LC molecules in the cell seen from above (right) [82]; (c) Diffraction pattern of the radial polarized laser beam.

- the θ-cell is a second TN cell that rotates the entrance polarization by an angle of 2θ. The cell is composed of two plates linearly and circularly rubbed, filled with twisted nematic LCs (Liquid Crystals) distributed with a twist angle θ given by the local alignment layers

(see Fig. 3.6(b)). The direction of the linearly rubbed alignment layer determines the cell axis.

The desired state of polarization (radial or azimuthal) depends on the polarization of the incident light on the θ-cell. If the polarization rotator is switched on, the entrance polarization is parallel to the cell axis of the θ-cell and a radially polarized beam can be obtained at the exit. This is the polarization used in our case. As described in Sec. 2.3.2, the radial polarization promotes the excitation of LSPR along the tip axis in the bottom-illumination TERS configuration. The Fig. 3.6(c) shows the obtained diffraction pattern of the radial polarized laser beam.

In addition to the RPC unit, the bottom microscope is also equipped with an Olympus 100× oil immersion objective with a high numerical aperture (NA = 1.4). In a typical AFM-TERS experiment, a freshly prepared TERS probe is magnetically mounted on the cantilever arm of the upper microscope as shown in Fig. 3.7(a). After the first AFM adjustments, the tip
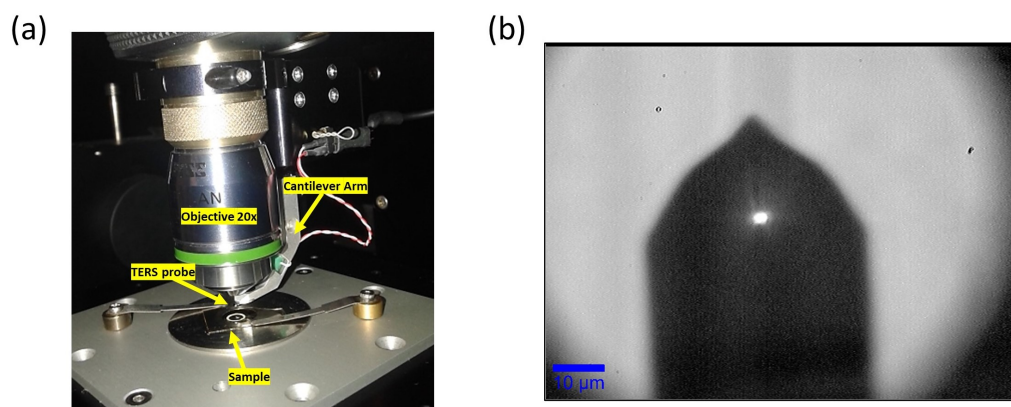
(a)

(b)

Figure 3.7: (a) Photograph of upper part of the system when the TERS tip is mounted; (b) Video image showing the intense sparkle at the apex of the tip seen through the 100× objective.

is automatically brought nearby of the sample surface by the z-movement of the microscope Z stage. Once the approach is completed, the TERS tip needs to be aligned with the excitation laser of the inverted microscope. The system allows to finely focus the laser beam on the tip with the posi-

tioning unit (L3). The optimal position for TERS measurements is revealed by monitoring the back-reflected light of the laser beam in the video control and the Raman spectrum in real-time. In fact, when the laser focus is positioned to the apex of the tip, the excitation of LSPRs is maximised and an intense sparkle can be observed (see Fig. 3.7(b)). The enhancement is also confirmed by an increased intensity of the characteristic Raman peaks of the analysed sample.

3.4 UV-Vis spectroscopy

The UV-Vis spectroscopy is a technique used to characterize the optical response of the liquid/solid analytes and, in the context of SERS, the metallic substrates in the ultra-violet (UV) and visible (Vis) spectral range. A typical implementation of UV-Vis spectroscopy consists in measuring the wavelength dependence of the intensity I transmitted through the sample. The parameter evaluating the percentage of transmitted light is the transmittance $\%T$ defined as $\%T = I/I_0 \times 100$ where I_0 is the reference intensity. If the sample is solid, I_0 corresponds to the incident light. When the sample is liquid and, thus, inserted in a container (cuvette), I_0 corresponds to the transmitted light through the void cuvette. The measurement of the transmittance enables to calculate the absorbance of the analyte through the logarithmic function:

$$A = -\log_{10}(T) \tag{3.1}$$

The absorbance is widely used to determinate the concentration of an unknown solution following the Beer-Lambert law which states that the absorption of light by a substance is proportional to its concentration in solution as follows:

$$A = \epsilon l c \tag{3.2}$$

where ϵ is the molar absorptivity coefficient ($M^{-1}cm^{-1}$), l is the optical path length of the light through the cuvette containing the solution (*cm*) and c is the molar concentration (*M*) [112]. In some cases, the UV-Vis

spectrophotometer can also be configured to measure the reflectance of a sample defined in percentage %R as the ratio between the intensity of light reflected from the sample I and the intensity of light reflected from a reference material of high reflectivity I_0.

In the so-called single beam spectrophotometer, the reference intensity I_0 is acquired by removing the sample from the beam path. The instrument used in this work thesis, instead, is a double beam spectrophotometer (Lambda 35 by *Perkin Elmer*) that enables to measure the reference beam in a different channel as shown in Fig. 3.8. The system works in a wavelength
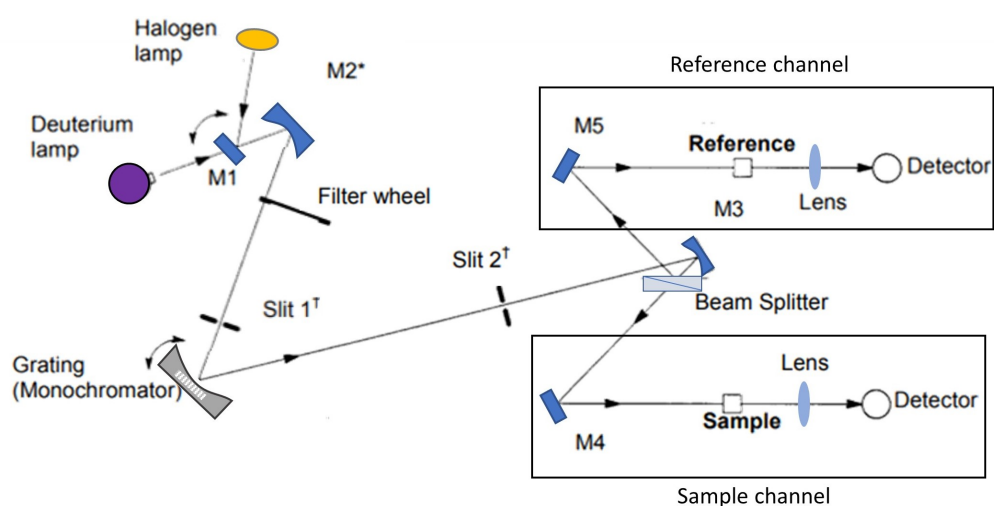

Figure 3.8: Optical system of the Lambda 35 spectrometer. The mirrors M are: $M1$, $M4$ $M5$ are plane, $M2$ toroidal and $M3$ spherical. The mirror $M1$ rotates to change the incoming source radiation [113].

range of 190-1100 *nm* and a variable bandwidth range of 0.5 to 4 *nm*. The working spectral range is covered by two radiation sources, a deuterium lamp and a halogen lamp, that change automatically at 326 *nm*. The radiation coming from one of the source is reflected by a mirror ($M2$) and directed to the inlet slit (Slit 1) of a monochromator which consists of a holographic concave grating with 1053 *lines/mm* in the center. Before to reach the slit, the beam is filtered with a proper filter depending on the wavelength being produced. The filter wheel is driven by a stepping motor which is synchronized with the monochromator. The grating disperses

the radiation to produce the spectrum. The rotational position of the grating selects a segment of the spectrum, reflecting this segment through the exit slit (Slit 2) with a spectral bandpass of 1 *nm* to the mirror *M*3. Each monochromatic beam is then split into the two channels (beam and reference) by a beam splitter and reach the photodiode detector.

When a solid sample is analysed, the transmitted or reflected beam can not be fully picked up by the detectors. In fact, uneven, rough or spherical surfaces can deviate the beam resulting in a reduced signal. Therefore, to obtain a correct transmittance and reflectance measurement, the instrument is equipped with an integrating sphere (RSA-PE-20) that is inserted in the beam channel as shown in Fig. 3.9(a). In this case, the sample is
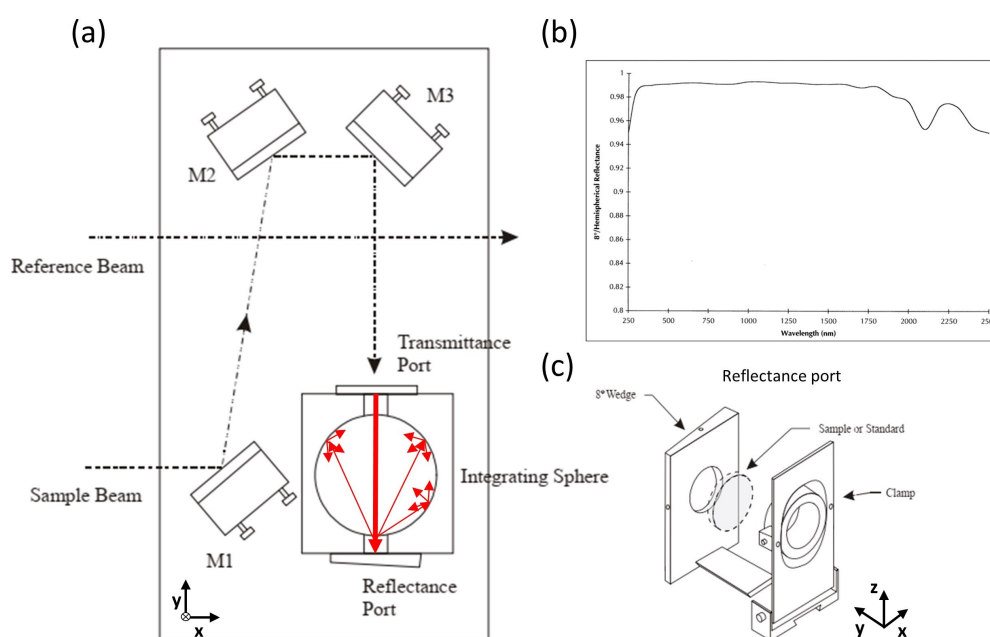
Figure 3.9: (a) Optical setup of the RSA-PE-20 accessory; (b) Reflectance spectrum of the Spectralon; (c) Frame port and holder sample mounted in front of the Reflectance Port [114].

placed against the sphere on the Transmittance (or Reflectance) Port and the beam transmitted (or reflected) by the sample is reflected onto the internal reflective surface of the sphere before reaching the detectors inside the sphere. The sphere's internal surface is made of the polymer Spec-

tralon, which offers levels of diffuse reflectance approaching 100%. The material has the same thermal stability as the high-density polyethylene, is chemically inert and highly hydrophobic. The range of efficiency of the Spectralon covers the whole region of UV, visible and NIR. The reflectance is greater than 99% between 400 and 1500 nm and 95% between 250 and 2500 (Fig. 3.9(b)). During the direct transmittance measurements where the sample is placed at the Trasmittance port, the Reflectance port is closed by a reference sample made of Spectralon. In addition, the diffuse transmission can be measured by replacing the port frame of 8° (see Fig. 3.9(c)) with one of 0°. In similar way, is possible to acquire measurements of overall or diffuse (that excludes the specular component) reflectance by placing the sample at the Reflectance Port in front of the proper port frame of 8° or 0°, respectively [114, 115].

3.5   X-ray diffraction

X-ray diffraction (XRD) is a versatile and non-destructive technique based on the X-ray scattering that provides information about the crystallographic structure (orientation, shape, size, crystal defects), the crystalline phases and, thus, the chemical composition of a specimen. It is generally employed to characterize crystalline or partially crystalline (*i.e.* with a periodic structural order) solids but it can be also employed to examine amorphous materials. The X-rays are electromagnetic waves characterized by wavelengths ranging from 0.2 *nm* to 10 *nm* comparable to the inter-atomic spacing of the crystalline solids. When the X-ray beams are incident on a crystalline solid, they are diffracted by the crystallographic planes as illustrated in Fig. 3.10. As result, if the diffracted waves constructively interfere, intense reflected X-rays can be produced . The condition to keep these beams in-phase is given by the Bragg's law that is derived by considering that their path difference ($SQ + QT = 2PQ \sin(\theta)$) has to equal

one or multiple X-ray wavelengths ($n\lambda$):

$$n\lambda = 2d\sin(\theta) \tag{3.3}$$

where λ is the incident wavelength of the X-rays, θ the angle between the incident beam and the crystallographic plane, d is the perpendicular distance between pairs of adjacent planes and n is the order of the reflection. Thus, by knowing the spacings of crystallographic planes d by the diffraction method, we can determine the crystal structure of materials. For example, the plane spacing of cubic crystal d_{hkl} is related to the lattice parameter (a) by the following equation:

$$d_{hkl} = \frac{a}{\sqrt{h^2 + k^2 + l^2}} \tag{3.4}$$

where the Miller indices (hkl) represent a series of parallel planes in a crystal with spacing of d_{hkl} [116].
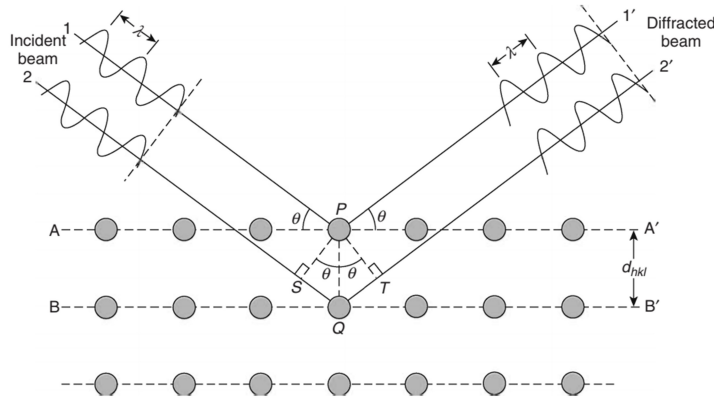

Figure 3.10: Bragg diffraction by crystal planes. The path difference between beams 1 and 2 is $SQ + QT = 2PQsin(\theta)$ [116].

The instrument used to investigate the specimen is composed, essentially, by a X-ray monochromatic radiation source and a detector.

The X-Ray source is based on a X-ray tube *i.e.* a vacuum tube converting the electronic energy into X-ray radiation and heat. The electrons produced by a hot filament (catode) are accelerated by the high voltage towards a

metal target (anode) generally made of *Cu*, *Al*, *Mo* or *Mg*. This collision promotes the excitation of an electron from the inner shell of the atom to a higher-energy state. The electronic transition of an electron in outer shell into the so-formed vacancy produces the emission of X-ray with a specific wavelength. The X-ray tube produces a radiation characterized by a continuous range of wavelengths superimposed by sharp intensity maxima at certain wavelengths (left panel of Fig. 3.11(a)). These peaks identify the characteristic X-rays that in generally correspond to the K_α and K_β lines, which are the strongest electronic transitions. The monochromatic radiation incident on the specimen is, thus, generated by using an absorbing material, such as Nichel, that filters out the other X-rays wavelengths (right panel of Fig. 3.11(a)).
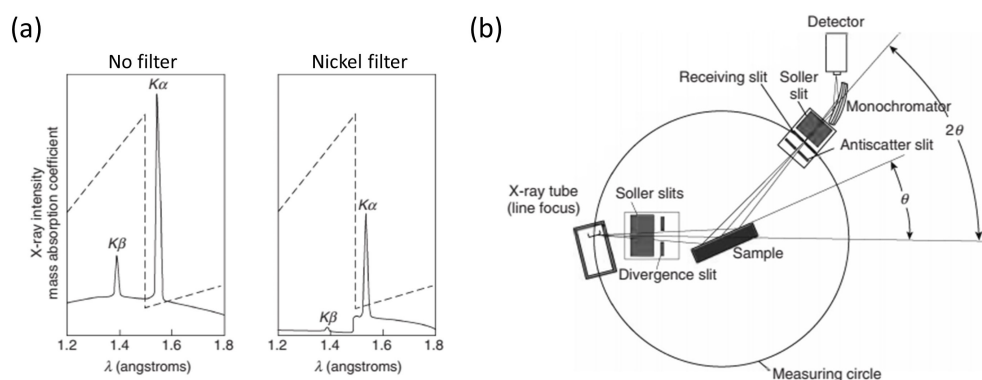

Figure 3.11: (a) Spectra of X-ray radiation before (left) and after (right) filtering. The dotted line indicates the sharp increase of absorption at a slightly shorter wavelength than the K_α radiation that enables a nickel filter to generate single-wavelength radiation; (b) Geometric arrangement of an XRD diffractometer. The angle θ is the angle formed between the crystallographic plane and the incident beam [116].

As shown in Fig. 3.11(b), the so-produced radiation from the X-ray tube passes through special slits that collimate and diverge the X-ray beam towards the sample. The diffracted X-rays form a convergent beam at the receiving slits (RSs) before they reach a monochromatic filter that removes the unwanted wavelengths and decreases the background radiation originating within the specimen. Thus, the diffracted beams are revealed by a

detector that, depending on the geometry arrangement of the diffractometer, can be fixed or rotate around the axis perpendicular to the plane of the figure of Fig. 3.11(b). The spectrum of the diffraction intensity versus the angle 2θ (diffraction pattern) is obtained by continuously changing the incident angle of the X-ray beam. Diffractometry enables us to identify the crystal structure and quality by analyzing and, then, comparing the spectrum with a database containing the diffraction spectra of known crystalline substances. [116]

In this work thesis, the X-ray diffraction profiles are obtained with *Ni* filtered *Cu K$_\alpha$* radiation (λ = 0.1542 *nm*) by using an Empyrean diffractometer by PANalytical with continuous scans of the 2θ angle and a scanning rate of $0.02° \; s^{-1}$.

3.6   SEM Analysis Images

Scanning Electron Microscope (SEM) is another method used to reveal the morphology of the plasmon-active nanostructures. The SEM images were acquired with *Zeiss Merlin VP* system at the accelerating voltage of 10 kV and different magnifications. In a first step, all the images are processed by *ImageJ* software. In the pre-processing operation, the image noise is reduced by using the *Smooth* filter which replaces each pixel with the average of its $3x3$ neighborhood. The image contrast is then enhanced to better distinguish the surface features from the background. Thus, a smaller area of the image is selected and analysed in detail. The Fig. 3.12(a) shows the obtained grey-scale image followed the pre-processing operation. The next step is based on the creation of two masks. The first mask provided segmented areas delimiting the borders of each nanostructure. The segmentation process was determined by using the *Find Maxima* tool which determines the local maxima in the image and creats a binary format of the same size with one marked segmented structure per maximum (see Fig. 3.12(b)). In this way, it is possible to delineate the edges of the objects of interest which would be otherwise indistinguishable when they

are in contact. The second mask consists of the conversion of the original greyscale image in binary format by adjusting the lower and upper-level threshold (see Fig. 3.12(c)). The final image is obtained by overlapping the two masks through the AND logical operator (see Fig. 3.12(d)).
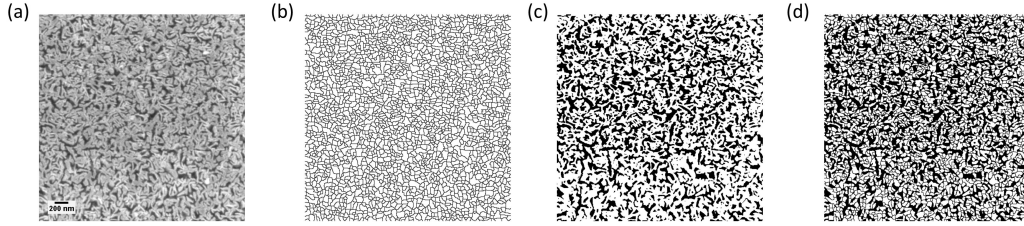

Figure 3.12: Example of SEM image processing relative to the cantilever region of a tip obtained with plasma-induced dewetting method: the tip was covered by 30 *nm* of *Ag* and treated with 60 *s* of Synthetic Air plasma and 30 *s* of Argon plasma: (a) Greyscale image 512 × 512 *pixels*; (b) Segmented areas marked (Mask 1); (b) Binary image (Mask 2); (d) Result of AND operation applied between Mask 1 and Mask 2.

The resulting binarized image is then used to determine different statistical surface parameters:

- The dimension of the objects is calculated from the *Area* calculated via the *Analyze Particles* command of *ImageJ*. The size distribution of the nanostructures is achieved by calculating the diameter of a circle whose area equals the projected area of the structure:

$$d_{EQPC} = 2 * \sqrt{\text{Area}/2\pi} \tag{3.5}$$

   which is arguably the best measure of the overall structure size when the objects have irregular shapes [117].

- The characteristic wavelength λ_c of the long-range order is determined through the PSD approach (see Sec. 4.2.2). The PSD is calculated by the Eq. 4.21 where the 2D FFT of the image is obtained through the Matlab built-it functions *fft2* and *fftshift*. After that, the rotational average of PSD is determined by a custom-made Matlab

routine and fitted by a Lorentzian function in OriginLab software in order to extrapolate the ν_C value and, then, calculate $\lambda_c = 1/\nu_c$.

- The porosity p of the substrate is defined as the ratio of the percentage of the black area:

$$p = \frac{\text{number pixels black area}}{\text{number total pixels}} \qquad (3.6)$$

where the numbers of pixels in the white and in the black areas were counted through the Matlab built-in function *bwarea* [118].

Chapter 4

Development of Coral-like probes for TERS applications

Part of the results shown in this chapter were published in Capaccio A., Sasso A., Tarallo O. and Rusciano G., "Coral-like plasmonic probes for tip-enhanced Raman spectroscopy", *Nanoscale*, 12(48), 24376-24384, **2020**.

4.1 Introduction

As discussed in the Sec. 2.3, a crucial role in the TERS measurements is played by the TERS-probe which consists of an AFM tip properly modified. The enhancement mechanism is strongly dependent on the geometry and the type of plasmonic material of the probe. By modifying these parameters, it is possible to manipulate the conditions necessary to excite the plasmon resonance modes in nano-antennas that contribute to the local field enhancement. In addition, the apex tip dimension determines the spatial resolution of the TERS imaging that, generally, improves for tips with smaller diameters [86]. The TERS probes can be found commercially by manufactures as Horiba [119] or Bruker [120], but they are commonly home-made prepared by using specific fabrication techniques. The main challenge in the development of performing TERS probes is producing reproducible tips that are both suitable for the nanoscale SPM imaging

and for the resonant EM enhancement. Moreover, another issue concerns the exposition of the tip to the air or other environments that can reduce the tip lifetime and its plasmonic activity. Thus, many strategies have been proposed both to fabricate high-quality TERS probes and to extend the tip lifetime [77, 121]. The different strategies reported in literature are mainly based on the fabrication of sharp smoothly or structured tips. Sharp smoothly metal tips can be fabricated by using the electrochemical etching of metal wires (*Ag* or *Au*). This method allows to produce cone-shaped tips with an apex diameter ranging from 10 to 30 *nm* [75]. These tips are generally employed in the STM-TERS systems. An example of silver tip produced by electrochemical etching is shown in Fig. 4.1(a). Other etching-based methods have been developed in last years to get even sharper tips with quite relevant efficient EM enhancement. Anyway, the reproducibility of these techniques is typically limited by the variations of etching parameters and metal wire crystal structure [86]. Furthermore, it has been found that for silver smooth tips the scattering efficiency is reduced. The Fig. 4.1(b) shows the calculated scattering spectrum of a silver smooth tip: any resonance peak is visible. The tip does not act as a plasmonic antenna
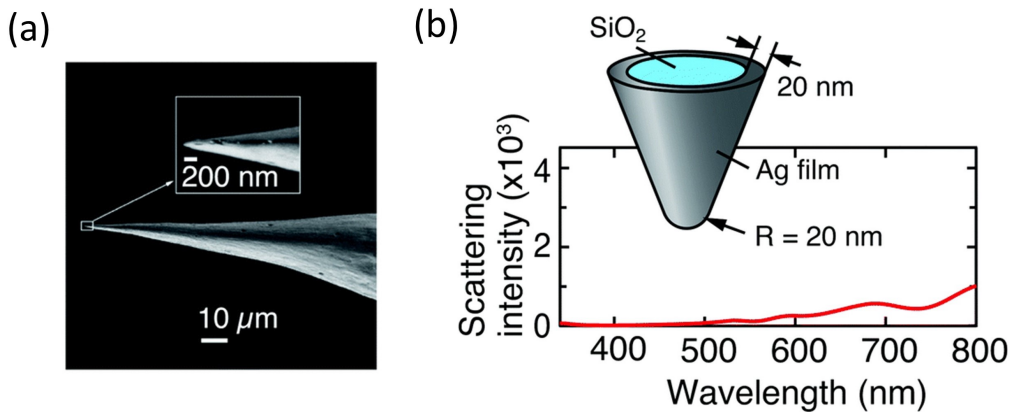

Figure 4.1: Example of sharply smooth tip. (a) SEM image of a silver tip tapered by electrochemical etching; (b) Calculated scattering spectrum of a sharp smooth tip [86].

but, rather, as a waveguide where the plasmons propagate non-radiatively

along the tip shaft. A local field enhancement is still present at the apex of the tip thanks to the lightning rod effect [122]. Therefore, in order to achieve higher enhancement factor, smooth tips are typically coupled to a metallic substrate (gap-mode) in TERS experiments [123]. The gap-mode scheme is surely advantageous to increase the detection sensitivity but its applicability is limited to very thin samples (≈ 10 *nm*) [77]. So, alternative methods have been developed to produce performing TERS tips that can eventually operate also in no gap mode and extend the applicability to thicker samples. Taguchi *et al.* [122] have demonstrated that dielectric tips covered by multiple metal grains can act as an efficient plasmonic antenna and that the TERS enhancement is maximized by the optimization of the grains number's. The Fig.4.2(a) shows the simulated scattering spectrum for a probe with 16 connected (dashed line) and disconnected (solid line) particles. In both cases, a pronounced peak is visible around $450 - 500$ *nm*, although a higher enhancement is provided for the probe with disconnected particles. Notably, the broadening of the resonance appears only when a nano-gap between adjacent grains is present. Whereas, when this gap is reduced, multiple peaks appear and the intensity of resonance decreases. This demonstrates that the nano-gaps play an important role in tuning plasmon resonance as well as in increasing the enhancement [122].

The most used technique to obtain nano-structured tips is based on the vacuum deposition of metal film on a dielectric AFM probe by thermal evaporation or sputtering. A typical example of a silver tip produced by thermal evaporation is reported in Fig. 4.2(b). As it can be noted, this method produces a granular film around the tip whose structure depends on several experimental factors as the evaporation rate, the working temperature, the residual vapour pressure in the evaporation chamber and the distance between the thermal bowl and the tip. The sputtering technique, instead, offers a major control of these parameters but provides smoother tips with respect to the thermal evaporation.

Another method is to bind colloidal nano-objects (beads, cubes or wires) to commercial AFM tips [77]. Compared to the etching method, this approach allows a more well-defined and reproducible geometry. An exam-

ple is shown in the Fig. 4.2, where the tip is prepared by depositing silver nanocubes using the Langmuir-Blodgett (LB) method [124].

In recent works, the nano-fabrication technology has also spread out thanks to high reproducibility and the possibility to better control size and shape of the tip. The Fig. 4.2(d) and (e) show, respectively, a probe produced
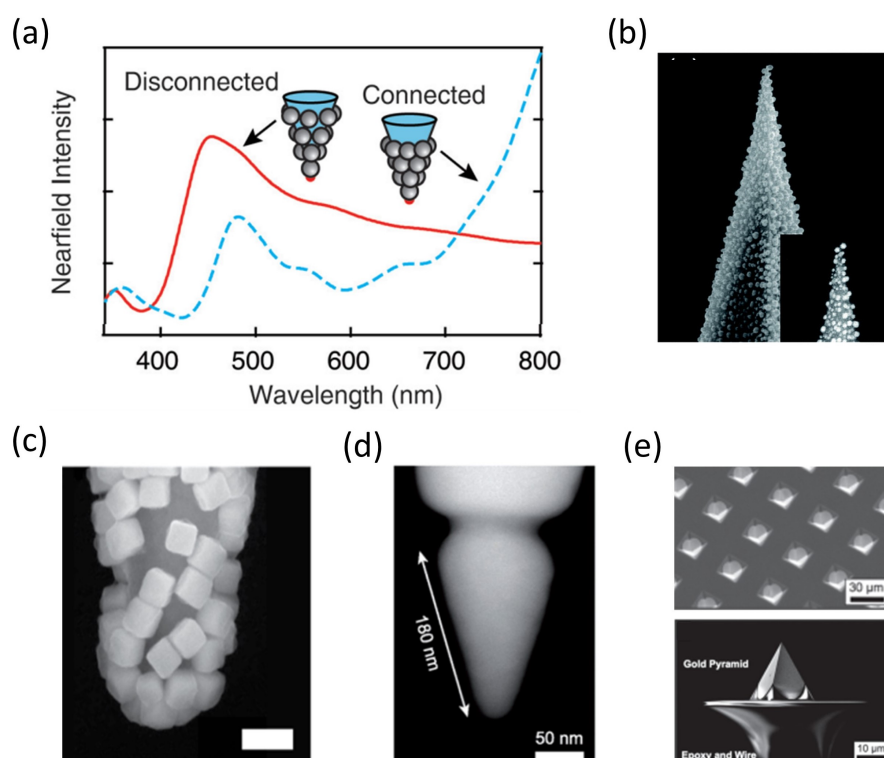

Figure 4.2: (a) Near-field intensity spectrum at the tip of disconnected (solid line) and connected (dashed line) 16-particle probe, normalized to that without tip [122]; (b) Silver tip produced by thermal evaporation [86]; (c) Commercial dielectric tip covered by NCs (scale bar 200 *nm*) [124]; (d) FIB image of a gold tip with a FIB milled groove; (e) Template-stripped gold pyramids [77].

by a focused ion-beam (FIM) milling and a series of gold pyramidal tips fabricated by using template stripping [77]. The use of such technologies allow a large-scale production but are quite expensive.

Beyond all these techniques, our group has developed a novel strategy based on the nano-structuring of *Ag*-sputtered commercial AFM probes via

Inductively Coupled Plasma (ICP) discharge. As far as we know, this is the first work in which this method is used to fabricate active-TERS probes. The plasma treatment produces a metallic nano-texture, resembling a *coral-like* structure, through a mechanism denoted as solid-state dewetting (SSD). The so-produced probes have shown an amplification up to 10^7 and a spatial resolution down to 10 *nm*, which render these devices particularly attractive for nanometer chemical characterization. A patent on this subject has been recently deposited by us and it is under evaluation.

4.2 Plasma-Induced Solid-State Dewetting

The solid-state dewetting (SSD) is a well-known phenomenon based on the agglomeration of thin films in nano-islands on solid substrates when heated to sufficiently high temperature. In some cases this mechanism is undesired and becomes a problem when the continuity and integrity of a thin film is required [125]. On the other hand, in the last years the application of the SSD to thin metal films has emerged as a novel simple and low-cost method for the fabrication of well-controlled patterns of particle arrays [126]. In fact the dewetting of a thin film can lead to the formation of spherical or faceted particles that are not easily produced via others methods as lithography-based techniques [127]. The SSD has been employed in various fields to produce nano-structures as catalysts, resistors, electrods and sensors [125] but a particular attention has been devoted to the development of plasmonic devices [128–130]. In fact, the optical resonances of nano-structures depend on the shape and ordering of the constituent nano-particles. Thus, by the appropriate control of the process parameters one can modify and eventually optimize the optical response.

The physical mechanism governing the SSD is the minimization of the the total surface energy of the free surfaces of the film and substrate, and of the film-substrate interface. A metallic layer deposited on a substrate by physical vapour deposition or sputtering is generally in a unstable or metastable state because of the relatively high energies of the metal

surface and film-substrate interface. This no-equilibrium condition leads the metal layer to break up and agglomerate (dewet) in nano-islands even at temperatures well below the metal's melting point [125].

Generally, two are the dewetting mechanisms of the thin films that can occur. If the film is metastable, it dewets by nucleation and expansion of dry zones. The nucleation can be initiated by edge retraction or void growth. If the film is unstable, it dewets spontaneously through the amplification of thickness perturbations and the mechanism is called spinodal dewetting. The Fig.4.3 illustrates the schematics and the SEM images of time evolution of the two processes. The surface morphology
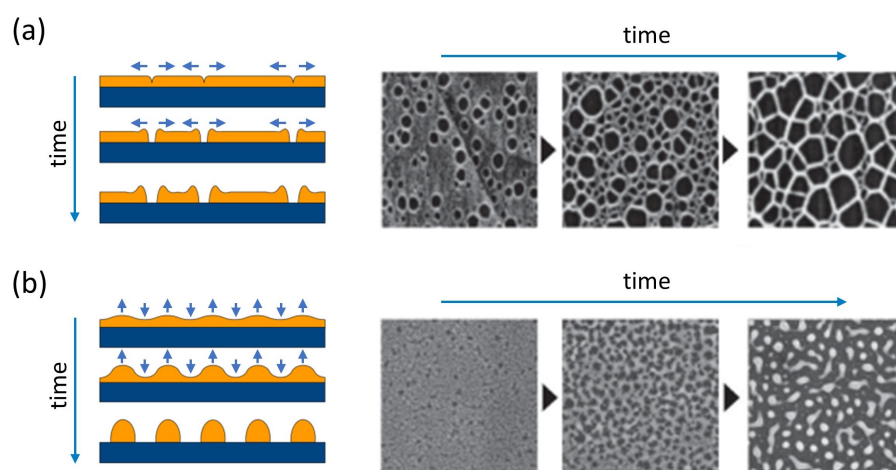

Figure 4.3: Schematic representation (left) and experimental example (right) of the time evolution of the phenomenon regarding (a) the nucleation and (b) the spinodal dewetting [127, 131].

evolves progressively through intermediate states until the formation of separate droplets/3D islands regardless of the type of mechanism. Notably, the nucleation of the holes occurs randomly within the film, whereas the nano-objects are spatially correlated in the spinodal dewetting. This is the key feature in general to distinguish the two processes. The dewetting mechanism can be reliably identified by analysing the spatial distribution of particles or holes using the power spectral density (PSD) function as it will be discussed later, or Minkowski functionals [127, 131].

The SSD is tipically induced by thermal annealing at temperatures well below the bulk melting point. Lkhamsuren *et al.* [132] proposed the thermal dewetting to produce structured *Au* coated AFM probes for TERS application. However, the employment of the thermal annealing requires high temperatures and does not assure a quite uniformity of the metal grains on the probe. Motivated by this, we propose as alternative the application of a RF inductively coupled plasma (ICP) to induce the dewetting process of thin *Ag* films. Compared to the thermal annealing, the plasma treatment is a low-temperature process allowing also the use of supporting heat-sensitive substrates. Furthermore, the surface modification can occur in shorter times. The plasma-based techniques are quite widespread for the nano-structuring of different materials and they differ each others for the excitation source, the gas process and the device geometry [133]. A systematic investigation of the effect of RF plasmas in different process gases on sputtered silver surfaces can be found in Okeil *et al.* [134]. The authors show that flat *Ag* films can be completely converted in a 3D-nanoporous surfaces when exposed to a oxidizing RF capacitively coupled plasma (CCP). The incorporation of oxygen into the silver lattice leads to a volume expansion and a change in film morphology. Anyway, no further explanation about the underlying mechanism in the forming of such structures is proposed. Moreover, they do not mention the possible contribution of the SSD.

To the best of our knowledge, the only report referring explicitly to the plasma-induced SSD available in literature was found in Choe *et al* [135]. The authors induce the dewetting of *Sn* films by applying a RF ICP in H_2 atmosphere. They suggested that the mechanism could be explained by considering the energy gradient in the film. During the plasma exposure, the surface of the film is bombarded by the accelerated ions present in the ionized gas which transfer energy to the film surface so that the surface atoms become energetically active compared to the bulk ones. If the film is thin, this difference in energy is small and thus when a sufficient plasma energy is applied, the film fluctuates as a whole causing the spinodal dewetting. For thicker films, this difference is larger and the surface atoms

diffuse and activate the dewetting process by means of hole nucleation and growth before sufficient plasma energy reaches the bulk.

In our case, we used a RF plasma in synthetic air atmosphere to induce the nano-structuring of thin *Ag* films where the role of the oxidation of the silver layer can not be excluded in the process. As a matter of fact, the mechanism is more complex and very debated in literature. Although it is not very well understood yet, an attempt to explain it could be done by considering the co-existence and co-operation of more phenomena:

(*i*) The air RF plasma is capable to oxide the silver layer at ambient temperature thanks to reactive species produced in the discharge. As will be shown in the experimental part of this chapter, the formation of the oxide silver layer have been further confirmed by X-rays diffraction (XRD) measurements. As reported and verified by El Mel *et al.* [136], the *Ag* layer exhibits a very poor oxidation resistance at low temperature in the presence of atomic oxygen. In contrast, when exposed to the molecular oxygen the oxidation process requires a high temperature to be induced. Furthermore, the oxidation process in the RF plasma have been found to contribute to the break-up of the silver surface. In fact, as the oxide layer grows, internal stresses due to mechanical or thermal excursions can induce the crack of the formed layer. As result, the pristine underlying silver exposed again to the air plasma repeats the process until the silver is completely oxidized [137]. Anyway, as experimentally observed by the same authors and by our group, this cracking-induced process is not sufficient to explain the growth of nano-structures on the silver surface.

(*ii*) Another mechanism proposed that enters in competition with the cracking-induced oxidation process described above is the Kirkendall effect [138]. The effect is a diffusional phenomenon that is observed to occur at the interface between two different materials. The different diffusion rates of the two constituents produce a disequilibrium of the material flow that is compensated by the inter-diffusion of vacancies. In some cases, the condensation of excess vacancies can give rise to

void formation, called Kirkendall voids, in proximity of the interface and within the faster diffusion side. When the Kirkendall effect occurs in the oxidation process of metals, the vacancy clusters are induced by the rapid outward diffusion of metal ions rather than inward oxygen ions through the oxide layers [139].

The role of this effect in the formation of nanoporous Ag oxide structures, similar to that obtained by our group, have been been reported in another work of El Mel *et al.* [140]. They have verified that by exposing different Ag nanocrystals to the RF room air ICP, a series of nanovoids form at Ag/Ag_xO interface. In addition, the effect occurs simultaneously with the cracking-induced oxidation process that tends to fragment the oxide shell into small discontinuous pieces. Depending on the shape and the dimension of the Ag nanocrystal, the corrosion process can take over the Kirkendall effect because it hinders the formation of a continuous oxide layer necessary to ensure the unbalanced mass transport of material. Nevertheless, the Kirkendall effect can not be activated unless the material is exposed to a high temperature. Since the plasma treatment occurs at ambient temperature, the authors suggest that the temperature could rise locally due to the exothermic nature of the chemical oxidation reaction of the silver. Another explanation could be that the energy carried by the oxygen atoms is converted into heat in the oxide layer [137]. In any case, the Kirkendall effect is considered responsable for the formation of nanovoids inside the nano-crystal and below the formed oxide layer. In fact, this effect is largely used to produce hollow structures as reported in several works [141–143]. The final morphology of the treated nanocrystals of El Mel's group, instead, shows a clear nanoporosity and elongated nanoparticles on the overall surface. So, the authors suggest that such structures could be due to the physical bombardment of the oxide shell by the relatively energetic species generated by the RF plasma.

(*iii*) Compared to the work of El Mel's group, we suggest that the forma-

tion of such structures should be triggered by the solid-state dewetting of the oxide silver layer. In fact both the local rise of the temperature and the stress strain due to the oxidation process could contribute to induce the mechanism. In order to minimize the energy of the system as the exposure time to the RF plasma increases, the structure of the oxide film rearranges to form grain boundaries along which atoms can easily migrate to form islands. As a matter of fact, a similar process is also reported in the work of Zhao *et al.* [144] where the Kirkendall voids have been proposed to explain the initial stage of thermally-induced SSD of *Cu* films deposited on native Si oxide substrates. Our assumption is that the cracking process and the Kirkendall effect might weaken and destabilize the thin oxide layer promoting the SSD of the silver oxide.

This phenomenological model would suggest the idea that SSD could occur through the nucleation of the Kirkendall voids or crack defects. Anyway, as we will see in the experimental part, the morphology of the silver layer is more similar to the classical picture of the spinodal dewetting. In fact, the nanostructures are spatially correlated and the morphology shows a long-range order with a characteristic wavelength.

4.2.1   Mechanism and phenomenology of the SSD

Most of the theory on solid state dewetting is borrowed from that on thermal dewetting in liquid/solid films, the systems where this phenomenon was first observed. From a thermodynamic point of the view, the dewetting of thin liquid film deposited on a solid substrate depends on the intermolecular interaction substrate-film and film-film. In particular, the driving force energy of the process can be defined as

$$E_S = \gamma_A + \gamma_{AB} - \gamma_B \tag{4.1}$$

where γ_i is the surface energy density of material ($i = A, B$; A film; B substrate) and γ_{AB} the interfacial energy density. If E_s is negative, i.e.

$\gamma_B > \gamma_A + \gamma_{AB}$, the film is stable and a total wetting is achieved, otherwise, the film dewets [126]. In the liquid state dewetting the process occurs by hydrodynamics mass transfer in the film. Compared to liquid case, the dominant transport mechanism of the SSD is generally found to be the capillary-driven surface diffusion. The diffusion is initiated from the spontaneous formation of voids or holes (dewetting zone) at specific defects or inhomogeneities (impurities, thickness variation and, in particulary, grain boundaries in polyctrystalline metal films) and proceeds via retraction of the edges of the film [145]. The Fig. 4.4(a) shows the lateral profile of an hole edge with a sharp corner indicated by a dashed line. In order to reduce the local curvature of the corner, the mass is transported from the triple line (the intersection point where the film, ambient, and substrate meet) to the flat area ahead of the edge via a flux J. The accumulation of the mass at the edge of the film leads to the development of a rim, and the flux divergence ahead of the rim causes the formation of a valley. The rim height increases as the edge continues to retract giving rise to the retraction edge phenomenon [126]. The transport of the material A from the dewetting zone to the film surface via the flux J for a isotropic material is given by the Fick's law [146]:

$$J = -B\nabla_s\kappa \quad \text{with} \quad B = \frac{D_s\gamma_A\Omega^2 n}{k_BT} \tag{4.2}$$

where ∇_s is the surface gradient of the film curvature κ, Ω is the atomic volume and n is the areal number density of atoms. The time evolution of the film thickness $h(t)$ can be obtained following the theory of the thermal grooving by Mullins [147]. Mullins stated that the velocity of the surface element along its normal is proportional to the gradient of the flux J and thus to the surface Laplacian of κ:

$$\frac{dh(t)}{dt} = \nabla_sJ = -B\nabla_s^2\kappa \tag{4.3}$$

The evolution of the film surface profile can be obtained by solving the Eq. 4.3 considering four boundary conditions: (i) the shape of the surface

profile (contact line), (ii) the initial thickness of the film, (iii) the mass conservation and (iv) the equilibrium Young angle given by $\cos(\theta_{eq}) = \frac{\gamma_B - \gamma_{AB}}{\gamma_A} = 1 - \frac{E_S}{\gamma_A}$ [146].
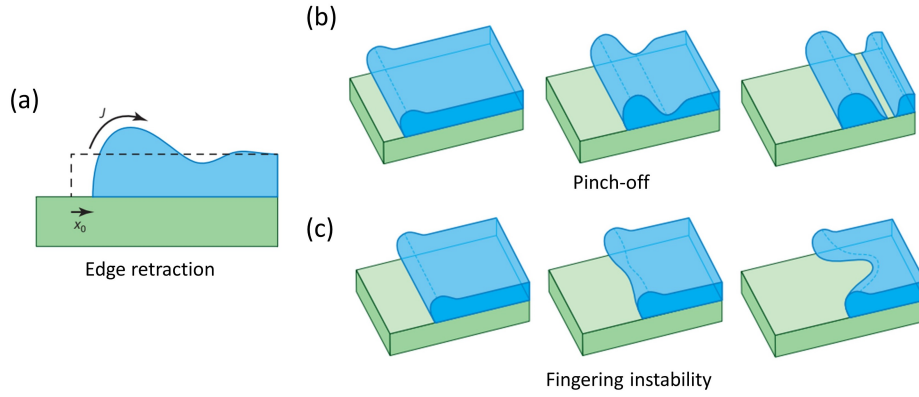

Figure 4.4: (a) Cross-sectional view of a retracting edge of a film, after retraction over a distance x_0 from the position of the initial edge with a sharp corner; Schematics of the edge retraction followed by (a) rim pinch-off and (b) fingering instability [126].

The solution of the Eq. 4.3 found by Srolovitz and Safran [148] shows that as the rim recedes, a depletion arises immediately behind due to the oscillation of the film thickness. As the edge retracts, the valley becomes deeper leading to pinch-off of the rim. The new edge then continues to retract and develop a new rim, and the process repeats (Fig. 4.4(b)).

In some cases, when the dewetting zones are sparse, the forming rims may break up into fingers (fingers instability) (Fig. 4.4(c)). It has been also observed that a further amplification of thickness fluctuations (Rayleigh-like instability) can eventually contribute to fragment the forming rims or fingers in isolated nano-islands. As matter of fact, the final stages of the dewetting can be affected by different breaking instabilities (fingering instabilities, pinch-off and mass shedding, Rayleigh instabilities) that give rise to more complex morphologies (fractal, dentritic, etc.). Anyway, according to various models, during the dewetting, the edge of the film should retract as $x_0 \propto t^n$ where n depends on the type of the retracting edge. Before pinch-off or development of a fingering instability, models

suggest that $n \sim 0.4$ to 0.5, whereas for repeated pinch-off an average value of $n = 1$ [126]. In general, the crystallographic and faceting properties of the film material can influence the shape evolution of the rim [146].

Spinodal dewetting

Up to now the SSD has been described as a process that occurs in proximity of holes or defects through the mechanism of the edge retraction of the thin solid film. It is worth noting that the thin film can also undergo a continuous process where the dewetting is initiated by spontaneous growing of the perturbations in the film thickness. Since the final morphologies of the film remember those observed in phase separation of a binary mixture via spinodal decomposition [149], this process is commonly termed spinodal dewetting [150]. The Fig. 4.5(a) illustrates an example of early stage morphology of spinodal decomposition observed in a colloid-polymer system. The spinodal dewetting has been observed in various liquid films of polymers [151, 152], liquid crystals [153, 154] and metals [155–157]. In par-
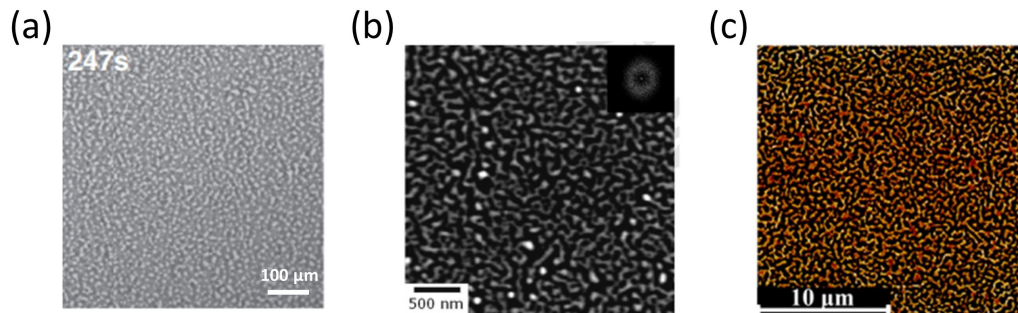

Figure 4.5: (a) Confocal Scanning Laser Microscopy (CSLM) image of the spinodal decomposition for a colloid-polymer mixture [158]; (b) SEM morphology after irradiation by 10 laser pulses on the $Co/Ag/SiO_2$ bilayer with 1.5 nm of Co and 5 nm Ag thickness [159]; (c) SEM image of thermically-induced spinodal dewetting on a film Pd/SiN with 10 nm of Pd thickness [160].

ticular in the metals, it is generally induced by localized irradiation with nanosecond laser pulses, whereby the metal film is heated to its melting point. An example of laser pulsed-induced spinodal dewetting is shown in

Fig. 4.5(b). In fact, these studies assert that the transition to a liquid phase at high temperatures is a necessary condition to induce spinodal dewetting of the metallic thin films. However, few works have demonstrated that the spinodal dewetting can also be initiated at temperatures below the melting point giving rise to a spinodal "solid-state" dewetting [160, 161] (see Fig. 4.5(c)). This is the case of the plasma-induced dewetting [135] where the spinodal-like pattern was also experimentally observed in this work thesis on *Ag* thin films. Even if the mechanism is not completely clarified, based on the phenomenological model proposed beforehand, the cracking process and the Kirkendall effect might contribute to destabilize the oxide silver layer. At middle stage of RF plasma, the unstable oxide film might dewet spontaneously through the amplification of the thickness perturbations. The main characteristic of the observed spinodal-like morphology is that the holes or the forming nanostructures are spatially correlated.

In literature, it is well known that in spinodal regime the pattern of the nano-structured film has a well-defined spatial frequency. Formally, the characteristic wavelength of the spinodal instability can be obtained using the linear stability analysis considering the profile of the film-vacuum interface that minimizes the system free energy [162, 163]. The total free energy of a defect-free thin film on a substrate can be defined as [160]:

$$F(t) = \int \left[\gamma \sqrt{1 + (\nabla h(\vec{\chi}, t))^2} + G(h(\vec{\chi}, t)) \right] dx\, dy \qquad (4.4)$$

where $h(\vec{\chi}, t)$ is the film profile above the point $\vec{\chi} = (x, y)$ on the substrate, γ is the surface tension film-vacuum, G is the interfacial potential that represents the energy density per unit area required to bring two interfaces (film-substrate and film-vacuum) from infinity to a certain distance h. Let's apply the linear stability theory by introducing a perturbation $u(\vec{\chi}, t)$ on the film profile so that $h = h_0 + u$. By substituting h in Eq. 4.4 and expanding up to the second order, the free energy becomes:

$$F(t) = \frac{1}{2} \int \left[\gamma (\nabla u)^2 + G''(h_0) u^2 \right] dx\, dy \qquad (4.5)$$

The free energy can be rewritten as a sum over independent fluctuation modes by expressing u as Fourier series $u(\vec{\chi}, t) = \sum_{\vec{k}} u_{\vec{\chi}(t)} e^{i\vec{\chi}\cdot\vec{k}}$:

$$F(t) = \pi \sum_{\vec{k}} \left[\gamma k^2 + G''(h_0) \right] |u_{\vec{k}}(t)|^2 = \sum_{\vec{k}} F_{\vec{k}}(t) \tag{4.6}$$

The film rupture via spinodal dewetting occurs if at the spontaneous growth of the surface oscillations ($d|u_{\vec{k}}(t)|^2/dt > 0$) corresponds a simultaneous reduction of the free energy of its associate mode ($dF(t)/dt < 0$). Such conditions are fulfilled if the first term $\gamma k^2 + G''(h_0)$ of the Eq. 4.6 is negative, i.e. if $G''(h_0)$ is negative and k is not too large considering that γk^2 is always positive. As result, both stable (decaying) and unstable (growing) modes will be present. Given the previous inequality and defining $\lambda = 2\pi/k$, the unstable modes that contribute to break up the film are characterized by wavelengths longer than the cut-off wavelength λ_c:

$$\lambda > 2\pi \sqrt{\frac{-\gamma}{G''(h_0)}} = \lambda_c \tag{4.7}$$

The interfacial potential G depends on the intermolecular forces of the system under consideration. In thin films the potential can be described by a short-range term (Born repulsive forces) proportional to h^{-8} and a van der Waals (vdW) term proportional to h^{-2}:

$$G(h) = \frac{A}{2h^2} - \frac{Ah_c^6}{24h^8} \tag{4.8}$$

where A is the Hamaker constant. By inserting this expression in Eq. 4.7, λ_c can be approximated to:

$$\lambda_c \approx 2\pi \left(-\frac{\gamma}{3A} \right)^{1/2} h_0^2 \tag{4.9}$$

This linear scaling between λ_c and h_0^2 is generally observed in the experiments and used as a qualitative criterion to determine if the spinodal regime occurs [160]. Quantitative predictions, however, requires prescrib-

ing the exact form of the interface potential G. Given the right shape of
the interfacial potential, the spinodal dewetting morphology could show
both bi-continuous structures and holes depending on the thickness of the
film [164]. In particular, it has been observed that the dewetting pattern in
some metal films show bicontinuous structures for thinner films, whereas
a distribution of holes for thicker ones [156, 163]. This behaviour can be
explained considering that in thinner films the vdW forces are dominant
respect to the surface tensions because of the nearness of the film-substrate
and film-vacuum interfaces. Whereas the surface tensions tend to smooth
the film-vacuum interface, the vdW tend to change the thickness to min-
imize the surface free energy, thus inducing an amplification of thickness
modulation [162].

4.2.2   Power Spectral Density (PSD) method

Beyond the qualitative considerations, the best way to distinguish between
the nucleation and spinodal dewetting is often done by measuring the av-
erage hole wavelength. As discussed above, the presence of spatial corre-
lations is a signature of spinodal regime; their absence is often indicative of
nucleation-driven dewetting although the origin of the nucleated holes is
not very clear [165]. In this work thesis, the SEM dewetting-induced pat-
tern images have been analysed by using the power spectral density (PSD)
function. This approach, based on the decomposition of the surface into
contributions from different spatial frequencies is a consolidated method
used to analyse the surface structuring induced by dewetting [166]. It can
be computed by using the fast Fourier transform [151, 156, 157], the height-
height correlation function [167] or the autocorrelation function [168]. In
fact, formally, the PSD is defined as the Fourier transform of the autocorre-
lation function $R(\mathbf{r}, t)$ which measures the correlation of the surface heights,
$h(\mathbf{r}, t)$, separated by the vector $\mathbf{r}$:

$$P(\mathbf{k}, t) = \frac{\omega^2}{(2\pi)^d} \int R(\mathbf{r}, t) e^{i\mathbf{k}\cdot\mathbf{r}} d\mathbf{r} \qquad (4.10)$$

where $R(\mathbf{r}, t) = \omega^{-2}\langle h(\mathbf{x}, t)h(\mathbf{x} + \mathbf{r}, t)\rangle$, ω is the interface width and d the dimensionality. The PSD can be expressed also as function of the height-height correlation function:

$$P(\mathbf{k}, t) = \frac{1}{2(2\pi)^d} \int [2\omega^2 - H(\mathbf{r}, t)]e^{i\mathbf{k}\cdot\mathbf{r}}d\mathbf{r} \tag{4.11}$$

where $H(\mathbf{r}, t) = \langle(h(\mathbf{x} + \mathbf{r}, t) - h(\mathbf{x}, t))^2\rangle$. The Fig. 4.6 illustrates the parameters used to describe the surfaces statistics where the lateral correlation length l_{cor} is defined as the value of $\mathbf{r}$ at which $R(\mathbf{r}, t)$ decreases to $1/e$ of its original value [169].
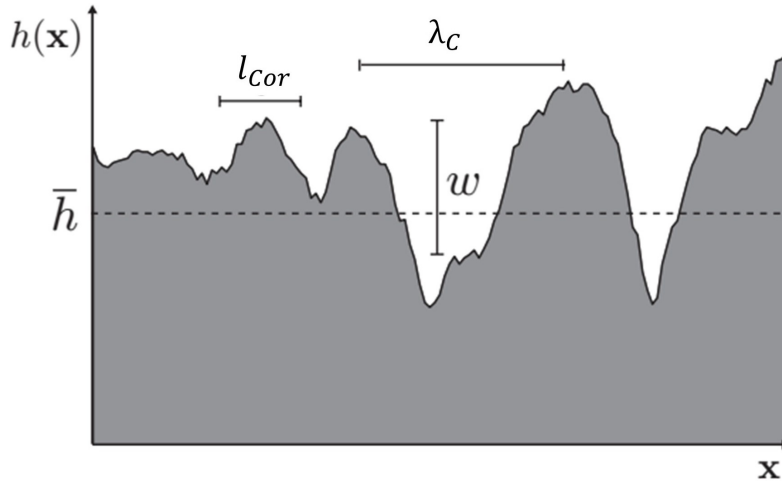

Figure 4.6: Illustration of statistics used to describe rough surfaces: the mean height $\bar{h}$, interface width w, lateral correlation length l_{cor}, and wavelength λ_C [169].

Nevertheless, the application of FFT algorithm for the estimation of power spectra is more popular. The method is based on the fact that the energy contained in an analog signal, $u(t)$, is related to the magnitude of the squared signal integrated over time (we will consider for now the discussion in time domain):

$$E = \int_{-\infty}^{\infty} |u(t)|^2 dt \tag{4.12}$$

where $u(t)$ is a Fourier transformable function. According to the Parseval's theorem, the Fourier transform (FT) of the function $U(v) = \int_{-\infty}^{\infty} u(t)e^{i2\pi vt}dt$ preserves the energy:

$$\int_{-\infty}^{\infty} |u(t)|^2 dt = \int_{-\infty}^{\infty} |U(v)|^2 dv \tag{4.13}$$

where $|U(v)|^2$ equals the energy density function over frequency v, also referred to as the energy spectral density [170]. If the function $u(t)$ is not Fourier transformable[1], it can be truncated as:

$$u_T(t) = \begin{cases} u(t) & -\frac{T}{2} < t < \frac{T}{2} \\ 0 & \text{otherwise} \end{cases} \tag{4.16}$$

The normalized energy spectrum of the truncated function $u_T(t)$ is:

$$G_T(v) = \frac{|U_T(v)|^2}{T} \tag{4.17}$$

which has units of power per unit frequency and T is the interval in signal time. We can now define the power spectral density of $u(t)$ as:

$$PSD(v) = G_T(v) = \lim_{T \to +\infty} \frac{|U(v)|^2}{T} \tag{4.18}$$

The continuous Fourier transform for a finite sequence of data is equivalent

---

[1]A function $u(t)$ is Fourier transformable if

$$\int_{-\infty}^{\infty} |u(t)| dt < \infty \tag{4.14}$$

On the contrary, the function satisfies

$$lim_{T \to +\infty} \frac{1}{T} \int_{-T/2}^{T/2} u^2(t) dt < \infty \tag{4.15}$$

and it is said $u(t)$ has finite average power. In the former case, we will refer to the distribution of energy over the frequency or energy spectrum density (energy spectrum). In the latter case, we talk about the average power over the frequency or power spectral density (power spectrum) [171].

to the discrete Fourier transform (DFT) defined as:

$$U(v) = \sum_{n=0}^{N-1} u(t_n) e^{i\frac{2\pi}{N}vt_n} \Delta t \tag{4.19}$$

where N is the number of sample points in t and u (both variables take on values from 0 to $N-1$); the DFT is usually evaluated using a fast Fourier transformation (FFT) algorithm. Taking into account the DFT, the discrete version of a one-dimensional PS and PSD are given by:

$$PS(v) = \frac{|U_T(v)|^2}{N^2} \quad PSD(v) = \frac{PS(v)}{\Delta v} \tag{4.20}$$

where the PSD has units of amplitude squared per frequency unit and Δv is the data point spacing in frequency space. This discussion can be applied to the case of the optical surface by using the 2D FFT. Given a surface image characterized by a matrix of $N_x \times N_y$ values of pixel intensity $u(x, y)$, the PSD is given by:

$$PSD(v_x, v_y) = \frac{1}{N_x^2 N_y^2} \frac{|U(v_x, v_y)|^2}{\Delta v_x \Delta v_y} \tag{4.21}$$

where $U(v_x, v_y)$ is the 2D FFT of the image [172]. The calculated PSD function shows the strength of the variations (intensity of the pixels) as a function of frequency. For isotropic surfaces this function is radially symmetric and only the radial average of the PSD in polar coordinate system is typically shown [173, 174]. The Fig. 4.7 shows an example of PSD and average radial PSD calculation for a nano-structured substrate prepared in this work thesis. The annular shape of the power spectrum, indicates the existence of a characteristic length-scale, whereas the radial symmetry denotes the isotropy of the dewetted pattern. From the frequency v_C corresponding to a peak in the radial average PSD, is possible to calculate the characteristic wavelength $\lambda_C = 1/v_C$. The peak is a clear mark of which is the dominant characteristic length scale of the surface. In addition, the full width at half maximum (*FWHM*) is inversely proportional to the lateral correlation length l_{cor} defined as the length beyond which the surface
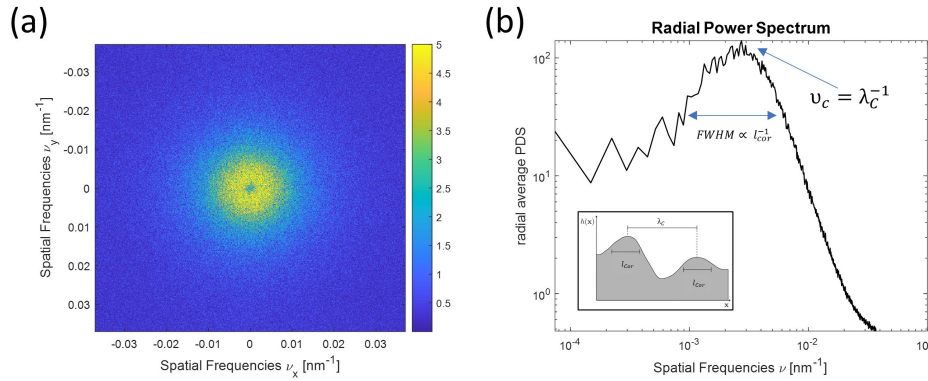
Figure 4.7: (a) Power spectral density of a periodic nano-structured sample; (b) Corresponding average radial PSD. The inset shows the surface parameters used to describe the surface.

heights were not significantly correlated. These parameters must satisfy the relation $l_{cor} \leq \lambda$ because the grains on the surface are separated by at least their size; only if they grow next to each other would it imply that $l_{cor} = \lambda$ [169]. More details on the estimation of these surface parameters from the SEM images are reported in Sec. 3.6.

4.3 Fabrication of the TERS probes

In the following sections it will be described the procedure used for the fabrication of the TERS-probes employed in this thesis work. The tips were prepared starting from two types of commercially available *Si* AFM tips: ArrowTM CONT (NanoWorld) [175] for Contact Mode operation and TESPA (Bruker) [176] for AC Mode imaging, having radii of curvature of about 10 *nm* and 7 *nm*, respectively. The procedure is based on three steps as sketched in Fig. 4.8. Briefly, the *Si* AFM probe is firstly oxidized and then covered with a metallic layer of silver. Finally, the *Ag* layer undergoes the plasma treatment that leads to the formation of a *coral-like* structure on the tip shaft. These different stages are extensively described below.
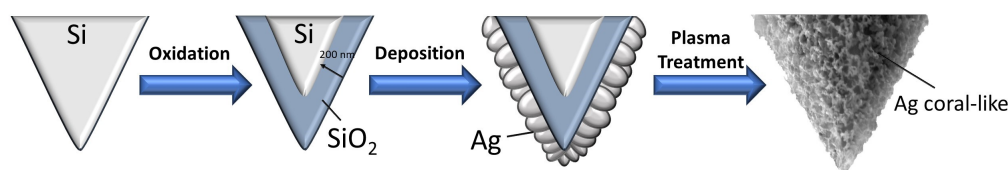
Figure 4.8: Schematics of the procedure designed to fabricate *Ag coral-like* probes.

4.3.1 Oxidation

The first step consists of the modification of the refractive index of the probe base material which is made of silicon. It has been proven that the plasmon resonance of *Ag*-coated *Si* probe is strongly dependent on the refractive index of the under-layer material [177]. In particular, the decreasing of the refractive index from *Si* (n = 4.4) to SiO_2 (n = 1.5) has shown to improve the yield and TERS enhancement factor as well as to tune the plasmon resonance in the visible region (Fig. 4.9(a)). Therefore, the *Si* AFM tips
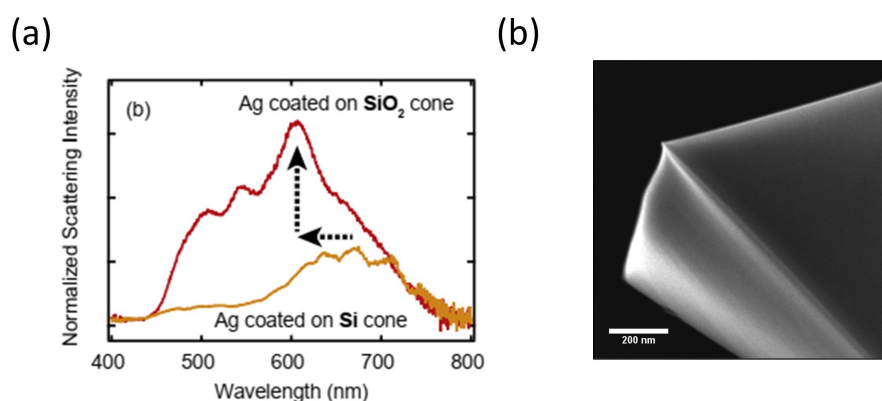

Figure 4.9: (a) Dark-field scattering spectra of *Ag*-coated oxidized *Si* probe and *Ag*-coated non-oxidized *Si* probe [109]; (b) SEM image of an Arrow Si AFM probe after the thermal treatment at 1000°C for 10 *h*. The tip radius is still around 10 *nm*.

were oxidized by heating them in a muffle furnace at 1000°C for 10 *h* in order to produce a thick layer of SiO_2 (more than ≈ 200 *nm*). Unlike the deposition of SiO_2, the thermal oxidation allows preserving the sharpness

of the tip [71]. The Fig. 4.9(b) shows the SEM image of an oxidized probe where any appreciable increment in the tip radius is visible (radius $\approx$ 10 *nm*). After that, the tips are left in the furnace for $\approx$ 24 *h* to slowly cool down to room temperature.

4.3.2 Deposition

Before the deposition of the metallic layer, the tips are pre-cleaned to remove any organic contaminants attached on the tip surface during the oxidation phase. The impurities could affect the metallic adhesion to the tip shaft and compromise the nano-structuring of the *Ag* layer. Thus, the probes are firstly exposed to the Argon plasma cleaner (Sec. 3.2) for few minutes at the pressure of 1 *Torr*. After that, the tip is covered with 30 *nm* of silver via magnetron sputtering (Sec. 3.1) by using a sputtering current I_S at 50 *mA* and the stage rotation *ST* at 35 *rpm*. The choice of this thickness represents a compromise both to preserve the sharpness of the tip apex and to allow the formation of the nano-texture. As will be described in next section, the thickness is one of the process parameter controlled for the optimization of the procedure.

In order to improve the adhesion of the *Ag* layer on the tip, the probe is previously coated with 3 *nm* of chromium (I_S = 120 *mA*, *ST* = 35 *rpm*) followed by 10 *nm* of gold (I_S = 20 *mA*, *ST* = 35 *rpm*). The multi-layer *Cr-Au-Ag* have been proven to be highly stable and capable to sustain TERS measurements in both air and liquid environments [178]. In fact, it has been observed experimentally that the absence of this bilayer can compromise the nano-structuring of the silver layer. After the exposition to the plasma treatment, a series of bubbles start to arise on the surface probe as shown in the Fig. 4.10(a) proving the necessity to stabilize the silver layer adhesion. The Fig. 4.10(b) shows a tip (not treated yet) after the deposition of the double *Cr-Au* layer and 30 *nm* of *Ag*. After this deposition, the tip radius increases up to about 50 *nm* due to the coating of the multi-layer. Moreover, the sputtering provides a tip with a surface quite uniform. This type of tip, which in the following will be referred as

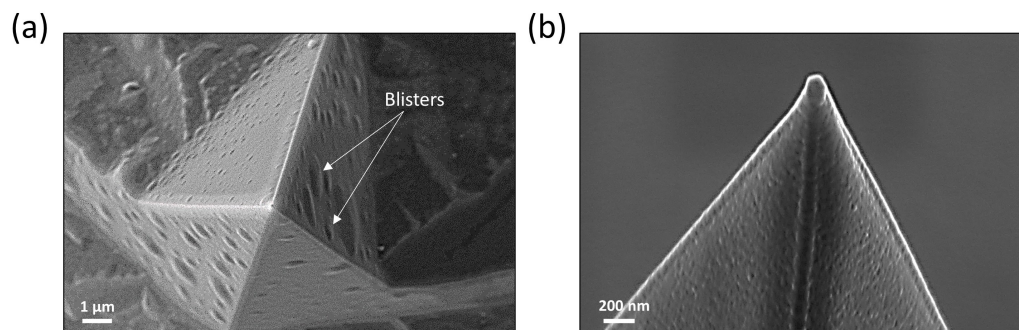*s-type* (smooth type), is mainly useful in the gap-mode configuration.

(a) (b)

Figure 4.10: (a) SEM image of a TESP tip covered with only 40 *nm* of *Ag* layer and exposed to Air plasma discharge for 30 *s*. (b) SEM image of a TESP tip covered with the multi-layer *Cr* (3 *nm*), *Au* (10 *nm*), *Ag* (30 *nm*) via magnetron sputtering.

4.3.3   Plasma treatment

The ICP treatment was performed with the same system used to remove the organic contaminant on the tip after thermal treatment, but using as gas process synthetic air (79% N_2 + 21% O_2 mixture). The optimal exposure time (and the ideal deposition thickness of *Ag*) has been found after a previous test conducted on oxidized *Si* wafers. In this way the plasma effect of an *Ag* layer deposited on the same base material of the tips can be verified. As will be shown in the following and described in Sec. 4.2, the exposition to RF-excited air plasma induces the formation of well-separated silver oxide grains thanks to the presence of reactive oxygen species produced in the discharge. Anyway, since the *Ag*-oxide layer can compromise the plasmonic performances of the probes [179, 180], the metallic layer is restored by a further plasma treatment in Argon atmosphere. The reliability of this procedure is confirmed by monitoring the samples with the X-rays diffraction (XRD) technique.

Preliminary test on Si wafers

The preparatory study is carried out on oxidized silicon wafers covered with the double *Cr-Au* layer and a variable *Ag* thickness h_0 ranging from 5 *nm* to 60 *nm*. At this stage, the *Ag*-sputtered film appears quite smooth and compact, with only slight roughness resulting from the sputtering process. The samples are then exposed the RF plasma in air atmosphere at pressure
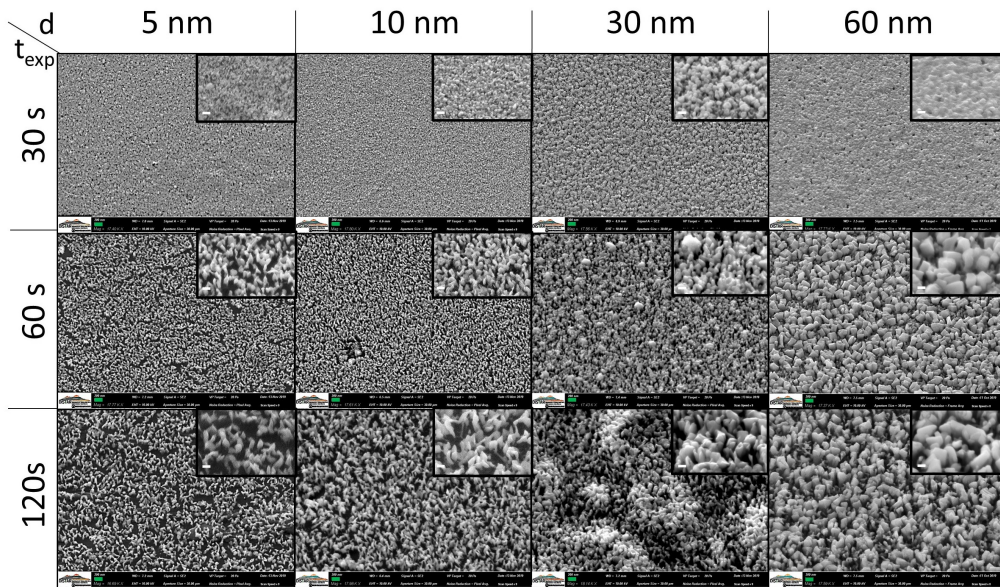

Figure 4.11: SEM images of the oxidized *Si* wafers covered by different *Ag* layer thickness and treated at various exposure time t_{exp} to the RF air-plasma (scale bar 200 *nm*). The magnification of the SEM images are shown in the inset (scale bar is 100 *nm*). All the substrates are pre-covered with the double *Cr-Au* layer.

of 1 *Torr* and power of 18 *W* by varying the exposure time t_{exp} in the range 30 *s*-120 *s*. The Fig. 4.11 shows a group of the most significant SEM images of some treated substrates. As can be seen, a uniform nano-structuring of the *Ag* surface all over the substrate starts to arise as the exposure time to the air RF plasma increases. The *Ag*-film texture evolves to complex and disconnected *Ag*-oxide grains which resembles the classical picture of the spinodal dewetting. The spinodal-like pattern can be confirmed by analysing the SEM images of the substrates through the PSD approach

described in the Sec. 4.2.2. The analysis have shown that the most of morphologies show a long-range order with a characteristic wavelength λ_c. The Fig. 4.12(a) reports the values λ_c at each initial Ag thickness h_0 for the intermediated stage ($t_{exp} = 1\ m$). Although previous studies on spinodal dewetting have reported that the dominant wavelength usually varies with the second power of the film thickness, in our case the complexity and the interaction of different effects (Kirkendall effect, cracking-induced oxidation process) make difficult to predict a theoretical trend. A specific modeling not available now should be required to take into account the complex system. Anyway, the fact that the patterns have a specific long-range order might inspire confidence that the SSD have been triggered by the spinodal process. The forming Ag-oxide nano-objects have differ-
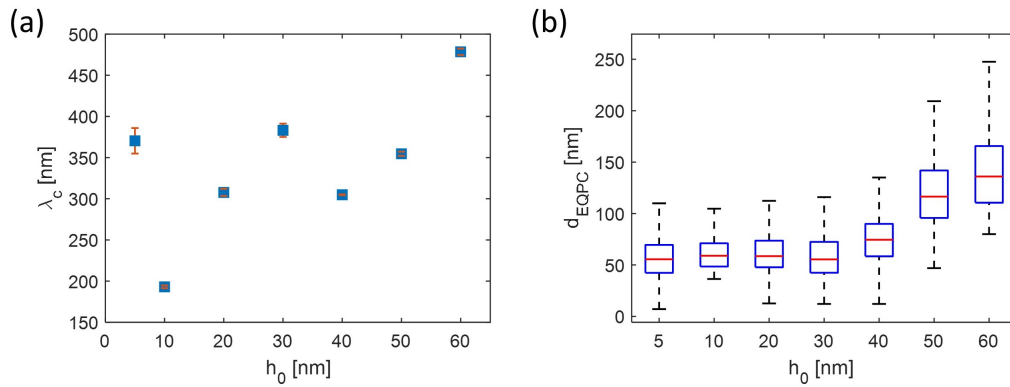

Figure 4.12: (a) Plot of the characteristic wavelength λ_c as function of the squared Ag layer thickness h_0^2 at fixed exposure time of 1 m; (b) Box plot of the d_{EQPC} as function of the Ag layer thickness at fixed exposure time of 1 m.

ent average size and shape depending on both the process parameters: the thickness and the exposure time. Notably, thinner layers give rise to smaller and lamellar objects with a morphology referred to as *coral-like*, whereas large thickness provides larger and faceted shape objects which are typical of the solid-state dewetting [127]. This transition to a major average size of the grains can be observed quantitatively in the Fig. 4.12(b) where the boxplot of the diameter d_{EQPC} is plotted as function of the initial thickness for the fixed exposure time of 1 m. As described in Sec. 3.6, the

equivalent projected circle *EQPC* diameter, i.e. the diameter of a circle of equal area to the 2*D* projection of a particle, distribution can be obtained by SEM images analysis and is, generally, used as parameter to estimate the no-spherical particle size. At thickness below 30 *nm*, the size of grains seems to not change dramatically. Whereas at values above 30 *nm*, we observe a slow increase of the dimensions.

A further quantitative analysis of the SEM images reveals that, fixed the *Ag* layer thickness, the increasing exposure time seems to promotes the enlargement of the nano-pores between the grains. A similar trend has been observed also in the work of Mel *et al.* [136] in the nano-structuring of silver columns by means of the room air RF ICP. They verified that a further increase in the oxidation rate leads to an increase of the global porosity of the *Ag*-oxide surface. In this regard, the Tab. 4.1 reports our

Table 4.1: Porosity [%]

Exposure time [s]	Thickness [nm]		
	5	30	60
30	45	47	8
60	48	55	44
120	57	57	54

values of the porosity (percentage of pores with respect the total substrate) calculated as described in Sec. 3.6 at different thickness. As we can see, these values tend to increase in the function of the exposure time. Since the pores are precursor of the final separation in isolated nano-structures, these outcomes prove that the exposure time can be tuned in order to obtain more or less separated grains.

Coral-like AFM tips

Once confirmed the effectiveness of the plasma treatment in nano-structuring the *Ag* surface, the freshly metallized tips with the multilayer *Cr-Au-Ag* are exposed to the air RF plasma. The Fig. 4.13(a-c) shows a series of images of
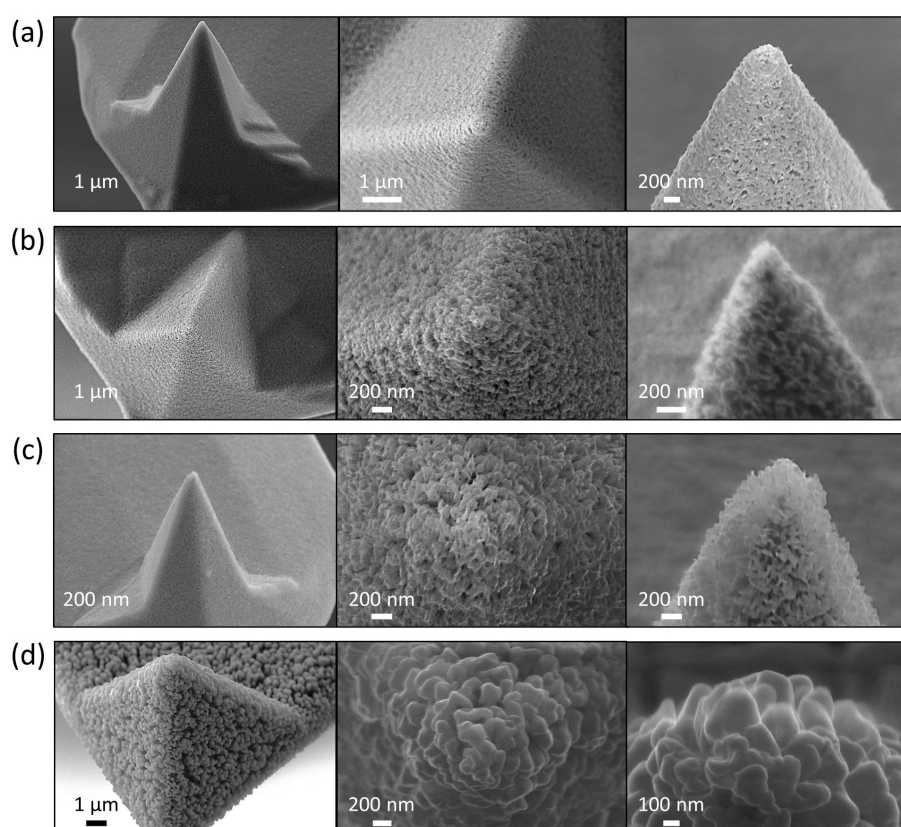
Figure 4.13: SEM images of the treated TESPA tips covered with *Ag* 30 *nm* and exposed to Air plasma for (a) 30 *s*, (b) 60 *s* and (c) 90 *s*; (d) Arrow tip covered by *Ag* 60 *nm* and exposed to air plasma for 60 *s*. All the tips are pre-covered with the double *Cr-Au* layer.

the tips covered by the *Ag* layer of 30 *nm* and treated in air-plasma for 30 *s*, 60 *s* and 90 *s*, respectively. The morphologies obtained on the tip probe are not so dissimilar to that obtained on the oxidized *Si* wafers covered by the same thickness of *Ag* layer. Slight differences in the dimension and shape of the formed grains are probably due to conical shape of the tip that can affect the forming morphology. Nevertheless, the *coral-like* morphology is induced on tip when treated for at least 60 *s*. The thickness of 30 *nm* of *Ag* represents the best choice to preserve the sharpness of the tip. As matter of fact, a deposition *Ag* layer of 60 *nm* gives rise to grains of dimensions too large that can compromise the spatial resolution of TERS measurements (Fig. 4.13(d)). To better visualize and analyse the spinodal-like pattern induced on the tip draft, the SEM images have also been acquired in corrispondence of the AFM-cantilever flat region which is in proximity to the apical part of the treated tip. The time evolution of obtained morphologies is illustrated in the Fig. 4.14. For each stage, the main surface parameters
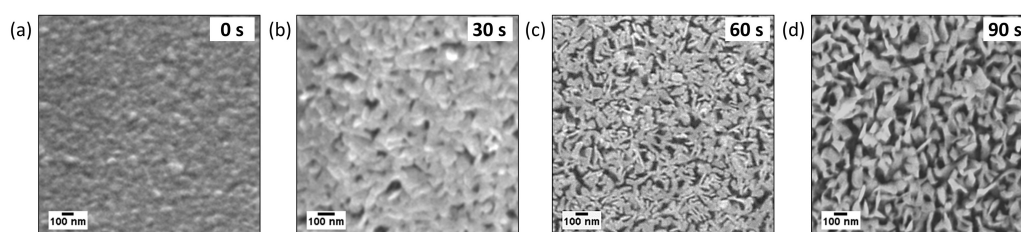

Figure 4.14: SEM images of the *Ag*-sputtered film following 0 *s* (not-treated film), 30 *s*, 60 *s* and 90 *s*, respectively.

have been calculated as described in the Sec. 3.6 and summarized in the Table 4.2.

As it is possible to see the presence of a characteristic length for all the time values highlights the role of spinodal-dewetting in the nanostructuring process. In addition, the time exposure of 90 *s* contributes to further separate the *coral-like* structures (porosity 48 %). This arrangement is similar to that described by Taguchi *et al.* [122] by which well separated metal grains distributed on a AFM probes produce higher and much consistent enhancement in TERS experiments. For this reason, this exposure

Table 4.2: Statistical surface parameters

Exposure time [s]	$\lambda_c = 1/\nu_c$ [nm]*	d_{EQPC} [nm]**	Porosity [%]
60	142 ± 3	48 (38, 59)	38
90	171 ± 3	56 (12, 71)	48

*ν_c is the peak value of the radial average PSD evaluated from the Lorentzian fit;
**Median (lower quartile, upper quartile).

time is arguably the best parameter to obtain TERS-active *coral-like* probes.

Silver oxide reduction

After the air-plasma treatment, the probes are exposed to the *Ar*-plasma in order to reduce the formed oxide silver nano-structures. The presence of the *Ag*-oxide has been demonstrated by performing XRD measurements on the oxidized *Si* wafers rather than directly on TERS tips. This choice to use larger and flat substrates was prompted to facilitate the XRD measurements. In addition, the wafers have been covered with only a 30 *nm* of *Ag* film to eliminate the strong interference from XRD signals due to gold in the adhesion layer, which exhibits diffraction peaks overlapping that from silver [181]. The Fig. 4.15(a) shows the XRD pattern in the 2θ region $30° - 48°$ obtained by analyzing the freshly sputtered *Ag* film. The two sharp peaks at 38.2° and 44.3° correspond to the (111) and (200) planes of the face centered cubic structure of *Ag* nanostructures, respectively. The XRD pattern after air-plasma treatment in Fig. 4.15(b) shows the presence of new reflections at 2θ angles of 32.08°, 32.68° and 37.11°, corresponding to overlapping contributions from *AgO* and Ag_2O [182]. The oxidation of the substrate is accompanied by a color change from silver color to grey-dark brown, as shown in the insets of Fig. 4.15. However, the *Ar* plasma treatment completely eliminates this dark color, restoring a silver color. Clearly, due to silver nano-structuring, the initial mirror-like appearance is lost. The Fig. 4.15(c) shows the XRD pattern acquired after 30 *s* of *Ar*-plasma treatment. The absence of the reflections from the oxidized silver
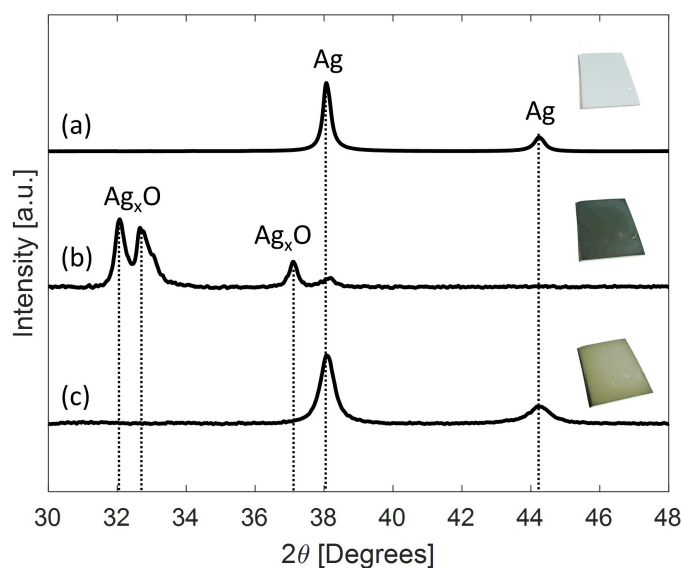
Figure 4.15: Comparison of XRD patterns in the 2θ $30° - 48°$ region relative to silicon wafers: (a) freshly sputtered with a silver layer, (b) after the treatment to air-plasma and (c) after the reducing treatment with *Ar*-plasma. The insets in each panel report a picture of the analysed wafers.

species confirms the effectiveness of the reduction process. Therefore, the oxidized tips have been treated for the same time in the *Ar* discharge (RF discharge power: 18 *W*). In the following, the tip resulting from this treatment will be referred to as *r-type* (rough type). Compared to the chemical approaches used to reduce the oxide metals [179], the plasma treatment in Argon atmosphere results cleaner (reagents-free) and faster. In contrast with Okeil *et al.* [134], we have verified that the nano-structures do not undergo any morphological modification. In fact, the authors observe the formation of a series of pores on the overall *Ag* surface when treated to Argon plasma for 30 *m*. In our case, the reduced exposure time to the discharge of 30 *s* is sufficient to reduce the oxide layer and allows to avoid such porosity. As shown in the Fig. 4.16(b) the oxidized tip after the reduction process has preserved the initial *coral-like* structures produced on the tip surface (Fig. 4.16(a)).
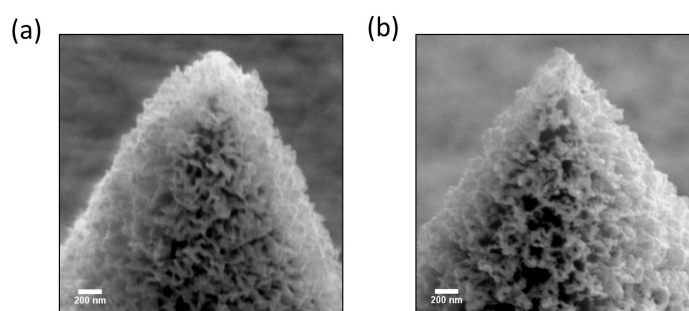
Figure 4.16: TESPA tip covered with the double layer *Cr-Au* and 30 *nm* of *Ag* (a) exposed to the air-plasma for 90 *s* (b) and after the reduction process.

4.4 Characterization of the TERS probes

The performances of both the *r-type* and *s-type* probes have been evaluated through the estimation of the enhancement factor and the spatial resolution. The TERS measurements were performed using the combined AFM/Raman microscope described in more detail in Sec. 3.3.

4.4.1 Enhancement Factor

The enhancement factor (EF) of the *r-type* tip has been estimated by using cristal violet (CV, Merck) dye as probe molecule. CV samples were prepared by dropping 10 *μl* of 10 *μM* CV solution on the glass coverslip. As matter of fact, the evaporation of the droplet on a substrate usually leaves a characteristic ring-like deposition due to particle migration to the contact lines, referred as coffee-ring effect [183]. To avoid this effect and to uniformly distribute the molecules onto the glass substrate, the droplet is covered with another cleaned coverslip forming a sandwich-like cell and allowed to dry at room temperature. In this way it is possible to improve the uniformity of molecule distribution on the surface. Under these conditions, the molecular density on each coverslip is estimated to be around 0.26 molecules per nm^2 (assuming an even distribution of molecules on the two sandwiched coverslips). The EF is then calculated following the Eq. 2.22 by comparing the near- and far-field intensities of a specific Raman

band under investigation and taking into account the source areas. The signals are acquired by mounting the prepared tip on the AFM system, as described in the Par. 3.3.2, and operating in the AC mode. The Fig. 4.17(a) shows the Raman spectra acquired on the CV sample (i) when the tip is approached to the substrate (near-field signal I_{NF}) and (ii) when the tip is is retracted by at least $10\mu m$ from the sample (far-field signal I_{NF}). The former spectrum exhibits the peaks that can be assigned to the CV [184]. The main bands used to evaluate the EF are highlighted in the spectrum. In the latter case, the spectrum is characterized by a broad fluorescence
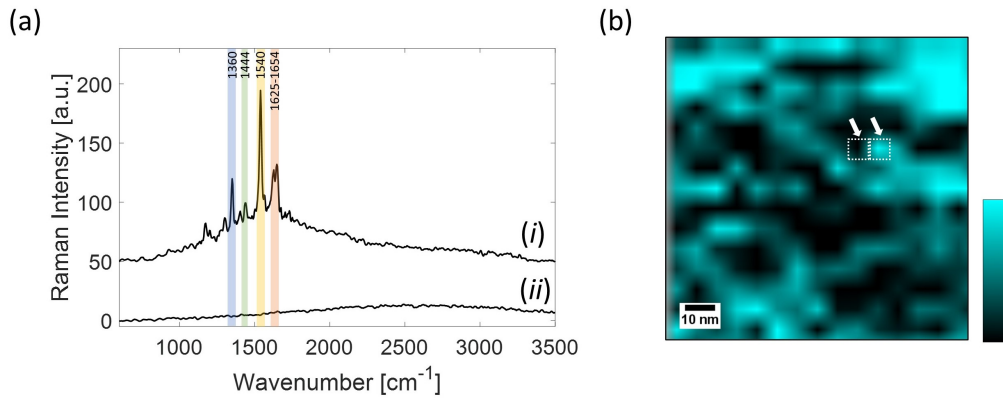
(a)   (b)

Figure 4.17: (a) Comparison between (i) the near-field CV Raman spectrum acquired using a power $P_{NF} = 80\ \mu W$ and time integration $\tau_{NF} = 3\ s$ and (ii) the far-field CV Raman spectrum acquired using a power $P_{FF} = 10\ mW$ and time integration $\tau_{FF} = 20\ s$. The assignment of selected CV bands (highlighted by colored vertical bars) is also shown; (b) Near-field signal map of the CV band $1540\ cm^{-1}$ acquired in a $0.1 \times 0.1\ \mu m^2$ region with a 10 nm step, $P = 80\ \mu W$ and $\tau = 3\ s$.

background and no CV signals are detectable. So, the estimation of the far field Raman signal is achieved by increasing the laser power P and the integration time τ. In this way, the optical contrast C is calculated as:

$$C = \frac{I_{NF}}{I_{FF}} \frac{P_{FF}}{P_{NF}} \frac{\tau_{FF}}{\tau_{NF}} \qquad (4.22)$$

where $P_{FF} = 10\ mW$, $\tau_{FF} = 20s$, $P_{NF} = 80\ \mu W$ and $\tau_{NF} = 3s$. The both near- and far-field peak intensities are found by averaging the signals

values coming from a Raman-band intensity map acquired in the $1 \times 1 \ \mu m^2$ area. This mean is performed to avoid any wrong evaluation of the EF due to an inhomogeneous distribution of CV molecules on the coverslip at the nanometer scale. According to Eq. 2.22, given the contrast C, the enhancement factor can be finally estimated considering that the source areas are calculated by assuming $r_{FF} = 350 \ nm$ for the laser beam waist in the focal region, and $r_{NF} = 10 \ nm$ for the radius of the near field region.

Actually, the sensitivity and near-field spatial resolution can be evaluated analysing the TERS signal of a sub-monolayer distribution of CV on the glass coverslip that is achieved by using the concentration of $1 \ \mu M$ than $10 \ \mu M$. The Fig. 4.17(b) shows the near-field intensity map of the CV band at $1540 \ cm^{-1}$ acquired in $0.1 \times 0.1 \ \mu m^2$ region with a $10 \ nm$ step. As it is possible to see, TERS signals acquired on adjacent points occasionally reveal significant fluctuations (see, for instance, the two pixel highlighted by arrows), which suggest a spatial resolution for the tip close to the scan step ($10 \ nm$). This behaviour also proves the high sensitivity of the TERS probes in detecting only a few molecules considering that at this low concentration in the region corresponding to a single pixel of the map should be present $\approx 3 \ molecules$ ($2.6 \times 10^{-2} \ molecules$ per nm^2).

Reproducibility

The average *EF* value was calculated by testing 22 *r-type* tips freshly prepared. Among them, only the 91% has exhibited a TERS activity showing an average $EF = (4.3 \pm 3.2) \times 10^7$. The EF distribution coming from the TERS-active tips is shown in Fig. 4.18. Considering that the best values found in literature [122, 185], this outcome can be considered a good result.

Aging effect

Although the *Ag* tips can provide the highest enhancement factor respect with other noble metals, it is well known that are susceptible to oxidation and enhancement decay within a few days when not stored in inert atmo-
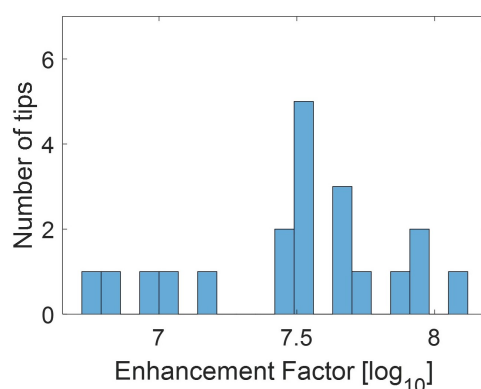
Figure 4.18: Histogram showing the logarithmic values of EFs of the tested *r-type* probes.

sphere [84, 86, 121]. As a matter of fact, a lost in TERS activity has been verified in 5 *r-type* tips that were exposed to ambient air for one week. Anyway, a treatment in *Ar*-plasma for 10 *s* have turned out to be effective in the regeneration of the TERS activity, even if with a reduced EF (average EF value $\approx 10^6$). Moreover, the *Ar*-plasma is also effective in cleaning tips from organic contaminants typically collected on the tip during the TERS measurements, which results in a serious drawback for the analysis of biological systems.

4.4.2 TERS imaging

An accurate estimation of the spatial resolution of the TERS tip, anyway, requires analyzing the TERS signal across a small sample feature. For this purpose, we have used a sample of multi-walled carbon nanotubes (MWCNTs) deposited on a glass coverlip. The MWCNTs (purity > 98%, *Sigma-Aldrich*) have a variable length ranging from 2.5 to 10 *μm* and average wall thickness of 12 *μm*. The sample is prepared by washing the MWCNTs in sequence in Milli-Q water, isopropanol and acetone. After each washing step, the relative dispersion was dried by heating on a hotplate at 100°*C*. Then, CNTs were suspended in $1, 2 -$ dichloroethane at a concentration of 1 *mg/ml* and then sonicated at 20% amplitude by a 1/8″ probe sonicator

(*FB*505 Fisher Scientific) for 60 *m* with a cycle ON of 20 *s* followed by a cycle OFF of 10 *s*. To avoid the probe heating, the sample is kept in a ice bath throughout the treatment. Successively, the suspension was centrifuged at 6000 *rpm* for 70 *s*, and the supernatant was collected. This, later, was finally drop-cast on the glass coverslip for the analysis. The
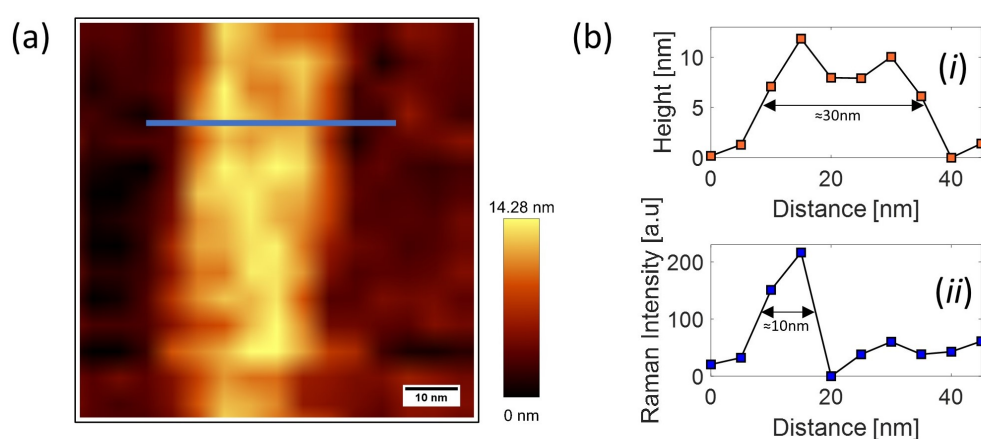

Figure 4.19: (a) AFM topography of a single MWCNT obtained by scanning a 75 × 75 *nm* region, with a 5 *nm* step; (b) Comparison between the AFM height (i) and TERS signal of the G-band of CNT spectrum (ii) obtained across the CNT section highlighted by a blue line in the AFM map reported in part (a). The points correspond to the AFM-height/TERS values averaged on 3 scans of the same line.

Fig. 4.19(a) shows the AFM topographical image of a single MWCNT. The cross-section indicated by the blue line and plotted in trace (i) of the Fig. 4.19(b), reveals a FWHM $\approx$ 30 *nm* that is much higher than the expected CNT diameter provided by the manufacturer. This enlargement is clearly due to the convolution effect of the real CNT width with the probe apex. On the other hand, the simultaneously acquired TERS intensity of the G-band ($\sim$ 1580 cm^{-1}) across the same line reveals a FWHM $\approx$ 10 *nm*, a value confirmed by repeated scans of the same line (Fig. 4.19(b)(ii)). This value provides an upper limit of the TERS resolution for the employed tip and is in line with typical spatial resolution estimated by AFM-TERS [84, 122]. It should be noted that the lateral spatial resolution could be affected by the

coral-like structure present on the tip surface because of the Tip-Broadening Effect (TBE) reported by Wang *et al.* [186]. Compared to smooth tips where the hot-spot is located at the apex of the tip, in a nano-structured tip the hot spots are located on the nano-features distributed both on the apex and the shaft region. This shaft region, that interacts laterally with the sample object, may contribute to enhance the TERS signal making the lateral dimension of the objects larger than they are in reality. This phenomenon is quite similar to that occurring in AFM imaging when the tip radius is much larger than the sample nanofeatures.

The spatial resolution and the high sensitivity of the *r-type* probes have been also tested on 2D MoS_2 nanoflakes samples. The Raman spectrum of nanoflakes is characterized by two main peaks, the in-plane E^1_{2g} mode at $\sim$ 382 cm^{-1} and out-of-plane A_{1g} mode at $\sim$ 405.2 cm^{-1} (spectrum 1 in Fig. 4.20(b)). The Fig. 4.20(a) shows a TERS map of a flake corresponding to the line at 405.2 cm^{-1}. The distribution well reproduced the shape of the flake at nanoscale level. From the frequency difference between the observed A_{1g} and E^1_{2g} is possible to estimate the thickness of the nanoflake. In this case, a difference of 23.2 cm^{-1} was measured corresponding to few atomic layers [187].
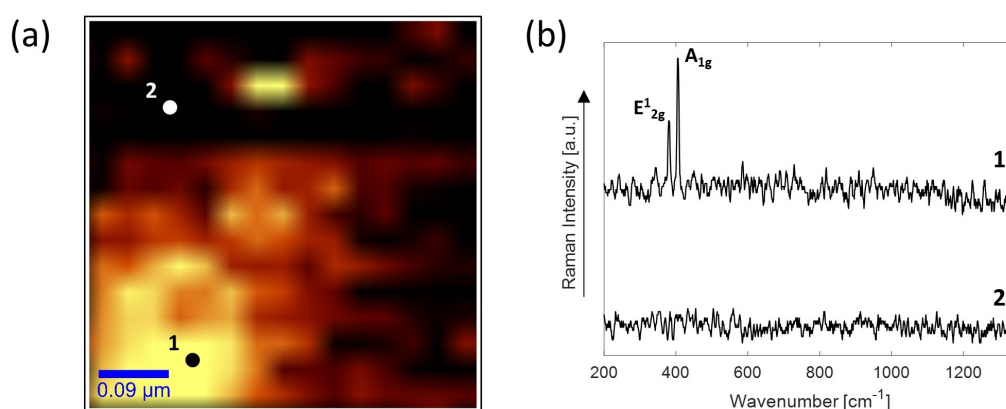

Figure 4.20: (a) TERS map of a flake obtained plotting the A_{1g} band (pixel size $\sim$ 30 nm, P = 10 μW); (c) TERS spectra acquired in the two points indicated in the TERS map.

4.4.3 Gap-mode configuration

As the final step, 5 *s-type* tips have been tested in order to highlight the role of nano-structuring. In the normal TERS configuration, the tips does not show any TERS activity so they have been tested in the gap-mode configuration. In this case the 10 μM CV solution is deposited on a 10 *nm* gold-coated coverslip following the same procedure described previously. The low thickness of gold film let the substrate to be transparent allowing the TERS gap-mode in back-scattering geometry. In this analysis, only 2 over 5 tips resulted to be TERS-active, with an average $EF \approx 2 \times 10^5$. As discussed in Par. 2.3.1, the gap contributes to enhance the Raman signal thanks the strong localized electric field generated between the metallic tip and metallic substrate. The spatial resolution in gap-mode configuration depends on the effective tip radius. However, the tip radius does not seems to affect the TERS spatial resolution, which reasonably depends instead on the extent of the plasmon active gap region. The Fig. 4.21 shows both the
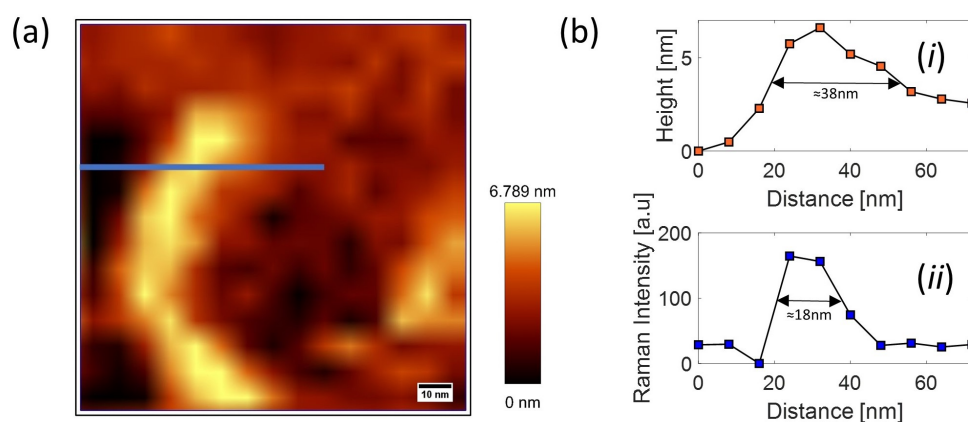

Figure 4.21: (a) AFM height map of a single MWCNT in a 120×120 *nm* region (step of 8 *nm*), obtained by using an *s-type* tip in gap-TERS configuration; (b) AFM height (i) and TERS signal of the G-band (ii) obtained across the CNT section highlighted by a blue line in the AFM map reported in part (a). The points correspond to AFM-height/TERS values averaged on 3 scans of the same line.

AFM map of a MWCNT deposited on a gold-coated glass coverslip (part (a)), together with both the AFM height and TERS signal of the G-band

acquired across a CNT section (part (b)). The FWHM of the TERS map provides an upper limit for a resolution of 18 *nm*. Instead, the CNT section can be estimated to be ~ 38 *nm* if evaluated from the AFM map, which is comparable to the tip radius (of the order of 40 *nm*).

Chapter 5

Fabrication and characterization of Coral-like SERS substrates

This chapter demonstrates that the procedure described in the Ch. 4 for the fabrication of the *coral-like* TERS probes, can be successfully used also to fabricate SERS active substrates. The results shown in this chapter are incorporated in a paper still in preparation.

5.1 Introduction

Since the discovery of the SERS, there have been many ongoing efforts to engineer SERS substrates producing strong, uniform and reproducible signals. As a matter of fact, the main obstacle in producing SERS substrates is consistency in fabrication and repeatability in measurements due to the inhomogeneity and randomness of SERS active hotspots. As seen in Sec. 2.2.3, the hotspots play a central role in creating high local EM field amplifications and can be classified depending the type of nanostructure that generate them.

The first generation of hotspots are produced by single nanoparticles (NPs) freely suspended in a homogeneous medium. Metal nanoparticles are used in a variety of research field as sensors, biological imaging, single molecule spectroscopy and clinical applications [188, 189]. They are, gener-

ally, synthesized by chemical procedures with different shapes that include not only the spheres but also cubes [190], prisms [191] or nanorods [192]. In addition, more complex morphologies can be produced to increase the hotspots density and the EF of the nanoparticles. Such strategies consist in the modification of the pre-synthesized nanoparticles by adding material [193] or by subtracting atoms on the metallic surface [194]. In this way is possible to improve the SERS performance at single-particle level preserving the intrinsic crystallinity of the starting nanoparticles [195]. The Fig. 5.1(a) shows an example of additive approach where *Au* nanodots have been selectively deposited over the edges and tips of *Ag* octahedra [196]. In the Fig. 5.1(b), instead, is shown a case of subtractive post-synthetic modification where a *Ag* nanowire is etched increasing the roughness on the surface [197]. Chemical-based NPs colloids production is a very pop-
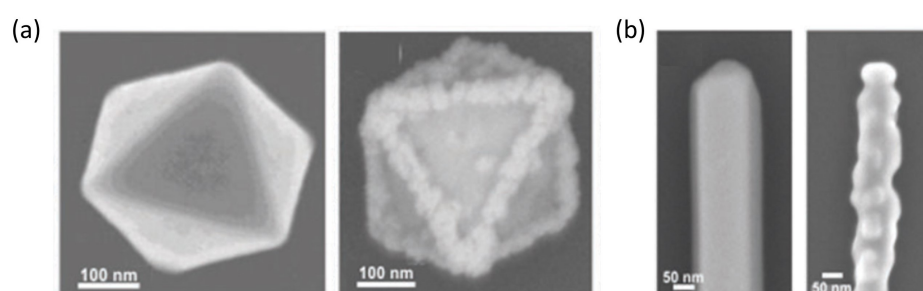

Figure 5.1: (a) SEM images of as-synthesized *Ag* octahedron and selective edge *Au*-deposited *Ag* octahedra, respectively; (b) SEM images of as-synthesized *Ag* nanowires and etched *Ag* nanowires, respectively [195].

ular low cost technique for SERS activities and particularly suitable for in solution experiments. However, the EF is normally weak ranging from 10^3 to 10^5 for these SERS samples. The sensitivity and the enhancement factor (EF) can be noticeably increased by exploiting the plasmonic coupling of neighbouring nano-particles (second generation of hotspots). The techniques used to produce ordered arrays of nanoparticles can be grouped in bottom-up and top-down approaches.

The bottom-up methods involve the fabrication of hierarchical structures starting from small building units such as atoms, nanoparticles, poly-

mers and nanoparticles. Generally, the nanoparticles can be aggregated by chemical or physical forces between NPs or between the NPs and substrate. When the assembly is chemically driven, the linking molecules or macromolecules often possess specific functional groups such as thiols, amino- and/or carboxylic acids [198]. In this regard, Ch. 6 will be focused on the development of SERS substrates prepared by our group via self-assembling of block copolymers. Another diffuse approach is based on the use of DNA origami templates that allows to reach inter-particle distances of few nanometers [199, 200]. The physically driven assemblies, instead, are based on magnetic and electrostatic interactions. The aggregation is induced by external stimuli as pressure, ionic strength, temperature or electromagnetic fields [198]. Another method consists in the optical manipulation of NPs to forms aggregates in liquid [201, 202]. Generally, the deposition of the NPs on a substrate can occur via drop-casting (Fig. 5.1(a)) or through Langmuir-Blodgett (LB) approach (Fig. 5.2(b)). Although the
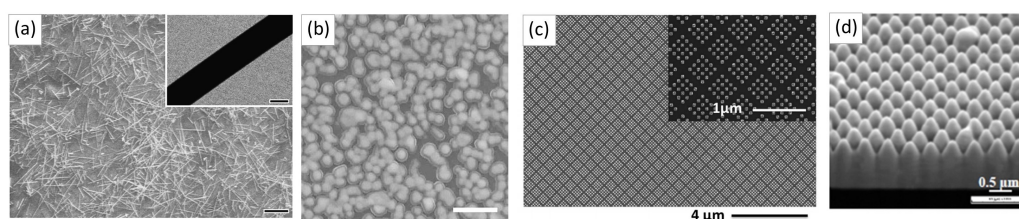

Figure 5.2: SEM images of SERS substrates. (a) *Ag* nanowires deposited on a glass substrate (scale bar 10 μm). The inset shows a singular nanowire of diameter 90 nm (scale bar 50 nm) [203]; (b) *Au* nanoparticles LB film (scale bar 500 nm) [204]; (c) *Au* nanocuboid periodic SERS substrates fabricated via EBL [205]; (d) *Au/Ag* multilayered NR arrays prepared via FIB [206].

bottom up techniques are low cost and allows a mass production on a large scale, the main obstacle is represented by the insufficient reproducibility. In addition, the residues from the synthesis process and molecules introduced during the assembly process could interfere with the SERS detection.

In comparison to the bottom-up approaches, the top-down methods involve the direct fabrication of small features on large area supports by various litographic techniques, such as elecron or ion beam lithography (EBL

and IBL), photolithography and nanoimprint lithography. The Fig. 5.2(c) illustrates a SERS device consisting of a series of metallic cuboids endowed with a specific inter-particle distance produced via EBL. Whereas the Fig. 5.2(d) shows an example of application of focused ion beam (FIB) employed to fabricate well ordered *Au/Ag* multilayered nanorods (NRs) arrays. These fabrication techniques allow very precise control over hotspot locations and structural geometries on a substrate, achieving strong and spatially defined electromagnetic field distributions. On the other hand, it is time-consuming and costly to prepare a large-area SERS substrate through these approaches. In addition, it is difficult to obtain a feature spacing below 10 *nm* even if this limitation has been overcome in the last years by performing sequential deposition of a metal and a spacer [198].

Beyond the strategies above mentioned, the plasma induced-dewetting technique, just used for the fabrication of TERS probes as described in Ch. 4, has proven to be effective to produce SERS substrates. In addition, the optical characterization of the so-prepared devices has shown a broadband response across the full visible and near-IR wavelength range. It is worth remembering that the plasmonic proprieties of the SERS substrates are strictly connected to the material, environment, shape, size and spacing of the nano-features. Most of the SERS substrates are, generally, characterized by a strong narrow LSPR resonance peaked at a given frequency. Therefore, the substrates have to be designed in order to fit the excitation wavelength, which requires more time and bio/chemical materials consuming depending on the used fabrication method. A broadband optical response of the SERS substrate, instead, represents a more flexible analytical tool. Furthermore, the plasmonic response in the near-IR range adds a significant advantage for biological applications of SERS.

5.2 Preparation of coral-like SERS substrate

The preparation of the nanostructured substrates mainly follows the same steps used to prepare the TERS probes. Since the substrates are prepared

using glass supports, the ossidation step is not applied in this case. Glass coverslips 15×15 mm^2 are firstly cleaned in *Ar*-plasma and then coated with the double bilayer of 3 *nm Cr*/10 *nm Au* and the *Ag* layer. After that, the samples are exposed to the RF air-plasma at the pressure of 0.4 *Torr* to induce the nano-structuring of the *Ag* film. In particular, the *coral-like* morphology has been observed for exposure times ranging from 90 *s* to 180 *s*. In fact, at higher exposure times the deposition layer starts to be completely "exfoliated" from the glass support and the nano-structuring is lost. As discussed in the previous chapter, the reactive oxygen species present in the feeding gas play a key role in the morphological modification of the *Ag* surface. At same time, the air-plasma forms a thin oxide layer as revealed by the XRD analysis in Sec.4.3.3. In order to get a deeper insight on this matter, the as-prepared glass substrates have been analysed by Raman spectroscopy. The Fig. 5.3(a) reports the Raman spectrum obtained by using a Raman probe power $P = 70$ μW and an integration interval $\tau = 100$ *s*. The observed Raman peaks at frequencies 214, 224, 296, 375, 423, 463 and

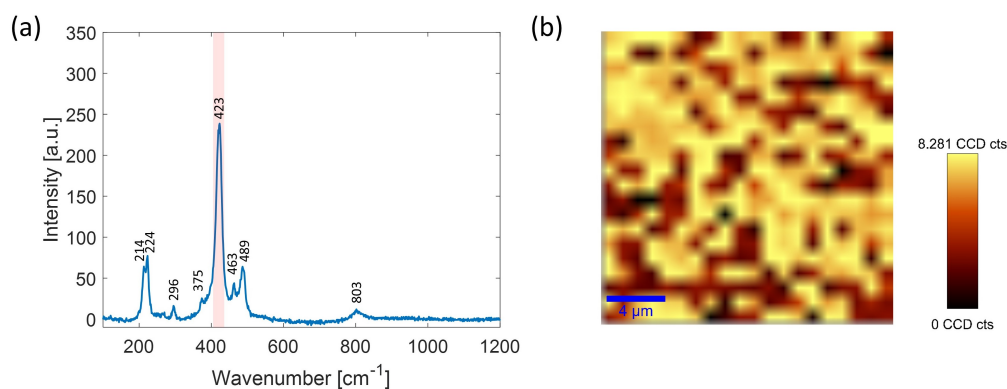Figure 5.3: (a) Raman spectrum of a substrate covered by 3 *nm Cr*/10 *nm Au*/30 *nm Ag* layer and treated in air-plasma for 90 *s*; (b) Raman imaging corresponding to the area intensity of the peak at 423 cm^{-1} (highlighted in part (a)) of the spectra acquired in a region of 20×20 μm^2 with a step of 1 μm using a power of 0.5 *mW* and integration time of 2 *s*.

489 cm^{-1} can be ascribed to *AgO*, while there is no spectroscopic evidence of AgO_2, usually appearing as a broad feature at $\sim$ 530 cm^{-1} [182, 207]. Roughly, *AgO* is uniformly distributed on the substrate, as evident from

the map in Fig.5.3(b) reporting the intensity of the AgO feature at 423 cm^{-1}.

As it is well known, silver oxides are rather sensitive to photochemical reduction and re-oxidation. As a consequence, prolonged exposition to relatively high laser power leads to a chemical change of surface structure that can be monitored by Raman spectroscopy. In particular, at laser power of ~ 17 mW, we observed a sudden spectra evolution in which AgO features disappear and the broad Ag_2O band at ~ 530 cm^{-1} band arises (see Fig. 5.4(a)). At the same time, two new bands appear, at ~ 803 cm^{-1} and 630 cm^{-1}. According to literature [208], both bands appear following the thermal decomposition of silver oxide to bulk silver. In particular, the band at 803 cm^{-1} is due to an atomic oxygen species (referred to as O_γ) chemisorbed on the reconstructed silver surface. Although O_γ species are confined to the surface, the intensity of this band is relatively high, as a consequence of SERS effect associated with surface roughness. On the contrary, the band at 630 cm^{-1} is due to oxygen species chemisorbed below the Ag surface, as a consequence of oxygen species diffusion underneath the Ag surface. Such chemisorbed species are referred to as O_β species.
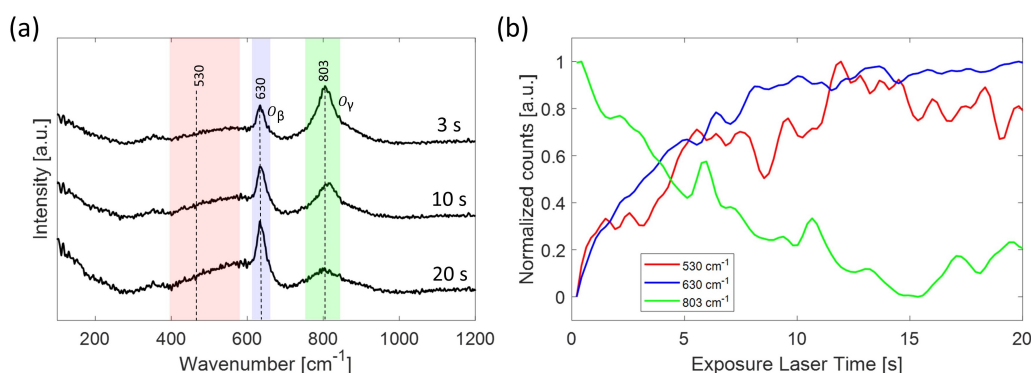

Figure 5.4: (a) Raman spectra recorded on the oxidized substrate during the laser irradiation and extracted at three different times; (b) Time evolution of Raman bands highlighted in part (a) corresponding to Ag_2O band at ~ 530 cm^{-1} (red), to O_β peak at 630 cm^{-1} and to O_γ peak at 630 cm^{-1}.

In Fig. 5.4(b) we report the evolution of these bands for the substrate undergoing a continuous irradiation of the Raman laser excitation set at a 17 mW power. As it is possible to note, the band due to O_β species

increases, reaching a plateau after $\sim 12\ s$ of continuous laser irradiation. At the same time, the band corresponding to O_γ species decreases, reaching a plateau on the same time scale. Reasonably, after 12 s, an equilibrium is reached among O_γ and O_β species. Clearly, the decrease of O_γ band can be also partly ascribed to the loss of SERS activity of the reconstructed metallic silver surface, as consequence of the continuous diffusion of oxygen species below the surface.

The final step of the preparation of the SERS substrates consists in the exposure to Argon plasma that, as verified in the Sec. 4.3.3, is effective to reduce the *Ag*-oxide with no modification of the nano-structuring. Also in this case, the surface evolution was investigated by Raman analysis. In particular, the same substrate was analysed as function of the exposure time to the *Ar* plasma. For such measurements, the laser power was limited to 0.3 mW, in order to avoid photo-induced effects. Fig. 5.5 reports the behaviour of the *AgO* band intensity at 423 cm^{-1} as function of the total exposure time to the *Ar*-plasma. Notably, after 10 s, the *AgO* band is no
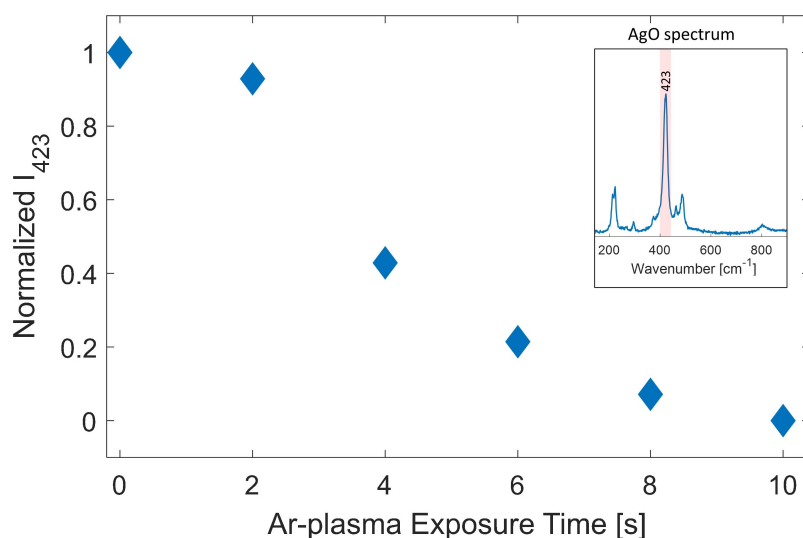

Figure 5.5: Temporal evolution of the *AgO* peak at 423 cm^{-1} (highlighted in the inset) at different exposure times to the *Ar*-plasma.

more visible, indicating a substantial decrease of *AgO* layer. Of course, due to the limited sensitivity of spontaneous Raman analysis, this cannot

be intended as a complete reduction of AgO to metallic Ag. As a matter of facts, the best performances (from the plasmonic point of view) of our substrates were observed after an exposure time $\tau = 30\ s$, that therefore was chosen for the preparation protocol of our SERS substrates.

5.3 Morphological properties

The effect of the plasma-induced dewetting on the morphology of the nano-structures by varying the initial Ag thickness h_0 and exposure time to the air-plasma has been monitored through SEM analysis. The Fig. 5.6(a-c) show the SEM images of SERS substrates obtained by changing the Ag thickness h_0 and fixing the exposure time to air plasma at 120 s.
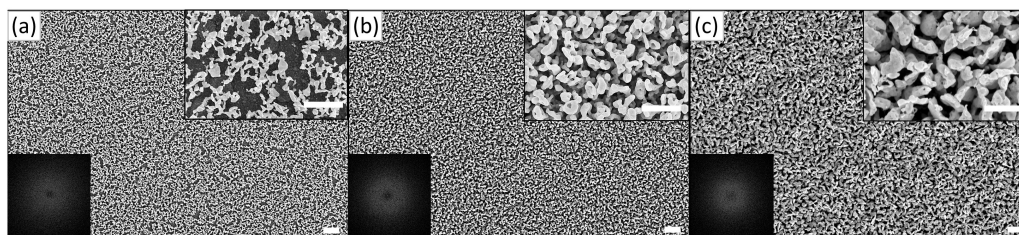

Figure 5.6: SEM images of SERS substrates covered by (a) 10 nm, (b) 50 nm and (c) 200 nm of Ag layer thickness treated for 120 s to the RF air-plasma and 30 s to Argon plasma (scale bar 1 μm). The inset in the upper right corner shows the magnification of the SEM image (scale bar 500 nm), whereas, the inset in the lower left corner shows the PSD.

The PSD calculated for each image, as described in Sec. 4.2.2, shows the typical ring-shape and the radial simmetry that confirm the existence of a long-range order with the characteristic wavelength λ_c and the isotropy of the spinodal-pattern, respectively. As just explained in Ch. 4, although the spinodal dewetting cannot be confirmed due to the multiple effects that can take place during the oxidation process (cracking and/or Kirkendall effect), these outcomes seem to suggest the idea that the nano-structuring could be triggered by the spinodal process. A further analysis of the morphologies have revealed that the average diameter d_{EQPC} of the nano-features increases according to the thickness of Ag layer similarly to the

case of the *Si* wafers seen in Par. 4.3.3. The Table 5.1 summarized the resulting surface parameters relative to the λ_c and d_{EQPC} calculated from each SEM image.

Table 5.1: Statistical surface parameters

Thickness Ag [nm]	$\lambda_c = 1/\nu_c$ [nm]*	d_{EQPC} [nm]**
10	285 ± 2	163 (135, 194)
50	347 ± 2	193 (156, 239)
200	432 ± 2	240 (191, 302)

*ν_c is the peak value of the radial average PSD evaluated from the Lorentzian fit;
**Median (lower quartile, upper quartile).

The effect of the exposure time on the morphologies has been carried out by fixing the thickness of *Ag* layer at $h_0 = 30$ *nm*. The Fig. 5.7 shows the SEM images relative to the substrates treated for 90 and 180 *s* with the corresponding PSD. For a quantitative description, the statistical surface
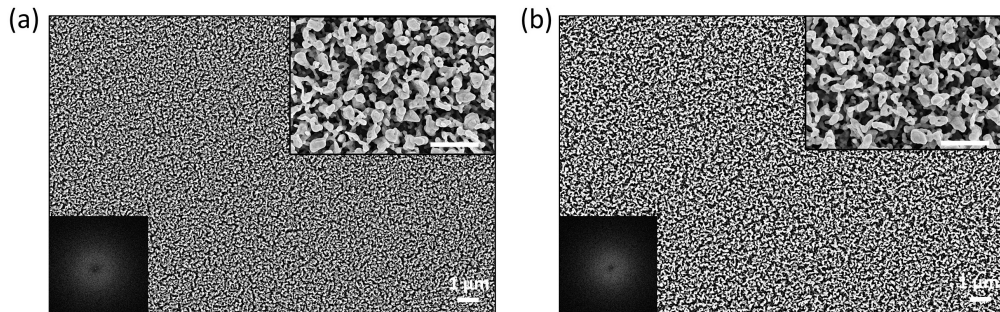

Figure 5.7: SEM images of SERS substrates covered by 30 *nm* of *Ag* layer thickness and treated for (a) 90 *s* and (b) 180 *s* to the RF air-plasma. The inset in the upper right corner shows the magnification of the SEM image (scale bar 500 *nm*), whereas, the inset in the lower left corner shows the PSD.

parameters calculated for both the substrates are summarized in the Table 5.2. Although the average dimension d_{EQPC} of the features seems to be quite constant, a slightly increase in the characteristic wavelength λ_c and the porosity can be observed. Actually, this behaviour should not surprise

considering that it has been previously observed also in the *Si* wafers. A further exposure to the air-plasma contributes only to enlarge the pre-existent cavities formed on the surface by maintaining the periodicity on the nanostructures. These outcomes confirms that the same type of nanostructuring obtained on the TERS probes, can be successfully induced also on the glass coverslips and exploited for the SERS applications.

Table 5.2: Statistical surface parameters

Exposure time [s]	$\lambda_c = 1/\nu_c$ [nm]*	d_{EQPC} [nm]**	Porosity [%]
90	262 ± 1	128 (98, 157)	49
180	338 ± 2	128 (98, 158)	54

*ν_c is the peak value of the radial average PSD evaluated from the Lorentzian fit;
**Median (lower quartile, upper quartile).

Finally, the AFM analysis is used to evaluate the depth of the *coral-like* structure. The AFM analysis was performed in tapping mode on the SERS substrate with $h_0 = 30$ nm and treated for $t_{exp} = 90$ s at air-plasma followed by 30 s of *Ar*-plasma treatment for the reduction process. The tapping mode enables to acquire both topographical (a) and phase (b) map of the surface as shown in Fig. 5.8. As we can see, the phase map shows a higher-contrast pattern, that also resembles the related SEM image, revealing more details with respect to the topographical map. The topographical picture shows some corresponding features but the surface roughness hinders the identification of the single nano-ligament. In fact, the phase of the oscillating tip is not sensitive only to the surface stiffness/softness of the investigated material but also to the adhesion between the tip and surface. The substrate is composed of the same material throughout the entire scan so we do not expect a change in phase due to the material properties. In this case, the pronounced difference in the phase along the edges of the pores that ranges from a minimum of −11° to a maximum of 8°, is due to the reduced contact area between the tip and the sample. Fig. 5.8(c) reports, instead, the height of the topographical map along the blue line

highlighted in part (a) and (b). A more quantitative analysis of the surface is displayed in Fig. 5.8(d), which shows the height distribution of the points of the levered topographical map. As it is possible to see, the 5% to 95% height excursion roughly corresponds to 30 *nm* (a value matching the *Ag*-layer thickness), which suggests that the whole *Ag* layer (not only the uppermost part) is nanostructured.
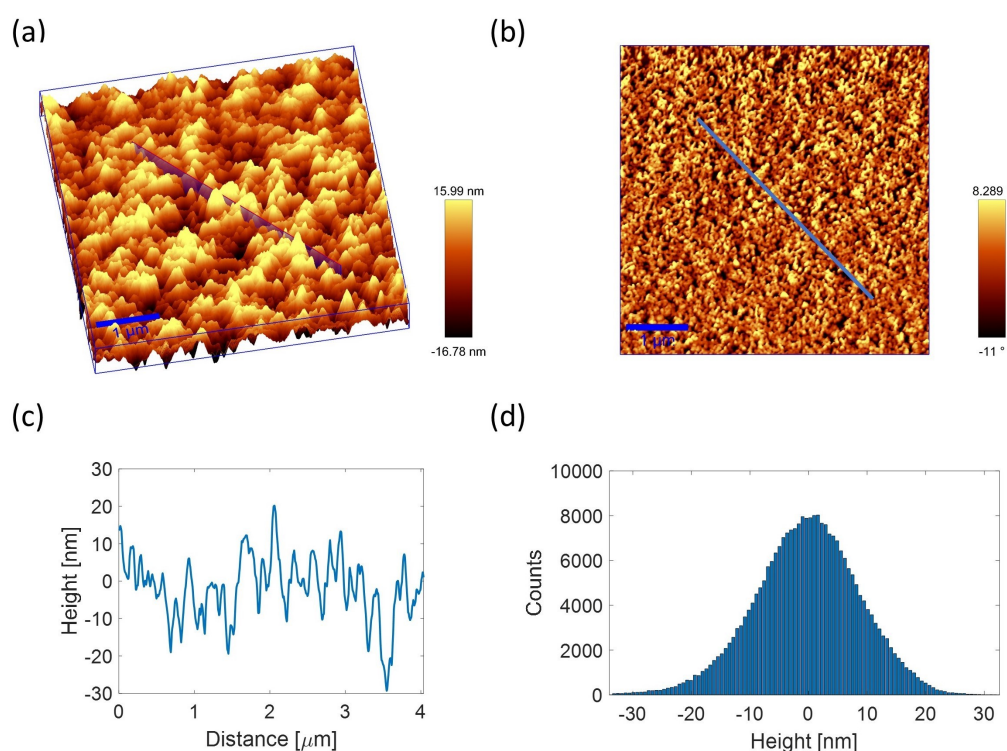

Figure 5.8: AFM analysis of the SERS substrate covered with 30 *nm Ag* layer treated 90 *s* at RF air-plasma. (a) Topographical map in a 5 *μm* × 5 *μm* region obtained by acquiring 512 points for 512 lines; (b) Phase map of the same region in (a); (c) Height profile of the topographical map highlighted in (a) and (b) by the blue line; (d) Heights distribution of the levered map reported in (a).

Anyway, given the complexity of the structure, should not be excluded the hypothesis that deeper pores are not completely reached by the AFM tip and that, thus, the thickness of the nano-structuring could be higher. In fact, a growth of the *Ag*-layer should be expected due the oxidation process as

also observed in the work of El Mel *et al.* [140]. However, a definitive proof of this issue can be, in principle, only obtained by other techniques not available at moment. For example, the scanning transmission electronic microscope (STEM) with Energy Dispersive X-ray (EDX) mapping could be able to provide accurate mapping of sectional *Ag* nano-structuring and identify the *Ag* distribution on the underlying *Au*-layer.

5.4 SERS activity

The optical properties of the *coral-like* substrates are studied by acquiring the diffuse reflectance spectra via UV-Vis spectroscopy (Sec. 3.4). The spectra of the SERS substrates with a 30 *nm* of *Ag* thickness and treated in air-plasma for 90 and 180 *s* are shown in Fig. 5.9. The spectra revealed an

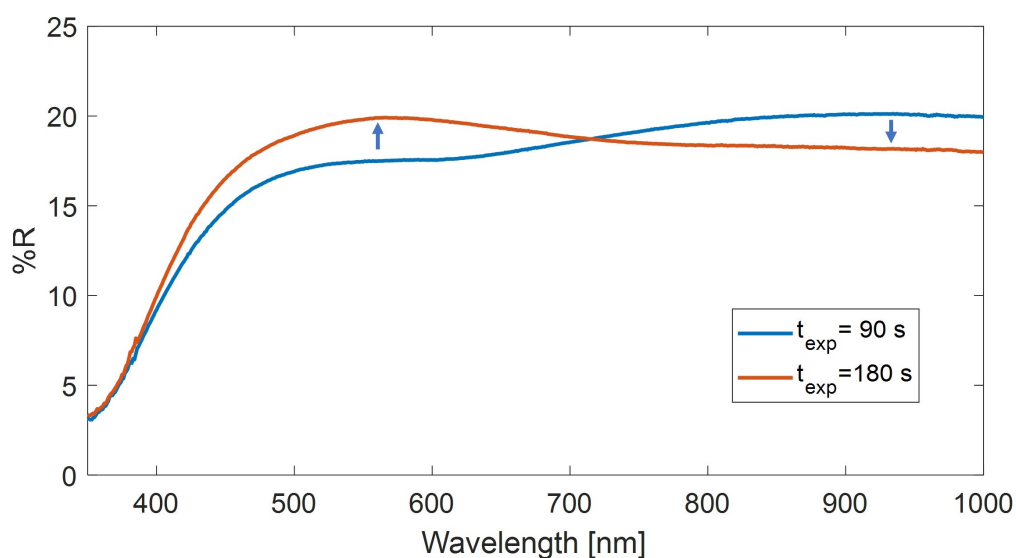Figure 5.9: Diffuse reflectance spectra relative to the substrates covered with 30 *nm Ag* layer treated for 90 and 180 *s* at RF air-plasma followed by 30 *s* of *Ar*-plasma treatment

adsorption edge below 400 *nm* and a large reflectance of intensity $\approx 15-20\%$ in the visible and near-IR region. In particular, at higher exposure times, the reflectance band undergoes a slight decrease in near-IR region and an

increase in the visible one as highlighted by the blue arrows. In any case, the obtained broad plasmonic response enables the use of these substrates for multi-wavelength SERS analysis.

Following the same procedure applied to the TERS probes in the Sec. 4.4.1, the EF of the *coral-like* substrates is evaluated by using the crystal violet (CV) as molecule probe. To carry out the measurements of the SERS signals, 1 μM CV solution is infiltrated in a sandwich-like cell constituted by two parallel plates, the SERS substrate and a microscope slide. The bonding between the two parts is guaranteed with heated parafilm strips that assure a thickness of the chamber of about 130 μm. This geometry assures a slower drying of the CV solution and a more uniform deposition of the sample. After that, the SERS spectra are collected using a power $P_S = 50~\mu W$ and integration time $\tau_S = 1~s$ from a map $10 \times 10~\mu m^2$. The spectra are then mediated and the intensity I_S relative to the peak 1584 cm^{-1} is taken for the calculation. Similarly, the Raman signal I_R relative to the same peak of 5.57 mM CV solution infiltrated in a cell formed by two glass coverslips is acquired with $P_R = 4.5~mW$ and $\tau_R = 10~s$. The Fig. 5.10 shows a comparison between the average SERS and Raman spectrum.

The EF is calculated according to the following expression as:

$$EF = \frac{I_S N_R P_R \tau_R}{I_R N_S P_S \tau_S} \tag{5.1}$$

where N_R and N_S are the number of molecules that contribute to the Raman and SERS signal, respectively. In particular, N_R is the number of molecules contained in the confocal volume $V_C = 2.3~fL$ and, thus, is given as:

$$N_R = c N_A V_C \tag{5.2}$$

where c [mol/l] is the molar concentration of the CV solution and N_A is the Avogadro number. The value N_S, instead, is the number of molecules adsorbed on the SERS substrate in the confocal area $A_C = 0.44~\mu m^2$. Thus, given the surface density $d_s = N_{tot}/S = c N_A V/S$ where V is the volume of sandwich-like cell and S is the area of the SERS substrate ($15 \times 15~mm^2$), N_S

can be evaluated as:
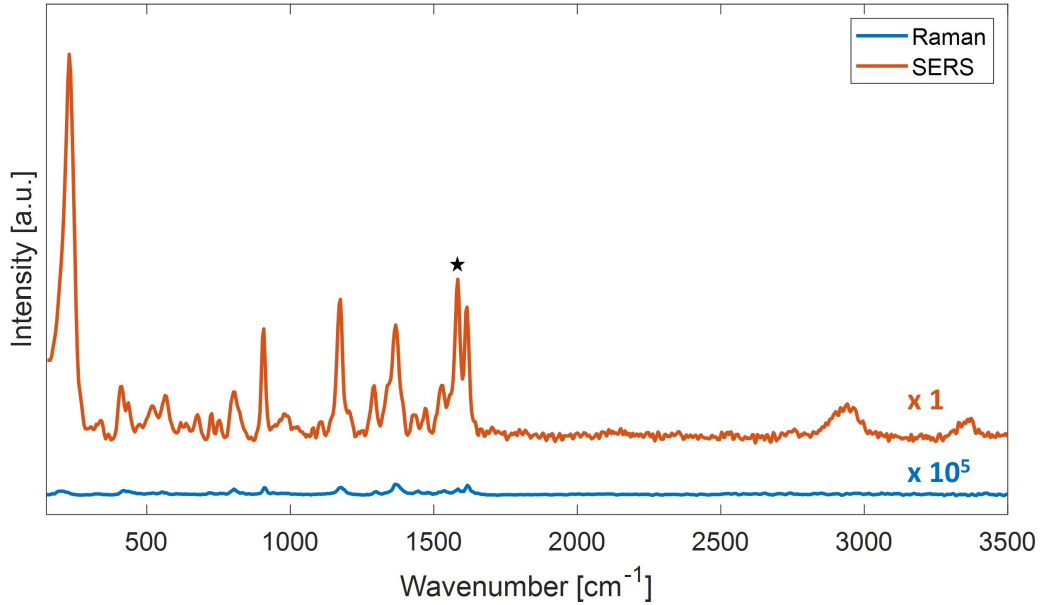
$$N_S = A_C d_s \tag{5.3}$$

Figure 5.10: Comparison between an average SERS spectrum measured in a region $10 \times 10 \ \mu m^2$ on a SERS substrate treated for 90 s in air-plasma and a Raman spectrum. The spectra are normalized with respect the power, molecule's number and integration time. The Raman spectrum is magnified $10^5 \times$ and the peak at 1584 cm^{-1} used for the estimation of the EF is highlighted by the star.

The effect of the exposure time to air-plasma on the plasmonic properties has been evaluated by comparing the EF of SERS substrates prepared at τ_{exp} = 90, 120, 150, 180 s. The results are summerized in Table 5.3.

Table 5.3: Variability of the EF with the exposure time t_{exp}

Exposure time [s]	EF	Exposure time [s]	EF
90	$1.5 \pm 0.3 \times 10^7$	150	$2.3 \pm 0.1 \times 10^6$
120	$2 \pm 3 \times 10^6$	180	$5.60 \pm 0.04 \times 10^5$

Each EF is calculated by mediating the EFs obtained in several regions of $10 \times 10 \ \mu m^2$ (20×20 points) acquired on the corresponding substrate. These

outcomes reveal that the most promising substrate for SERS applications is that treated for 90 s (EF ~ 10^7). In contrast, we note that the EF reduces of even two orders of magnitude for longer exposure times (t_{exp} = 180 s). Looking at the UV-Vis analysis (see Fig. 5.9) it can be noted that the employed excitation wavelength (λ = 532 nm) occurs within the broadband plasmonic resonance for both substrates. The difference found for the two substrates could be ascribed to the higher hotspot density in the 90 s exposure time substrate. Probably, the increment of the porosity and, thus, the enlargement of pores with the exposure time as shown previously, does not promote the generation of a large number of hotspots, resulting in a reduced EF.

Once fixed the exposure time at 90 s, we have evaluated the spatial reproducibility of the SERS signal using a 9.5 μM CV solution deposited on the so-treated substrate. Fig. 5.11(a) shows the SERS signal distribution corresponding to the isolated peak at 906 cm^{-1} of the CV Raman spectra acquired in a region of 10×10 μm^2 with a step of 0.5 $\mu m/points$ (map of 20×20 $points$ with a total of 400 spectra). The distribution is obtained by
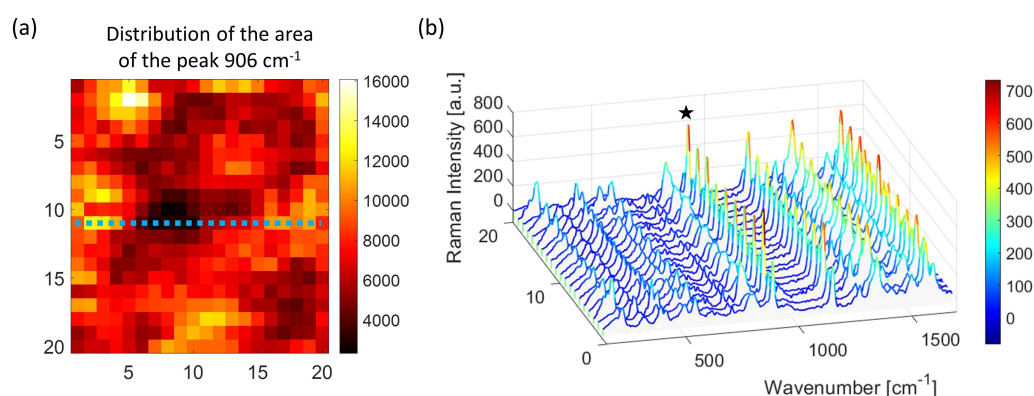
Figure 5.11: (a) Spatial distribution of the SERS signal corresponding to the area intensity of the peak at 906 cm^{-1} acquired in a map $10 \times 10\mu m^2$ (20×20 points); (b) SERS spectra acquired along the blue line of the map (a). The star symbol indicates the peak at 906 cm^{-1}.

mapping point-by-point the area under the investigated peak. The map shows darker regions that does not indicate an absence of the signal as

demonstrated by the Fig. 5.11(b) that reports the spectra acquired along the blue line. Actually, the distribution of the peak intensity shows a relative standard deviation of ~ 30%. Assuming a uniform distribution of molecules on the substrate, the observed signal variability could be ascribed to a point-to-point variability of the substrate EF. It is also true, however, that the procedure followed for a uniform distribution of the CV solution on the substrate could not be effective in case of porous substrates. This doubt, thus, demands further study and clarification that will be explored in the near future.

The SERS substrates have been successfully tested in visible region by using an excitation wavelength of 532 *nm*. Anyway, the broadband sensing performance can be demonstrated by employing different excitation wavelengths. In the next future, the system used in this work thesis will be equipped with a new laser line at 780 *nm* that will allow to test the SERS substrates also in near-IR region.

5.5 Wettability

Beyond the SERS activity, we have also investigated the wetting properties of our *coral-like* substrates. The wettability is the ability of a liquid to maintain contact with a solid surface, and it is controlled by the balance of the intermolecular interactions of liquid-solid and liquid-liquid. In fact, according to the chemistry of the surface and/or its roughness, a water droplet put on a solid substrate tends to spread completely over it (hydrophilicity) or to retain a fairly spherical shape (hydrophobicity). Both these properties are widely investigated in literature due the multiple and relevant applications, including everyday life, as preventing dust, rain and snow adhesion. In particular, the wettability properties of metal nanostructured surfaces are particularly attractive [209–211] due to many industrial applications such as catalysis [212] or supercapacitors [213]. Moreover, there is also some connection between wetting phenomena and SERS activity. As a matter of fact, knowing the wettability of SERS substrates becomes

extremely important especially for biological applications which involve in most cases water-soluble analytes. The hydrophilic substrates allow the solution to spread out and quickly dry on throughout the surface improving the detection efficiency [214]. On the other hand, the hydrophobic surface makes the droplet dry slowly in a single small spot leading to a major concentration of the analyte [215, 216].

The most common way to express the wetting properties of a substrate is the measurement of the static contact angle (SCA) that a liquid droplet (usually water) forms with a surface, In the case of a liquid droplet on a flat and rigid surface (Fig. 5.12(a)), the equilibrium SCA θ is expressed as the balance between the three surface tensions of the solid/vapor γ_{SV}, the liquid/solid γ_{LS} and the liquid/vapor γ_{LV} interfaces by the Young equation:

$$\cos \theta = \frac{\gamma_{SV} - \gamma_{LS}}{\gamma_{LV}} \tag{5.4}$$

In general, the surface is defined hydrophilic/phobic if the SCA of the water is lower/higher than 90°. Anyway, as anticipated, the contact angle is not only affected by the surface chemistry but also by the surface roughness. The Young equation is based on the hypothesis that the surface is homogeneous and smooth. In such cases, the SCA is always smaller than 120° which corresponds to the maximum theoretical SCA of the water on a smooth surface [217].
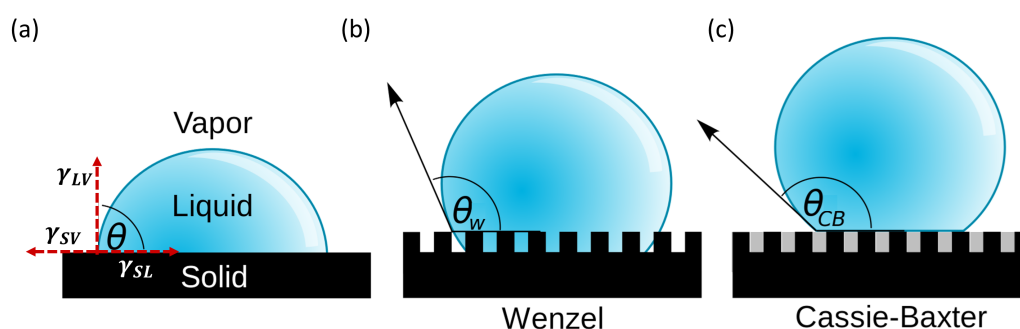

Figure 5.12: Schematics of: (a) droplet resting on a solid flat surface with the contact angle θ given by the Young equation; droplet resting on a textured surface in the (b) Wenzel state and (c) Cassie-Baxter state [218].

A method to altering the wettability is texturing the surface, i.e. modify the surface roughness. The main models used to correlate either phisically and chemically textured structures to the apparent SCA are, respectively, the Wenzel and Cassie-Baxter theories.

The Wenzel model describes the wetting behaviour of a homogeneous surface characterized by a roughness $r = A_r/A_p$ which is the ratio between the real and projected surface area of the substrate. The size of the droplet is assumed to be larger compared with the roughness scale of the surface and the liquid completely penetrates the cavities or grooves on the surface (Fig. 5.12(b)). Given the local SCA θ from the Young equation, the apparent SCA θ_W is given as:

$$\cos \theta_W = r \cos(\theta) \tag{5.5}$$

According to the Wenzel relation, since $r > 1$ a hydrophilic/hydrophobic surface would become more hydrophilic/hydrophobic as the surface roughness r increases. In other words, in the Wenzel state the roughness preserves and magnifies the underlying wetting properties of the substrate.

If the surface is chemically textured (heterogeneous), the apparent SCA can be derived by the Cassie-Baxter model. Let's consider a surface made of two species (in Fig. 5.12(c) are indicated in black and grey) characterized by its own SCA θ_1 and θ_2. Assuming again that the individual areas of these species are smaller compared to the size of the droplet, the apparent SCA θ_{CB} is given by:

$$\cos \theta_{CB} = f_1 \cos(\theta_1) + f_2 \cos(\theta_2) \tag{5.6}$$

where f_1 and f_2 are the fractional surface areas of the two species wetted by the liquid ($f_1 + f_2 = 1$). This model can be generalized to the case of hydrophilic and hydrophobic rough surfaces as follow:

- A hydrophilic textured surface can be seen as a thin porous medium where the water can infiltrate within the cavities of the solid. As result, the substrate can be considered as a mixture of solid and liquid phase. Since the droplet does not wet completely the substrate, we

are in partial wetting regime. Assuming that f and $1 - f$ are the relative fractions of the solid ($\theta_s = \theta$) and liquid ($\theta_l = 0°$) underneath the drop, the Eq. 5.6 becomes:

$$\cos \theta_{CB}^{hf} = f \cos(\theta) + (1 - f) \tag{5.7}$$

Unlike the Wenzel model, the roughness cannot contributes to the total wetting ($\theta_{CB}=0°$) because in partial wetting regime ($\theta \neq 0°$) will always remains islands of liquid emerging above the "absorbing" film. This description is valid and describe correctly the wetting if the liquid impregnates the texture (Cassie impregnating state). The formation of the impregnating film is energetically favorable if $\cos \theta > (1 - f)/(r - f)$. This inequality defines a critical angle θ_c comprises between 0° and 90° below which the condition is satisfied.

- In the case of hydrophobic structures, air pockets could be trapped in the cavities of the surface and lie just below the droplet. In such cases, the substrate is treated as a mixture of solid and air phase. Again, assuming that the two phases are characterized by their respective SCA θ (solid) and π (air) and occupy fractional surface areas f and $1 - f$, the Eq. 5.6 becomes:

$$\cos \theta_{CB}^{hb} = f \cos(\theta) + (f - 1) \tag{5.8}$$

This relation implies a different wetting behaviour with respect the Wenzel model. The apparent angle θ_{CB} increases even for an angle $\theta < 90°$ due to the air pockets trapped under the liquid. In this way, an hydrophobic surface can be obtained from a hydrophilic one. If the angle $\theta > 90°$, smaller values of f (which implies an higher roughness of the surface) contributes to increase the apparent angle θ_{CB} and, thus, the hydrophobicity of the surface. Furthermore, the relation suggests that the ideal angle of 180° can never be achieved because the conditions $f = 0$ or $\theta = 180°$ are not physically realizable. By expanding the Eq. 5.8 around π and assuming the maximum Young

angle of 120° ($cos(\theta) = -1/2$), the apparent angle can at most reaches a value of the order $\pi - \sqrt{f}$ (for $f = 10\%$ the apparent angle is 162°) [219].

Nevertheless, more complex cases of surface wettability that can not be explained by Wenzel or Cassie-Baxter models have been investigated in several other studies [220–222].

Finally, it is worth mentioning that another strategy used to modify the wettability of a surface is treating it chemically by grafting or by adsorbing molecules with its own properties. The glass and silicon, for example, are hydrophilic due their high critical surface tension[1] γ_C (of the order of 150 mN/m). These solids can be made hydrophobic by coating the surface with organic molecular layers of the type $-CH_2-$ that decrease γ_C. In similar way, hydrophobic surfaces as plastics and molecular crystals (low γ_C) can be made hydrophilic by coating them with gold [219].

5.5.1 SCA measurement setup

The most effective method for acquiring the SCA is the drop sessile method which consists in the direct measurement of the angle formed between the three interfacial tensions. The lateral profile of the sessile droplet placed on the surface is photographed and then analysed, generally, using a telescopic goniometer [224]. In our case, the SCAs measurements are carried out by using the home-made setup shown in the Fig. 5.13(b). A volume of 2 μl of pure water (Milli-Q) is gently deposited on the surface sample by using a *Gilson* pipette[2]. The sample is positioned on a holder aligned to the light source for the back-illumination and to the camera for the acquisition of lateral profile of the droplet. The light source, a

---

[1]The critical surface tension is the surface tension at which a liquid just completely wets a solid and is derived experimentally from the Zisman method [223].

[2]If the radius of the droplet is smaller than the capillary length (κ^{-1}), the capillary forces dominates with respect to the gravity and the shape of the droplet remains spherical. The capillary length is estimated by comparing the Laplace pressure γ/κ^{-1} and the hydrostatic pressure $\rho g \kappa^{-1}$ and is defined as $\kappa^{-1} = \sqrt{\gamma/\rho g}$ where ρ and γ are the density and surface tension of the liquid, respectively [219].

white high-power LED (Mod. MCWHL2, *ThorLabs*), is collimated and redistributed by two lens to create an uniform retro-illumination. The image of the droplet is then focused through a convex lens of focal length 10 *cm* to a CMOS camera (Mod. DCC1545M, *ThorLabs*) and analysed.
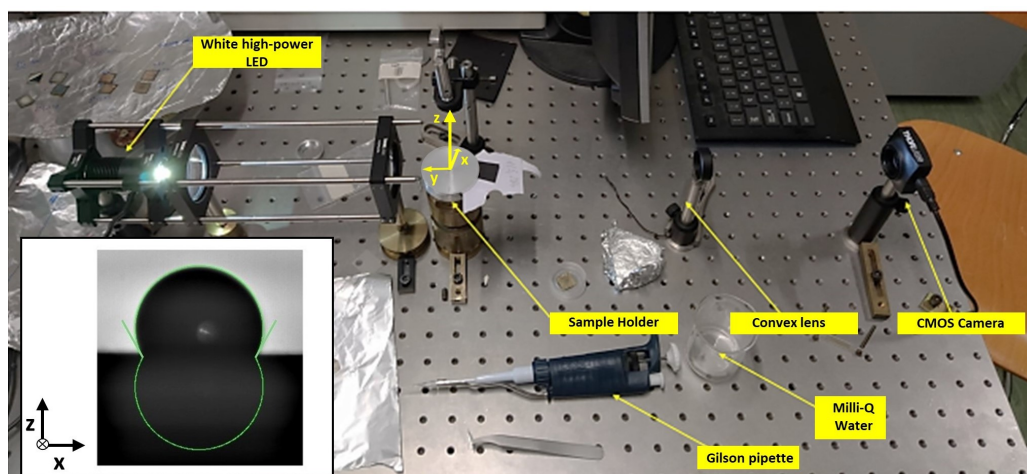

Figure 5.13: Picture of the home-made setup used for the CA measurements. The inset shows the curve fitting the lateral profile of the droplet by using the LB-ADSA approach.

At least five pictures of the droplets placed in different positions of the surface are acquired under ambient conditions. The data are analysed through a plugin, called Low Bond Axisymmetric Drop Shape Analysis (LB-ADSA), for *ImageJ* software. The control of different drop parameters (as diameter, height, position) allows to fit the droplet contour by a theoretical profile with high precision (see inset in the Fig. 5.13). This curve is obtained from the approximated solution of the Young-Laplace equation for axisymmetric drops by using first-order perturbation theory [225]. The final contact angle is calculated as the average of the five values and the error is the standard deviation which can be taken representative of the surface uniformity.

5.5.2 Nano-structuring effect on the wettability

The effects of surface texturing on the wetting properties were studied by comparing the SCA of the *coral-like* surfaces with the SCA of the smooth *Ag* surfaces as freshly prepared. The SCA measurements have been carried out on a set of SERS substrates covered with 30 *nm Ag* layer exposed for different times t_{exp} at the air-plasma followed by 30 *s* of *Ar*-plasma treatment. The upper panel of the Fig. 5.14(a) reports the measured SCA as function of the exposure time t_{exp}.
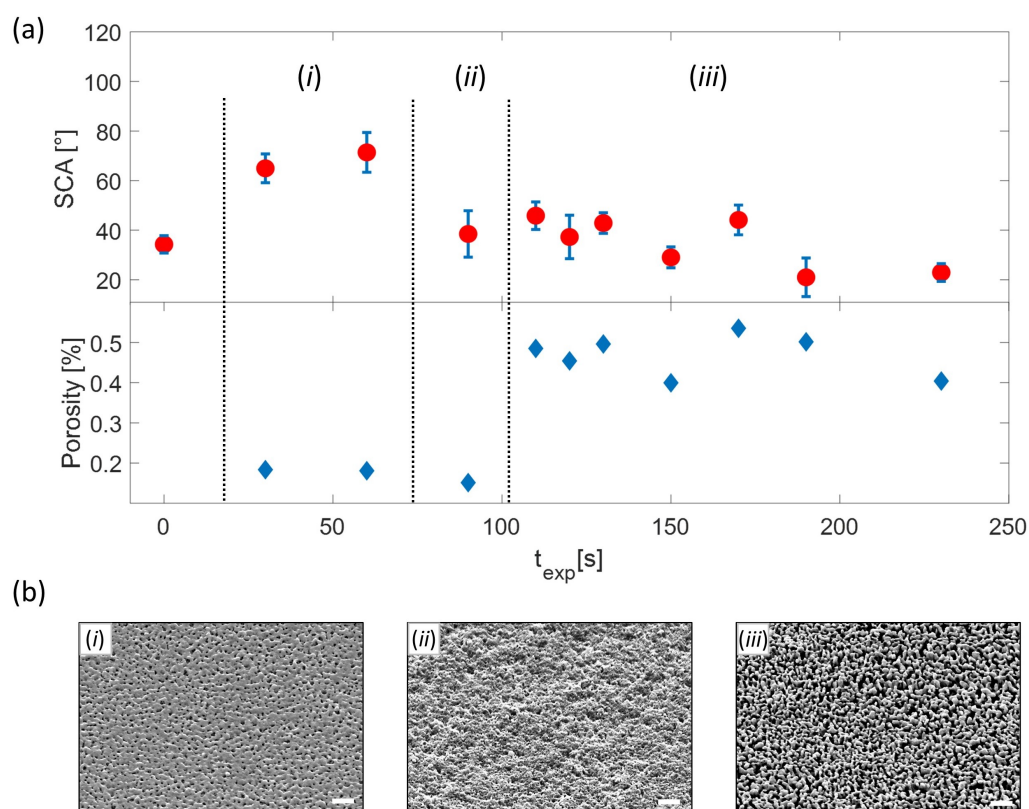

Figure 5.14: (a) SCA and porosity plot of the SERS substrates as function of the exposure time t_{exp}; (b) SEM images relative to SERS substrates treated (*i*) 30 *s*, (*ii*) 90 s and (*iii*) 130 *s*;

The water droplet deposited on the as-prepared smooth *Ag* surface ($t_{exp} = 0\ s$) forms a SCA 34.3° ± 3.5°. This result is in reasonable agreement with the founding of Dutheil *et al* [226] which reports a study of the con-

tact angle in function of the surface roughness of Ag films deposited by a magnetron sputtering. As matter of fact, AFM measurements of the our as-prepared films have revealed an intrinsic roughness of few nm that can explain the contact angle that we found for these surfaces. When the samples are treated with the plasma discharge the surface begins to change. For exposure times $t_{exp} < 60\,s$ the contact angle increases, after which for longer exposure times the contact angle decreases abruptly to settle at a fairly constant trend or with a slight decrease. For a qualitative discussion, the values of the porosity calculated for exposure time is reported in lower panel of the Fig. 5.14(a). By looking the trend of the porosity and the SCA, we can distinguish three wettability regions depending on the morphologies of the Ag surface. For seek of simplicity, the Fig. 5.14(b) shows the representative SEM image for each region. The first region (*i*) corresponds to samples where the nano-structuring process is still not initiated. The surfaces have a low porosity and the SCA is about $20° - 30°$ higher compared to the smooth Ag surface. The second region (*ii*) can be seen as a transition phase. Unlike the other two regions, the surface is characterized by a low porosity and, also, a low SCA. The surface is starting to be structured showing hillocks on the surface. The third region (*iii*) is characterized by samples showing the typical *coral-like* texture and an higher porosity. In such case, the porosity seems to be strictly correlated to the SCA measurements. The type of nano-structuring seems to promote the water filtering in the interstices among the *coral-like* circuit (Cassie impregnating state) and, thus, the hydrophilicity of the substrates.

5.5.3 Aging effect on the wettability

Beyond the nano-structuring effect, has been also analysed the aging effect on the wetting properties of the SERS substrates. In particular, we have verified that by storing the substrates in Ar or N_2 atmosphere, the wettability is preserved. On the other hand, we have noted that the wetting properties drastically change when the substrates are exposed to ambient air for times of order of tens of hours. So, to clarify the mechanism involved in

this changing, the time evolution of the SCA of the SERS substrates stored in laboratory air have been studied. The SCA measurements are taken at various times within a time range of 72 h. The Fig. 5.15(a) reports the time evolution of the wettability of the *coral-like* substrate treated for 120 s in air-plasma.
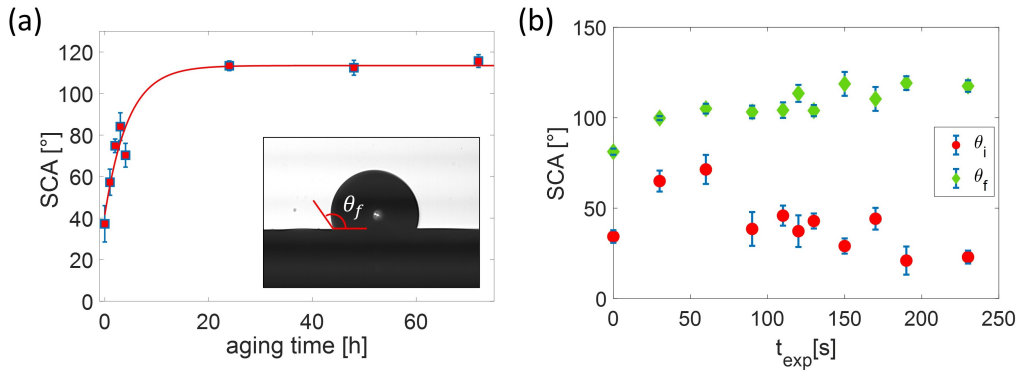

Figure 5.15: (a) Aging time evolution of the SCA measured on a substrate treated for t_{exp} = 120 s to air-plasma. The inset shows the water droplet profile acquired after 72 h of air storing; (b) Comparison between the SCAs θ_i and θ_f relative to the bare Ag and treated Ag surface substrates.

The initial angle θ_i is 37.3° ± 8.7° but after an exposure time of few hours the SCA starts to increase. The rapid growth stops after about 20 h when the SCA reaches a plateau and the final average angle becomes θ_f = 113.5° ± 4.7°. This behaviour reveals clearly that the substrate undergoes a transition from hydrophilic to hydrophobic surface. Such aging time dependence of the measured angles can be described through an exponential function of the type:

$$\theta(t) = \theta_f + (\theta_i - \theta_f)e^{-t/\tau} \tag{5.9}$$

where θ_i and θ_f are the initial and final angles, and τ is the rise time. As shown in the plot, this function (red line) well fits the time evolution of the SCA. The time monitoring of the SCA has been also performed on the smooth Ag and nano-structured surface substrates exposed to RF air-plasma for different times. In both the cases, we have observed the

same wetting behaviour described above. The outcomes of this study are summarized in Fig.5.15(b) where the final SCAs θ_f reached after long-time exposure in air are compared with the initial SCA θ_i measured on each sample. This plot reveals that every sample changes its own wetting properties by converting the hydrophilic surface into a hydrophobic one. In particular, the nano-structured substrates ($t_{exp} > 110\ s$) seem to reach higher final SCAs than the other ones. These results suggest the idea that the aging effect on the wettability of the SERS substrates could be affected not only by the morphology but also by the chemical nature of the aged surface. As a matter of fact, the wettability transition could result from the atmospheric oxidation of the Ag layer [227] or the adsorption of organic contaminants present in the air.

The role of oxidation has been verified by measuring the SCA on an oxidized Ag surface treated only in air-plasma, which is known to produce a thin oxide layer. The measured SCA of 30° ± 3° reveals an hydrophilic nature of the silver oxide. This result is in accord to the work of Mirzaein *et al.* [228] which reports that the silver oxide films are relatively hydrophilic and an increasing oxidation can at most increase the wettability of the films. It is therefore out of the question that the oxidation could affect the wetting properties of the aged substrates.

At this point, we have investigated the chemisorption of organic contaminants present in the air on the substrates. In fact, we have verified that by exposing the aged substrate at Ar-plasma or in ultra-high vacuum, the pristine wetting properties of the surfaces are restored. This observation reinforce the idea that organic contaminants could be effectively chemically adsorbed on the surface. As matter of fact, several works have demonstrate that airborne hydrocarbon compounds can be easily adsorbed on surfaces as graphene [229], heat transfer surfaces [230] or $Ge_2Sb_2Te_2$ (GST) NPs decorated surfaces [231] and that can affect the wetting properties. These studies have showed that the unintentional hydrocarbon contamination promotes the hydrophobic behaviour by lowing surface energy of the material. So, to shed light on the relationship of the airborne hydrocarbons with the wetting properties of the SERS aged substrates, we have kept both

the bare Ag and nano-structured surface for 24 h in saturated atmospheres of toluene (C_7H_8) and heptane (C_7H_{16}). The toluene and heptane have been chosen as representative of an aromatic and aliphatic hydrocarbon to mimic the organic contamination in ambient air. The results are shown in the Table 5.4 where the initial and final SCAs measured on a smooth Ag surface (t_{exp} = 0 s) and a *coral-like Ag* substrate (t_{exp} = 120 s to air-plasma + t_{exp} = 30 s of *Ar*-plasma) are reported.

Table 5.4: SCAs measured in Toluene and Heptane atmospheres

	Smooth		Coral-like	
	θ_i	θ_f	θ_i	θ_f
Toluene	36.4° ± 2.8°	77.2° ± 2.4°	33.5° ± 3.6°	79.4° ± 3.5°
Heptane		78.3° ± 2.2°		84.7° ± 1.2°

As we can see, the final state of both the type of surfaces is characterized by an SCA higher that the initial one. Although the surfaces have not clearly become hydrophobic, the increasing trend of the final SCAs lends to support the former hypothesis, indicating that the wetting changing could be the result of adsorbed airborne hydrocarbons.

Chapter 6

Development of SERS substrates by self-assembly of block-copolymer

In the previous chapter we have illustrated the top-down technique based on the SSD of thin *Ag* layer for the production of SERS-active *coral-like* substrates. In this chapter we present a different approach based on a bottom-up procedure to produce SERS substrates with a high density of hotspots. Such substrates have been employed to reveal the over-expression of a selected protein on the plasma membrane of cells. The results of this bio-application have been published in G. Rusciano, A. Capaccio, E. Sasso, N. Zambrano, A. Sasso, "Revealing membrane alteration in cells overexpressing CA IX and EGFR by Surface-Enhanced Raman Scattering", *Scientific Reports*, Vol. 9 , 1832, **2019**.

6.1   Preparation of the SERS substrates

Among the bottom-up techniques introduced in the previous Sec. 5.1, the self-assembly of block copolymer (BCP) is one of the most promising method to produce dense and ordered SERS nano-structures. The BCPs are macro-molecules composed of different types of polymer chains

linked one to another with a covalent bond. Under certain conditions, these macro-molecules can self-organize into aggregates of diverse morphologies such as spheres, cylinders or lamellae [232]. In some cases, such aggregates can be chemically loaded with metal NPs (*Au*, *Ag*, *Pt*) and used as nano-reactors to control their size and size distribution. Once loaded, these micelles can drive the assembly of NPs into ordered structures allowing to produce a dense cluster of NPs separated only by few nanometers. In fact the gap dimensions can be controlled by changing the molecular weight of the copolymer employed. Such characteristics make this method particularly interesting for the production of well ordered and dense hot-spots distributed SERS nano-structures [233–235].

The method presented herein leads to the formation of a two-dimensional substrate consisting of a random distribution of silver NP-clusters (nanoislands) with characteristics of homogeneity typical of the so-called near hyperuniform disorder [236]. The fabrication is based on the self-assembling of PolyStyrene-block-Poly-4-VinylPyridine (PS-b-P4VP) micelles loaded with silver nanoparticles (*Ag*-NPs) in highly concentrated solution. The synthesis procedure relies on a partially modified procedure, proposed in the literature by Cho *et al* [237] for substrates prepared on silicon supports. In our case we use glass substrates because the back-scattering arrangement of the inverted Raman microscope requires the use of transparent supporting material. The Fig. 6.1 illustrates the steps followed for the development of the SERS substrates.

The first part of the fabrication concerns the preparation of the *Ag*-loaded PS-b-P4VP micelles solution. The Fig. 6.1 (a) shows the structural formula of this block copolymer. The PS-b-P4VP molecule is a diblock copolimer composed by two different polymer chains: the P4VP block possesses a nitrogen atom in the ring, which makes it slightly more polar than the PS block. In apolar solutions the copolymer tends to form micelles with the hydrophobic shell of PS and the hydrophilic core of P4VP which is not soluble in non-polar solvents (Fig. 6.1(b)). Thus, the micelles of PS-b-P4PV are produced by dissolving 100.8 *mg* of polymer with molecular weights equal to 10400-*b*-19200 (polydispersity index of 1.27, Polymer

Source Inc.) in a solution of tetrahydrofuran (THF) (7.0 g) and toluene (10.5 g) for a total volume of 20 ml. The so-prepared solution is stirred for 2 h at 67°C and then for 3 h at ambient temperature. After that, the micelles core is loaded via a coordination complex of the P4VP with Ag ions by adding 200 mg of $AgNO_3$ to the solution (Fig. 6.1(c)). In fact, the presence of the
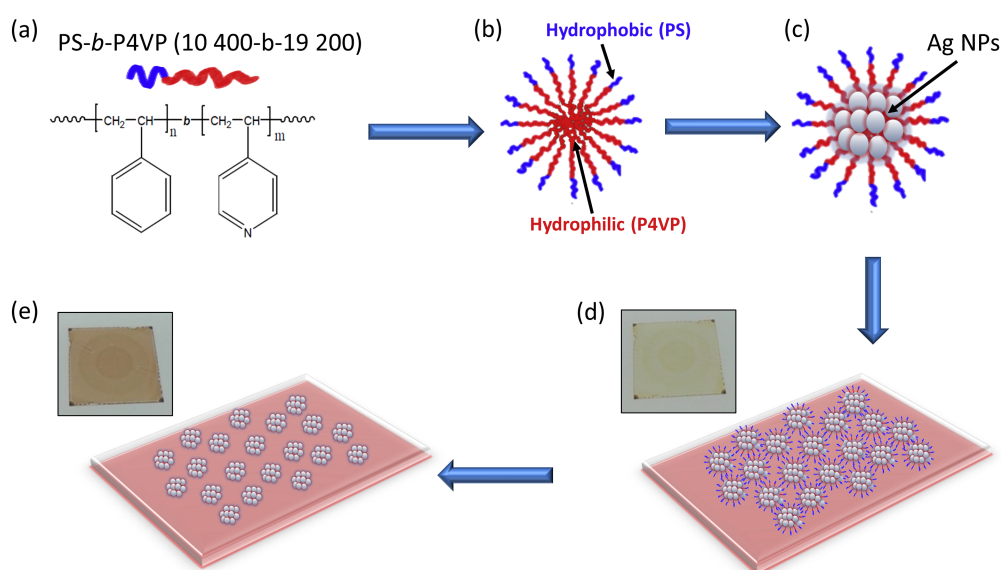

Figure 6.1: Scheme of SERS substrate preparation based on the BCP self-assembling loaded with Ag nanoparticles [238].

nitrogen atom in the P4VP block makes pyridine units suitable to act as binding sites for other polar materials, in this case the $AgNO_3$. After 24 h of mixing, the as-prepared solution is filtered by using PTFE filters with pore size 0.22 μm to eliminate the residues present in the solution. At this point, the Ag ions linked to the micelles core are reduced by adding 50 mg $NaBH_4$ under a controlled atmosphere with low humidity. Finally, the solution is centrifuged and the suspension phase containing only the void micelles removed. The rest of the centrifuged solution is then sonicated in an ultrasonic bath for 22 m and used for the next step.

The second part of the fabrication of the SERS substrate consists in the self-assembling of the Ag-loaded micelles. A droplet of 200 μl of solution is released on a glass coverslip 22 $\times$ 22 mm^2 and distributed by spin-coating

at 2500 *rpm* for 45 *s*. The procedure allows a fast solvent evaporation and, eventually, the formation of a single micelles layer (Fig. 6.1(d)). Subsequently, the polymer is removed by UV radiation that induces the photofragmentation and subsequent evaporation of the polymer, thus leaving only the nano-cluster of silver NPs (Fig. 6.1(e)). Nevertheless, it has been observed that a further exposition to Argon-plasma can successfully contribute to the removal of the polymer residuals.

The surface morphologies of the micellar film is analysed by acquiring the AFM images in tapping mode in a region 0.5×0.5 *mm* of the SERS substrate. The topographical map reported in Fig. 6.2(a) shows an high
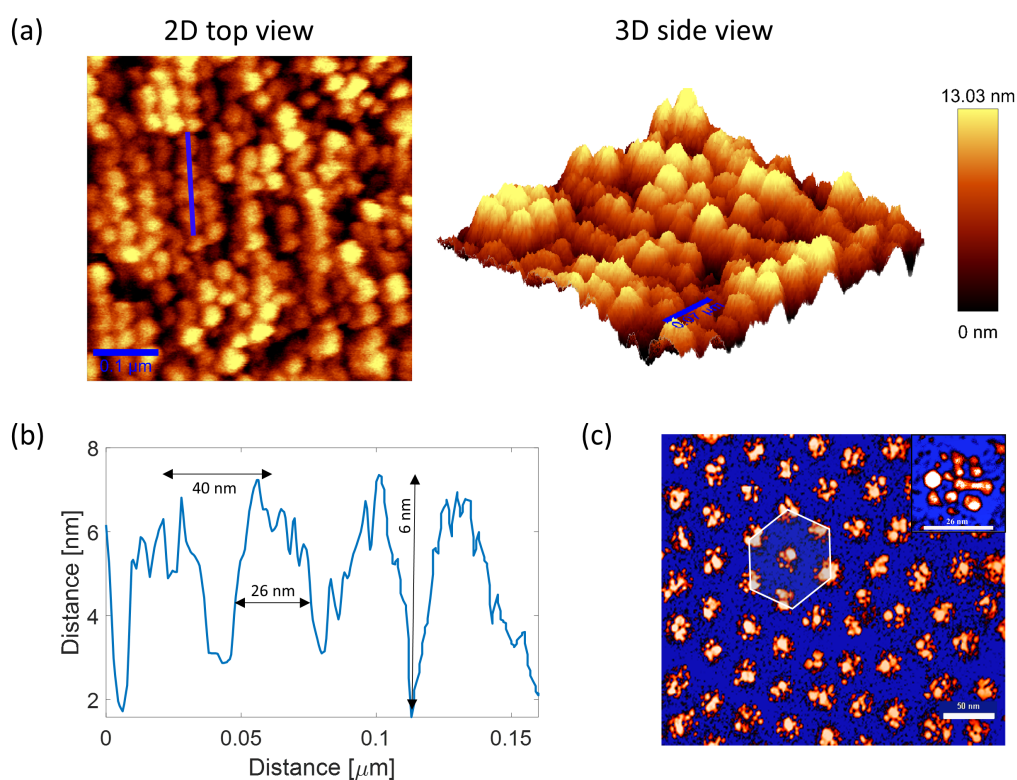

Figure 6.2: AFM images of the SERS substrate: (a) topographical map and (b) cross-sectional profile of the blue line highlighted in the map; (c) TEM image of the resulting *Ag*-loaded micelles film [239].

packing of the *Ag*-loaded micelles with short-range order. The crosssectional profile extrapolated along the blue line and shown in Fig. 6.2(b)

allows to evaluate the micelles' dimensions. Each micelle have an average diameter of 26 *nm* and an average full height of ~ 15 *nm* corresponding to the double of the average height accessible by the tip. The inferior value of the height with respect the lateral dimension should not surprise considering that the deposited micelles tends to relax on the substrate showing a reduced diameter. Moreover, these parameters are in agreement with the ones of the SERS substrates prepared with the same procedure in a previous work by our group [239]. The typical TEM image relative to these substrates are reported in Fig. 6.2(c). As we can see, the average *Ag* nano-cluster diameter is $D \sim 26$ *nm*, while cluster height is $h \sim 14$ *nm*. Each cluster consist of nearly touching *Ag* NPs separated only by few nanometers from one another. In addition, this image shows as the arrangement of the micelles allows to obtain an hexagonal-close-packed (hcp) structure of the *Ag*-NPs clusters. In fact, from the cross-sectional profile plot we can see that each micelle is distanced from its nearest neighbor by ~ 40 *nm* in accord with the periodic arrays distance shown in the TEM image.

6.2 Plasmonic characteristics of the SERS substrates

In the Sec. 2.2, we have seen that the plasmonic properties of the SERS substrates depend on the material and geometry of the nano-features as well as on the interparticle gap between them. In this regard, the resonance characteristics of the substrates have been evaluated at two different densities of the *Ag*-loaded micelles solution. After the suspension phase removal step described beforehand, the remaining solution has been further centrifuged and divided into two phases indicated as *D*1 and *D*2 in Fig. 6.3(a). The two fluids have been collected and used to prepared the corresponding SERS substrate. In order to identify the plasmonic resonances, both the reflection and total transmission spectra have been acquired to estimate the extinction spectra. The so-obtained spectra for both the substrates are

reported in Fig. 6.3(b). The slightly red-shift of the peaks from the density *D*1 to *D*2 suggests that the heavier micelles which are present in *D*2 part are populated by *Ag*-NPs with smaller interparticle gaps. In fact, as discussed in Par. 2.1.2, the near-field coupling introduces a red-shift in the resonance response as the interparticle gap between the NPs decreases. Anyway, the extinction spectra peaked around 480 *nm* are near the wavelength source of our system (532 *nm*) and, thus, the excitation of the LSPR is maximized. The inset of the Fig. 6.3(b) shows that the SERS substrate appears greenish colour when directly illuminated (reflected light).
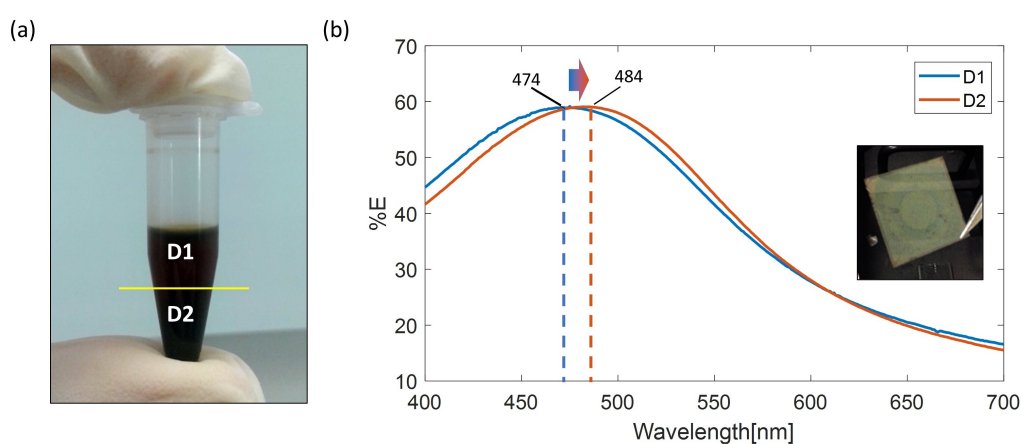

Figure 6.3: (a) Eppendorf tube containing the solution after the second centrifugation. The fluids of density *D*1 and *D*2 are collected at different heights; (b) Extinction spectra of the SERS substrates prepared using the solutions *D*1 and *D*2. The inset shows the SERS substrate in reflected light.

The efficiency of the so-produced SERS substrates in amplifying the Raman signal is evaluated from the enhancement factor (EF). Similarly to the procedure followed in the previous chapter, the EF factor has been calculated by comparing the average SERS and Raman intensities relative to the peak at 1620 cm^{-1} of the crystal violet (CV) spectrum. For the SERS signal, a 0.557 μM CV solution has been infiltrated in a cell composed of a SERS substrate and a glass coverslip of same size distanced by silica beads spacers of diameter 4.55 μm. The signals acquired in a region 20×20 μm^2 of the substrates are mediated and the average I_S used for the calculation.

The SERS spectra have been acquired with an integration time $\tau_S = 1\ s$ and a power $P_S = 1\ \mu W$. The Raman signal of a 5.5 mM CV solution is acquired with an integration time $\tau_R = 1\ s$ and a power $P_R = 1\ mW$. The numbers of molecules contributing to the SERS and Raman signals and the EF are evaluated as described in Sec. 5.4. The calculation of the EF provides the value of the order $\sim 10^7$ with a spatial uniformity of $\sim 5\%$. The Fig. 6.4 shows a comparison between the Raman and SERS spectra normalized with respect to the power.
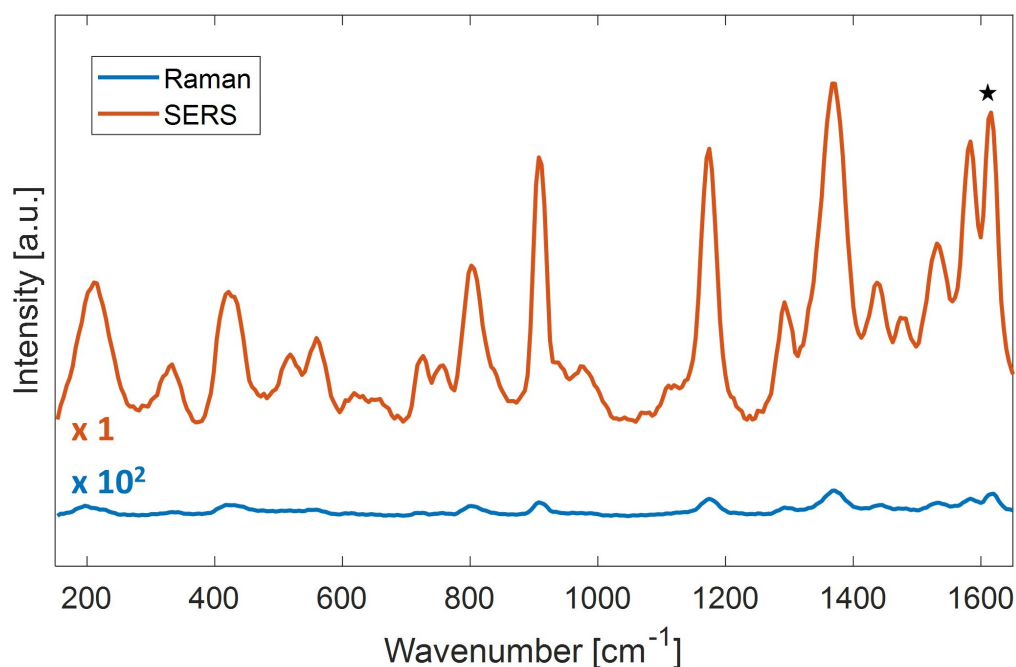

Figure 6.4: Comparison of the average SERS and Raman spectra normalized with respect the power laser. The peak at 1620 cm^{-1} used for the calculation of the EF is highlighted by the black star. The Raman spectrum is magnified 100×.

6.3 Analysis of membrane alteration in cells over-expressing CA IX and EGFR

In view to demonstrate the applicability of the so-prepared SERS substrates, the devices have been employed to reveal the over-expression of target proteins in cell membranes. The SERS technique has proven to be a quite sensitive approach to detect proteins, even in very diluted samples [240]. However, proteins detection in complex environment, such as the cellular membrane, is still a challenge. On the other hand, we have seen in Sec. 2.2.2 that the SERS effect of a molecule placed on the metallic surface decay with the distance as r^{-10}. So, the analysis of biological membranes in contact with a SERS substrate allows to eliminate any contribution due other cellular compartments, conferring a high-contrast to the SERS signals with respect to the bulk Raman contribution [241]. As a matter of facts, the possibility to highlight the contribution of the cytoplasmic membrane from the other cellular compartments opens many opportunities to analyze the role of specific biomolecules in healthy and pathological cells [242, 243]. So, we conduct a proof of concept of the SERS approach by implementing ectopic expression of carbonic anhydrase IX (CA IX) and epidermal growth factor receptor (EGFR) in the plasma membrane of SKOV3 tumor cell line [1]. CA IX is a trans-membrane protein, typically expressed in normal cells after hypoxic treatments. Cancer cells constitutively express CA IX, to support the metabolic shift towards anaerobic glycolysis. In particular, CA IX overexpression represents the expedient by which cancer cells manage to neutralise the acidic pH resulting from the anaerobic metabolism. Accordingly, CA IX expression represents a negative prognostic marker in cancer [244]. EGFR is an integral membrane protein, able to elicit intracellular signalling mediated by a tyrosine kinase activity, after binding to cognate ligands in the extracellular environment [245]. Its activity is often de-regulated in cancer, so that EGFR, as well as additional members of its

---

[1]The study has been done in collaboration with the group of Prof. N. Zambrano of the Department of Molecular Medicine and Medical Biotechnology of the University of Naples "Federico II" and the CEINGE research center.

family of tyrosine kinase receptors, are molecular targets for innovative cancer therapeutics [246].

6.3.1 Transfection efficiency evaluation

The over-expression of the CA IX and the EGFR in the SKOV3 cells is achieved by using the transfection technique. The transfection process is characterized by a statistical variability and its efficiency can be affected by several factors [247]. Regardless of the type of transfection and the method used, the development of a technique capable to identify (and possibly isolate) only the cells in which the process of transfection occurs successfully is required. Thus, the SKOV3 cells have been transfected with CA IX or EGFR in the presence of a vector encoding a fluorescent, EGFP protein (nEGFP), specifically expressed within the nuclear compartment [248]. In such conditions, only cells showing the appropriately excited fluorescence indicate the occurred transfection. The nEGFP protein was preferred to other versions of the EGFP (i.e., cytosolic or membrane-associated), in order to avoid possible interference of a cytoplasmic fluorescence with SERS signal detection at the membrane level. In particular, a 1 : 10 molar ratio of the expression vectors EGFP : CA IX has been selected.

To evaluate the efficiency of transfection, the SKOV3 cells population transfected with CA IX protein gene is analyzed through the fluorescence-assisted cell sorting (FACS). The FACS is a method for sorting a heterogeneous mixture of biological cells into two or more containers, one cell at a time, based upon the specific light scattering and fluorescent characteristics of each cell. In particular, the fluorescence intensity is produced by fluorescent-labeled antibodies detecting proteins, or ligands that bind to specific cell-associated molecules [249]. Fig. 6.5 shows a typical FACS profile of the co-transfected SKOV3 cell populations. The two plots report the fluorescence levels of the APC dye (anti-CA IX antibody) versus the fluorescence intensity for EGFP expression. The left panel shows the FACS pattern of the SKOV3 cells transfected with the only nEGFP (indicated as CAIX$^-$). The plot shows very low basal expression of CA IX and absence of

auto fluorescence in the nEGFP channel. The right plot reports the FACS pattern of the co-transfected SKOV3 cells with both nEGFP and CA IX (indicated as CAIX$^+$). The table reports the percentage of the different cell populations, gated within the $Q1$ to $Q4$ sectors. The values of $Q2$ (36.4%) and $Q4$ (2.0%) gates show that just 5% of cells within the population of cells positive to nEGFP expression ($Q2 + Q4$) can be recognised as false positive for CA IX expression. Therefore, this tests allow to find that we have the 95% of probability of selecting CAIX$^+$ cells.

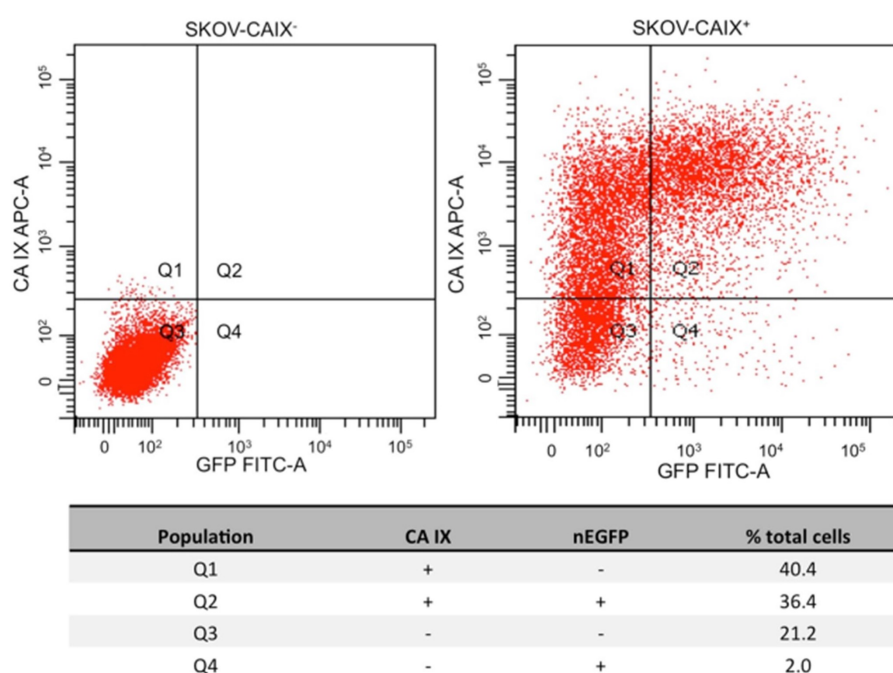| Population	CA IX	nEGFP	% total cells
Q1	+	-	40.4
Q2	+	+	36.4
Q3	-	-	21.2
Q4	-	+	2.0

Figure 6.5: FACS analysis of transfected SKOV3 cell sub-populations. The left plot shows untransfected cells for gating purpose. The right plot shows the FACS pattern of SKOV3 cells transfected with both nEGFP and CA IX expression vectors. The table summarizes the outcomes of the FACS analysis.

In order to identify the fluorescent SKOV3 cells and to perform the SERS measurements, our confocal Raman microscope has been properly modified. Thus, an optical branch devoted to fluorescence excitation/detection was added in upper part of the microscope. In brief, blue light (470nm)

from a fluorescence optical fibre (*M470L3 − C*1) was firstly properly colli-
mated and spectrally filtered, than it was injected into the same microscope
objective 20× used as condenser for bright field illumination and illustrated
in the AFM configuration of the Par. 3.3.1. Cell fluorescence imaging was
accomplished by using the same inverted microscope objective 60× used
for the Raman excitation, coupled to an external CCD camera (Hamamatsu
*C*5985) through a switchable mirror.

6.3.2   SERS measurements

The SERS measurements have been carried out by putting in contact the
SERS substrates with the cells cultured on a glass coverslip. As sketched
in Fig. 6.6(a), the cell coverslip is laid down onto the plasmonic substrate,
allowing cells adhesion by gravity. In order to avoid water evaporation, the
substrate/coverslip sandwich is sealed-off with a thin layer of low vapour
vacuum grease. Optimal adhesion of cells on the plasmonic layer, revealed
by the presence of high intensity SERS signals, is obtained after a few tens
of minutes from sample preparation.

The analysed samples are the SKOV3 cells over-expressing the CA IX
(CAIX$^+$ cells) and EGFR (EGFR$^+$ cells), respectively. The cells transfected
only with the nEGFP are used as control sample and are identified as CAIX$^-$
cells (or equivalently EGFR$^-$). It is worth noticing that this choice allows the
factorisation of any possible interferences of nEGFP in the acquired signals,
as well as any possible cellular stress due to the transfection process. The
SERS spectra are acquired at different times after transfection: session 1
(48 *h*), session 2 (60 *h*), session 3 (72 *h*) and session 4 (96 *h*). SERS data
acquisition protocol has been applied only on CAIX$^+$ and CAIX$^-$ cells
positive to the in-line nEGFP assay. The measurements are performed
by acquiring 20 spectra on a line connecting two opposite cell borders
(Fig. 6.6(b)). Each spectrum is acquired by using an integration time of
2 *s* and an impinging power (on sample) of 10 *μW* in order to avoid any
thermal heating effect. Spectra are acquired over the spectral range from
700 − 1800 *cm*$^{-1}$ (1024 points), with a spectral resolution of ∼ 1.5 *cm*$^{-1}$. In

order to better highlight SERS bands, acquired signals are background-subtracted. Background mainly originates from the presence of polymeric residues on the *Ag*-nanostructures not completely eliminated by substrate exposure to UV lamp. It presents two quite broad bands in the $1300 - 1600$ cm^{-1} region, which can be easily eliminated by a polynomial fit. In any case, as shown in Fig. 6.6(c), the obtained spectra exhibit a high variability, concerning both intensity and bands spectral positions. Given the spatial
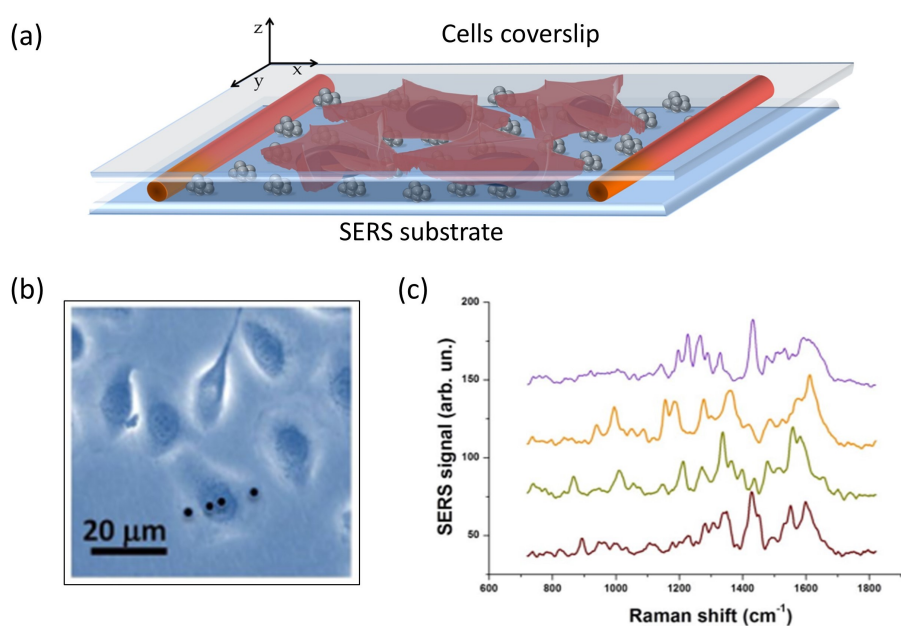

Figure 6.6: (a) Schematic drawing of the sample cell used for SERS analysis; (b) Bright field image from SKOV3 cells analysed in this work; (e) Four background subtrated SERS spectra acquired for the cell shown in (d). They were acquired with a 10 μW laser power (on the sample) and an integration time of 2 s. Spectra were selected in order to highlight the variability, in terms of bands positions, among the acquired signals owning to the same cell.

uniformity of the EF for the employed SERS substrate, there are many causes that can give rise to these fluctuations. The irregular morphology of the cell membrane could be surely an issue, determining changes of the substrate-membrane distance. Moreover, even at a given point, some deleterious impact may be induced by the intermittent contact between

membrane and surface at nanometric scale, due to the intrinsic fluidity of the membrane itself. Overall, we deem it appropriate to carry out spatial and temporal averaging of SERS signals to deal with any unwanted fluctuations.

6.3.3   SERS spectra processing

The ability to distinguish by SERS the effect of over-expression of a single protein at membrane level was accomplished by analyzing the cell populations by Principal Component Analysis (PCA). The PCA is a well-established statistical tool used to emphasize the variation and identify the underlying correlation in a large set of variables (observables). At this purpose, the PCA reduces this large amount of data in a smaller number of uncorrelated variables called principal components (PCs). The PCs are the linear combinations of the original observables and ordered according to their weight in differentiating among different data sets. In particular, the first PC contains the maximum variance from the data, the second PC the next highest amount, and so forth. When applied to Raman spectra, the PCA reduces the information contained in each spectrum composed of a number of points (in our case 1024) equal to the number of observables in only a few variables referred to PCs scores. Typically, the first 3 PCs retain more than 90% of the original information, allowing therefore the representation of each spectrum as a point in a 3-dimensional space (scores plot). In this representation, similar spectra occupy the same score plot region. The origin of points grouping is highlighted by PC loadings, pseudo-spectra which assess the contribution of each wavenumber to the corresponding PC [250]. Thus, the PCA was performed on the Raman spectra using a home-made MATLAB routine, based on the use of the princomp routine.

6.3.4   Interference from culture medium

An important issue to be considered for SERS spectra analysis concerns the role of the protein-rich medium (PBS, eventually mixed with cells

secretions) in which cells lie during measurements. As shown Fig. 6.7(a), the medium gives rise to a detectable SERS signal, clearly identified in this analysis. Hence, by acquiring SERS signals along a line through the
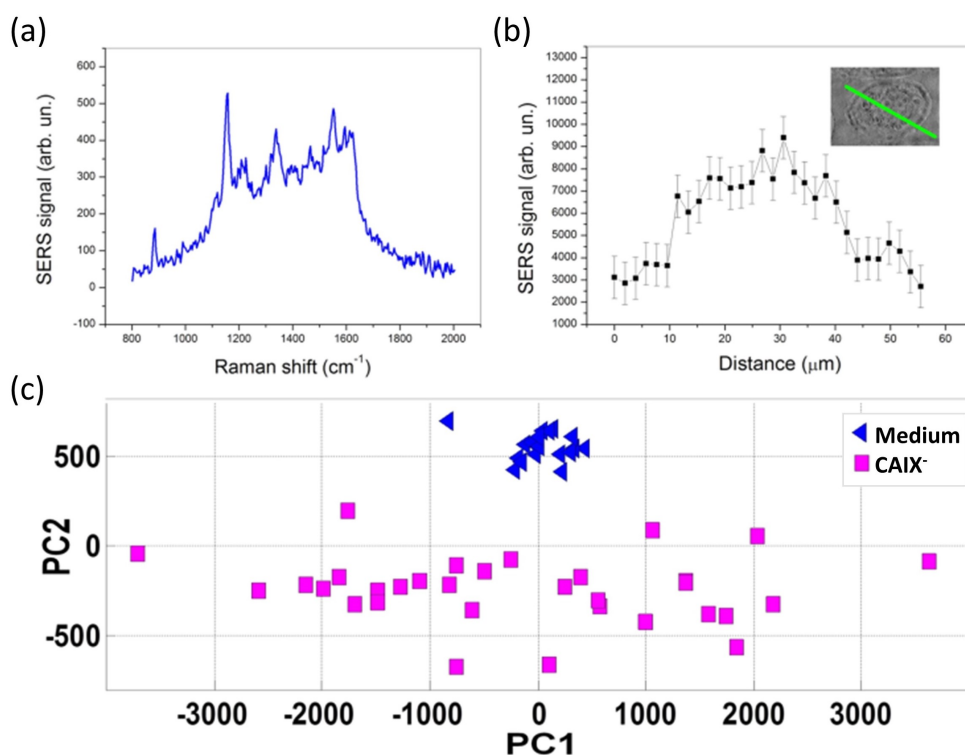

Figure 6.7: (a) A typical SERS spectrum acquired in the medium. (b) Integrated intensity of SERS signal acquired along a line across a cell, as shown in the inset. (c) PCA score plot performed on SERS spectra acquired in the cell medium and CAIX$^-$ cells. Notably, spectra from the medium, which exhibit a relatively high similarity, occupy a quite reduced space in the PC1-PC2 score plot.

cell, starting and terminating in the medium, it is possible to obtain a SERS profile as shown in Fig. 6.7(b). This SERS profile corresponds to the integrated intensity of Amide I band (1620-1680 cm^{-1}). Obviously, the interference from this signal becomes important in the case of poor contact of the cell with the substrate. To face this issue, cells were allowed to adhere to SERS substrate for $\sim$ 30 m before analysis. Moreover, signals were acquired in the thicker cell region (nuclear region) were cells adhesion was

best achieved. In these conditions, a quite good differentiation between signal form cells and from medium was achieved as proved in the score plot of Fig. 6.7(c).

6.3.5   Analysis of cells over-expressing CA IX

The PCA analysis of the CAIX$^+$ and CAIX$^-$ cells spectra are summarized in the Fig. 6.8. The score plot of the part (a) reports the outcomes of
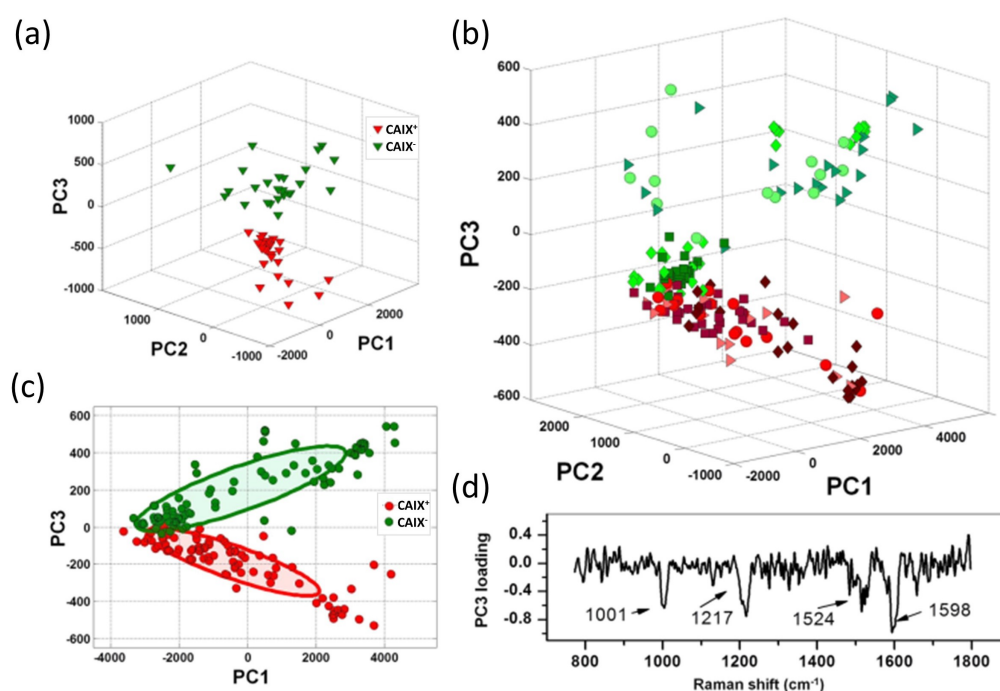

Figure 6.8: (a) PCA score plot of the CAIX$^+$ and CAIX$^-$ cells from the measurements of the session 2; (b) PCA score plot obtained from spectra collected in the 4 different experimental sessions (dots: session 1; triangles: session 2; diamonds: session 3; squares: session 4). Reddish/ greenish colour corresponds to CAIX$^+$/CAIX$^-$ cells; (c) 2D view (PC1-PC3 plane) of the PCA score plot shown in (b) relative to the session 1. The 95% confidence ellipses relative to CAIX$^+$ (red) and CAIX$^-$ (green) are also shown. (d) PC3 loading plot from data shown in part (b). Labels highlight the main spectral feature of PC3 loading.

PCA obtained for a single measurement session (session 2). Each point

represents the average SERS spectrum obtained by mediating the spectra acquired along a line on each cell. As shown, we found a quite good separation between CAIX$^+$ cells (red symbols) and CAIX$^-$ cells (green symbols). Similar results have been obtained for all the other sessions. In particular, the cells prepared at lower confluence and analysed after a longer time lapse from the transfection process have shown a higher clusterization of the scores. Probably, this could be ascribed to a higher presence of daughter cells in the sample, split from parent cells during the mitosis cycles occurred between the two measurement sessions. This reasonably could contribute to homogenise the cellular sample.

The capacity to highlight the presence of CA IX on the cellular membrane is still conserved by processing by PCA the spectra collected in all the investigated 4 sessions (see Fig. 6.8(b)), although at a slightly lower level with respect to the single session. This is absolutely not an obvious outcome because the complex membrane biochemistry might render intrinsically different samples acquired in different sessions. The score plot also shows that a certain clusterization of cells belonging to the same session can still be appreciated, especially along the PC3 score coordinate. Looking at the loading relative to the PC3 component (see Fig. 6.8(d)), we notice that all the peaks of this loading can be attributed to protein components, while no lipid-related feature can be observed (e.g. in the region around 1440 cm^{-1}), suggesting that the difference highlighted by this loading is not amenable to modification of lipids induced by the transfection process.

In order to test the reliability of our SERS based assay of cellular membranes, we use the leave-one-out cross validation (LOOCV) procedure. Calling N the total number of analysed cells, PCA is calculated using $N-1$ spectra (training set), and the scores of the left-out spectrum are calculated projecting it on the PC vectors of the training data. Therefore, this spectrum is attributed to a given sample by evaluating its position with respect to the 95% confidence ellipse of the training data (whose classification was assured known) in the space of the first three scores. This procedure is iteratively repeated until all the spectra set were left out. The Fig. 6.8(c) reports

the 95% ellipse relative to all data. It is worth noticing that these ellipses remain substantially unchanged in the iterative procedure of LOOCV, which suggests a sufficient data sampling of our analysis. The results of LOOCV analysis are summarised in the confusion matrix shown in Table 6.1. From the elements of this matrix, it has been possible to estimate a sensitivity ~ 94%, a specificity ~ 93% and a global accuracy ~ 94% of our SERS-based approach for CAIX detection.

Table 6.1: Confusion matrix

True/Predicted	CAIX+	CAIX-
CAIX+	77	5
CAIX-	4	76

Spontaneous Raman vs SERS A further analysis on the SKOV3 cells over-expressing CA IX has been done to highlight the sensitivity of SERS technique with respect the spontaneous Raman spectroscopy (RS). The Fig. 6.9(a) shows a comparison between the typical Raman (left panel) and SERS (right panel) average spectra obtained by mediating 20 points along a line on a cell. Notably, both signals are acquired by using the same integration time (2 s), while the laser power is three orders of magnitude higher for the spontaneous Raman case. Besides, we remark that Raman signals exhibits DNA related spectral features (such as the peak at 784 cm^{-1}) coming from the nuclear region, while all SERS features can be ascribed to lipids and proteins [251]. The PCA score plots obtained from both spontaneous Raman (left) and SERS (right) spectra of SKOV3 cells is reported in Fig 6.9(b). In both cases, red and green symbols represent the $CAIX^+$ and $CAIX^-$ cells, respectively. No difference between $CAIX^+$ and $CAIX^-$ cells is detected for spontaneous RS measurements for the first three score orders, the same being true for higher orders PC (data not shown). On the other hand, a complete separation between $CAIX^+$ and $CAIX^-$ cells is obtained in SERS analysis, highlighting a higher sensitivity of SERS to membrane modifications.
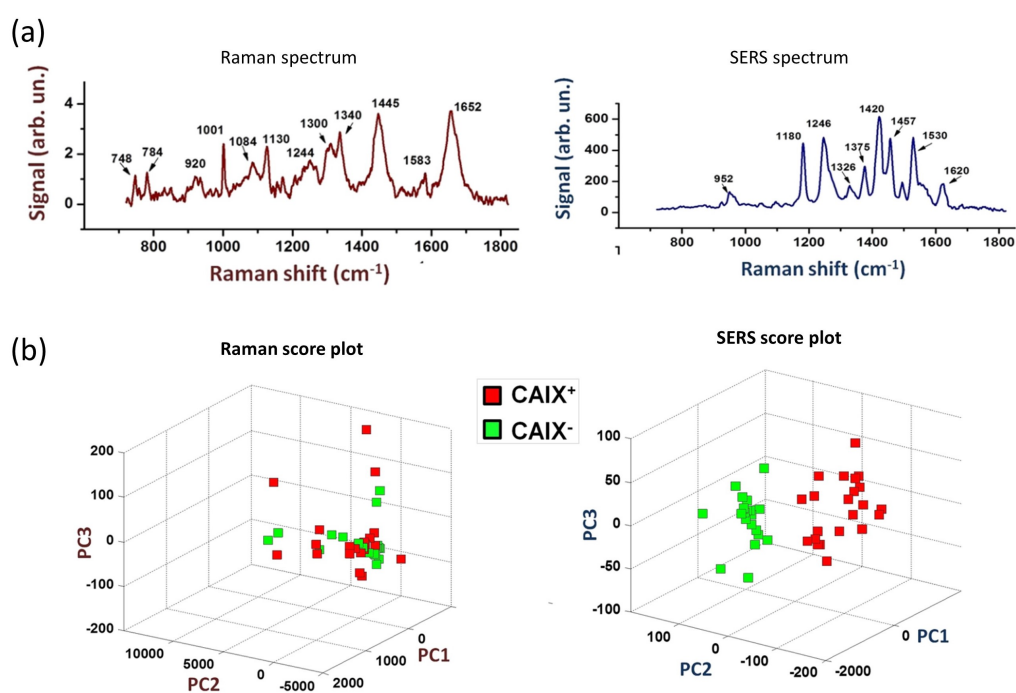
Figure 6.9: (a) Comparison between Raman (left) and SERS (right) spectrum. In both cases, the main spectral features are highlighted by labels reporting their spectral position; (b) PCA score plots of the CAIX$^+$ (red) and CAIX$^-$ (green) cells relative to the Raman (left) and SERS (right) measurements.

6.3.6 Analysis of cells over-expressing EGFR

Finally, we present the SERS analysis of the SKOV3 cells over-expressing the protein EGFR. Again, SERS analysis reveals a quite relevant capacity to distinguish EGFR$^+$ cells with respect to cells transfected in order to express only nEGFP (EGFR$^-$ that we will referred to as "control"), as clearly shown in Fig. 6.10(a). Moreover, as for the CAIX case, we verified that
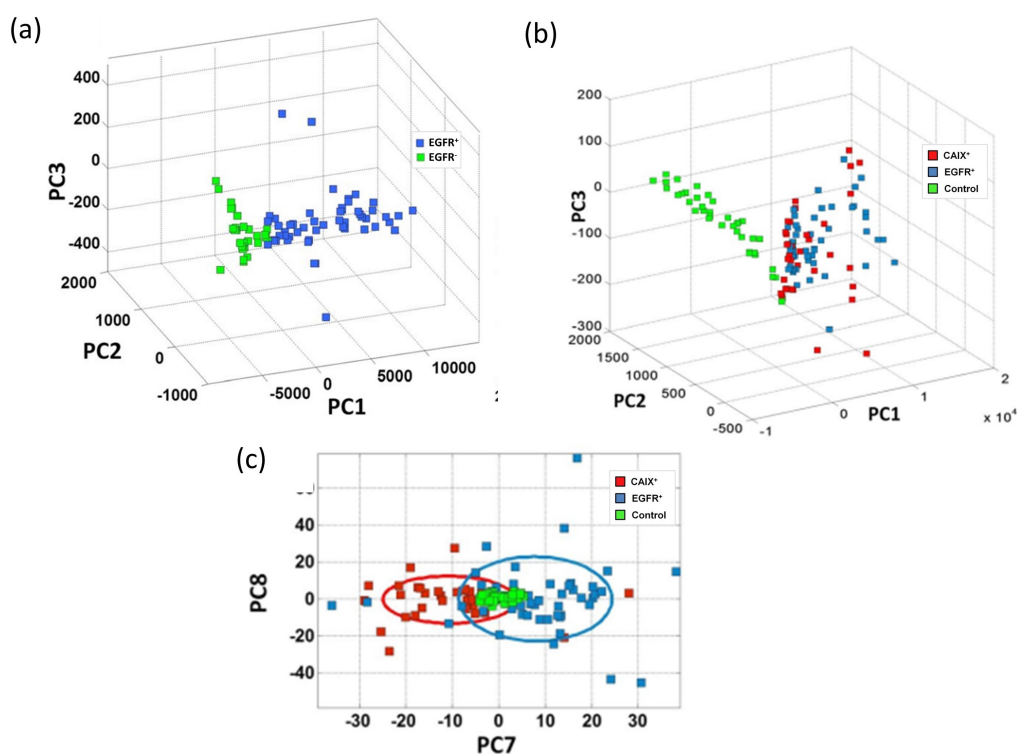

Figure 6.10: (a) PCA score plot obtained by SERS analysis of EGFR$^+$ and EGFR$^-$cells; (b) Score plot obtained by PC analysis of SERS spectra from EGFR$^+$, CAIX$^+$ and control; (c) 2D scatter plot (PC7-PC8 plane) from the same data analysed in (b). Samples are differentiated, to a good extent, along the PC7 coordinate, which describes around 2% of variability among samples.

spontaneous Raman is not able to discriminate cells over-expressing EGFP on the cytoplasmic membrane. As a further step, we checked the level of selectivity of our SERS-based approach to distinguish the over-expression of two target proteins. Hence, we applied PCA to CAIX$^+$, EGFR$^+$ and

control cells, which lead to the scatter plot reported in Fig. 6.10(b). Clearly, in this plot, CAIX$^+$ and EGFR$^+$ cells (red and blue squares, respectively) are separated from the control sample, while no difference was found between CAIX$^+$ and EGFR$^+$ cells, which, in fact, occupy the same score plot region. As a matter of fact, cells showing CA IX or EGFR expression may result indistinguishable due to elicitation of similar membrane perturbations, which may not be dependent on the size, the protein sequences and the glycosylation patterns of the extracellular domains exposed on the plasma membrane. However, by limiting the analysis to only CAIX$^+$ and EGFR$^+$ cells (therefore not including control cells), a good differentiation between the two different samples is again obtained, with a global accuracy $\sim$ 90% (data not shown). This outcome suggested us to check the discrimination capability (among CAIX$^+$, EGFR$^+$ and control) at higher PCs. Discrimination among samples was revealed, to a certain extent, by PC7, a component which describes only $\sim$ 2% of variation of SERS data. The Fig. 6.10(c) shows this outcome. In the same plot, the 95% confidence ellipses for all the samples are also displayed. It is worth noticing that control cells exhibit a relatively small area in the plot, which suggests a more pronounced homogeneity of control cells with respect to the CAIX$^+$ and EGFR$^+$ samples. However, it should be noticed that the use of a high order PCs (describing therefore only a little variation among data), casts doubts upon the reproducibility of the here obtained experimental outcome.

Conclusions

The development of reliable and effective plasmoni devices for SERS and TERS applications represents the major obstacle towards a wider diffusion of TERS/SERS as powerful analytical tools in material science and life science. In the case of TERS, the main technological challenge is based on the fabrication of metal nano-structures on the tip. Compared to SERS substrates that are produced on large-area surfaces, the sub-micron dimensions of the tip apex make the nano-structuring task more tricky. In the first part of the present work thesis, we showed a novel and versatile method for the preparation of appropriate AFM-TERS tips and SERS substrates, developed in this work thesis. The application of a RF ICP in air atmosphere on *Ag*-sputtered surfaces has demonstrated to induce a uniform *coral-like* texture on the overall surface. Although the mechanism of nano-structuring is not yet completely clarified, a key role seems to be played by the oxidation of the metallic layer. The oxidation could contribute to induce a cracking and/or Kirkendall voids in the as-oxidized *Ag* layer. These processes are not sufficient to explain the spatially correlation observed between the nano-features of the *coral-like* pattern and the existence of a long-range order with a characteristic wavelength. Since the pattern resembles the classical picture of spinodal decomposition, it has been suggested the idea that the nano-structuring could be triggered by a spinodal solid-state dewetting process. Anyway, further studies could bring us more knowledge on the mechanism of the nano-structuring formation. Beyond the phenomenology of the process, we have demonstrated the versatility of this technique by successfully obtaining metallic nano-

structures on both TERS probes and SERS substrates. Moreover, we have also shown the effectiveness of the ICP treatment in *Ar*-atmosphere in cleaning tips from organic contaminants typically collected on the tip during the TERS analysis, which results a serious drawback for the analysis of biological systems. The obtained probes are endowed with a high ($\sim 10^7$), a quite reproducible EF and an upper limit of the lateral resolution equal to ~ 10 *nm*, in agreement with the typical spatial resolution estimated by AFM-TERS. It is worth noting that compared to the *s-type Ag*-tip, the *Ag coral-like* tips can be used in no-gap configuration allowing to achieve a high spatial resolution by using the tip alone without electromagnetic coupling with a metallic substrate. As result, this advantage paves the way for the applicability of TERS probes to the study of thicker samples. As regards the SERS substrates, the optical characterization have shown that the *coral-like* shape provides a plasmonic broad-band response in visible and IR-region that, thus, enables the applicability of such devices to multi-wavelength SERS analysis. Although the investigation of these substrates deserves additional studies, at the excitation wavelength investigated, the substrates have shown a high EF $\sim 10^7$ with a spatial uniformity $\sim 30\%$. Beyond the SERS properties, the wettability of the *coral-like* substrate have also been investigated. In particular, we have observed that the porosity of the nano-texture renders the SERS substrates very hydrophilic. In addition, we have verified that the storing conditions of the substrates strongly affect the wettability properties. Compared to the inert gases (N_2 or *Ar*), the air atmosphere exposure tends to make the substrates hydrophobic. Moreover, the nano-structuring of the surface promotes this tendency. So, in order to shed light on this issue, we conducted some studies that led us to highlight the possible involvement of airborne contaminants.

In the last chapter we also presented a bottom-up technique for the fabrication of SERS substrates and a biological application. We have seen that the self-assembly of *Ag* NPs-loaded PS-b-P4VP micelles on glass coverslip enables the production of SERS substrates consisting of a random distribution of silver NP-clusters. The morphological characterization of the substrates revealed a hexagonal arrangement of the NPs nano-islands

and an high packing of the *Ag* NPs that promotes the generation of multiple hotspots. In addition, the optical characterization showed a plasmonic resonance around ≈ 480 *nm* and an high EF $\sim 10^7$ with a spatial uniformity of $\sim 5\%$. Finally, we have demonstrated that the SERS analysis of cell membranes is able to reveal membrane alteration induced by over-expression of a model membrane protein. This intrinsically label-free approach could be quite useful in many contests. For instance, it could provide precious information on the dynamic transformation of cells induced by external stresses, including drugs administration. Moreover, SERS could be a quite powerful tool for early diagnosis of over-expression of cancer-related proteins, such as CA IX and EGFR, exposed on the cell membrane. Anyway, the SERS-based approach suffer from some limits concerning in particular its selectivity. In particular, our approach fails in discriminating among CAIX+, EGFR+ and control cells, unless pushing PCA to high order, and therefore poor significant, components. Moreover, its efficiency reasonably depends upon the specific protein involved in the investigation. Nevertheless, our results demonstrate the possibility to highlight differences in the protein framework of cellular membranes. In particular, it is reasonable to envisage a quite good sensitivity of our approach to reveal membrane transformation, since such processes typically involve a consistent change of the membrane protein pattern (e.g. malignant transformations). Globally, our results pave the way for a label-free membrane analysis, a fundamental issue for both fundamental biomedical studies and applied researches devoted to sensors development.

Acknowledgements

Author's publications

Papers included in this thesis

1. G. Rusciano, A. Capaccio, E. Sasso, N. Zambrano, A. Sasso, "Revealing membrane alteration in cells overexpressing CA IX and EGFR by Surface-Enhanced Raman Scattering", *Scientific Reports*, Vol. 9 , 1832 (2019);

2. A. Capaccio, G. Rusciano, A. Sasso, O. Tarallo, "Coral-like plasmonic probes for Tip-Enhanced Raman Spectroscopy", *Nanoscale*,12(48),24376-24384 (2020).

   N.B. The paper has been selected as back cover on Nanoscale (Fig. A);

3. A. Capaccio, A. Martinez, G. Rusciano, A. Sasso, "Broad-band plasmonic platforms for Surface Enhanced Raman Spectroscopy", (work in progress);

Additional Papers not covered in this thesis

1. G. Rusciano, A. Capaccio, G. Pesce, A. Sasso, "Experimental study of the mechanisms leading to the formation of glistenings in intraocular lenses by Raman spectroscopy", *Biomed. Opt. Expr.*, Vol. 10, 4 (2019);

2. A. Capaccio, G. Rusciano, A. Sasso, "Raman Analysis of Tear Fluid Alteration Following Contact Lense Use", *Sensors*, Vol. 19(15), 3392 (2019);

3. A. Capaccio, S. Caserta, G. Rusciano, A. Sasso, S. Guido, "Dissolution of aqueous surfactant solutions investigated by combining time-lapse polarized light microscopy and confocal Raman spectroscopy", *Journal of Colloid and Interface Science*, Vol. 591, 136-146 (2020);
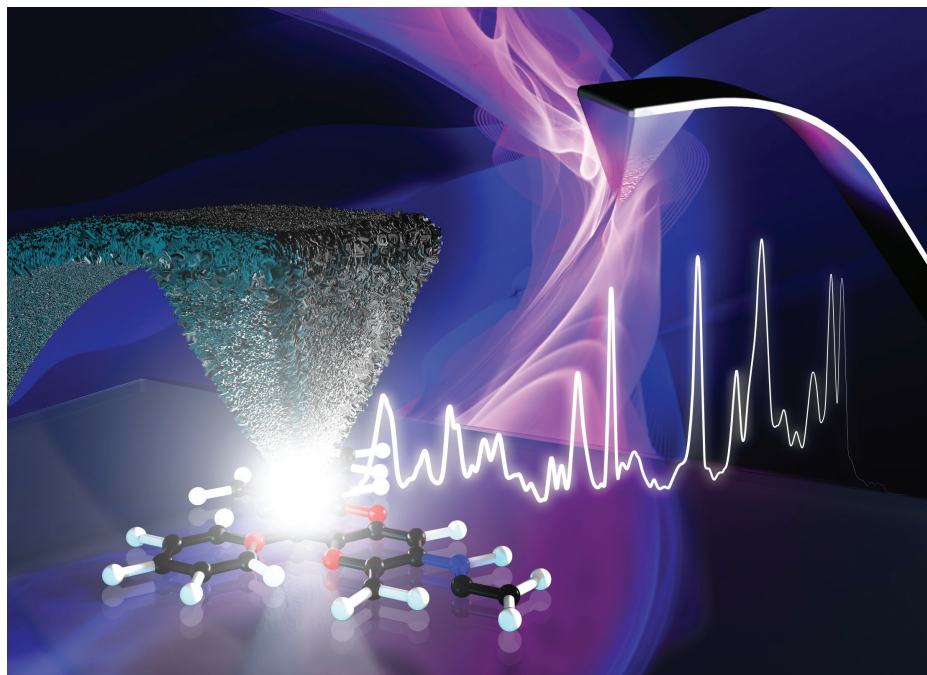
Showcasing research from the group of Prof. G. Rusciano and Prof. A. Sasso at the Laboratory of Nano-Spectroscopy, University of Naples "Federico II".

Coral-like plasmonic probes for tip-enhanced Raman spectroscopy

Tip-enhanced Raman spectroscopy probes confine light to a nanometric region, enabling access to chemical information of systems at nanoscale. When prepared by spinodal dewetting of Ag-coated AFM-tips, they appear covered by a coral-like silver nanotexture, endowed with an excellent plasmonic activity.

As featured in:
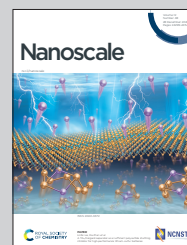
Nanoscale

See Giulia Rusciano *et al.*, *Nanoscale*, 2020, **12**, 24376.

ROYAL SOCIETY OF CHEMISTRY

rsc.li/nanoscale

Registered charity number: 207890

Figure A: Back cover of Nanoscale, vol. 12, issue 48, 2020 [252].

Bibliography

(1) M.Fleischmann, M.; Hendra, P.; McQuillan, A. *Chem. Phys. Lett.* **1974**, *26*, 163–166.

(2) Raman, C.; Krishnan, K. *Nature* **1928**, *121*, 501–502.

(3) Raman, C. *Indian J. Phys.* **1928**, *2*, 387–398.

(4) Rodriguez-Saona, L.; Ayvaz, H.; Wehling, R. L. In *Food Analysis*, Nielsen, S. S., Ed.; Springer International Publishing: 2017, pp 107–127.

(5) Ferraro, J.; Nakamoto, K.; Brown, C., *Introductory Raman Spectroscopy*, 2nd ed.; Elsevier Inc.: 2003.

(6) Nemets, V.; Petrov, A.; Solov'ev, A. *J Appl Spectrosc* **1987**, *47*, 975–985.

(7) Kuhar N. Sanchita Sil, S.; Taru Verma, T.; Umapathy, S. *RSC Adv.* **2018**, *8*, 25888–25908.

(8) Cordero, E. et al. *J Biomed Opt.* **2018**, *23(7)*, 1–23.

(9) Chiu, L.; Ichimura, T.; Sekiya, T., et al. *Sci Rep* **2017**, *7*, 43569.

(10) Scatena, E.; Baiguera, S.; Del Gaudio, C. *Journal of Healthcare Engineering* **2019**, *14*, 1–11.

(11) Kumamoto, Y. et al. *Acta Histochem Cytochem* **2018**, *51(3)*, 101–110.

(12) Toporski, J.; Dieing, T.; Hollricher, O., *Confocal Raman Microscopy*, 2nd ed.; Springer, Cham: 2011; Vol. 158.

(13) Borman, S. *Anal. Chem.* **1982**, *54(9)*, 1021A–1026A.

(14) Rigneault, H.; Berto, P. *APL Photonics* **2018**, *3(9)*, 091101.

(15) Cialla-May, D.; Michael Schmitt, M.; Popp, J. *Physical Sciences Reviews* **2019**, *4(6)*.

(16) Jones, R.; Hooper, D.; Zhang, L.; Wolverson D.and Valev, V. *Nanoscale Research Letters* **2019**, *14(231)*.

(17) Wang, X.; Huang, S.-C.; Hu, S.; Yan, S.; Ren, B. *Nature Reviews Physics* **2020**, *2*, 253–271.

(18) Long, D., *The Raman Effect: A Unified Treatment of the Theory of Raman Scattering by Molecules*, 1st ed.; John Wiley and Sons Inc.: 2002.

(19) Lewis, I.; Edwards, H., *Handbook of Raman Spectroscopy From the Research Laboratory to the Process Line*, 1st ed.; CRC Press: 2001.

(20) Gillet, Y.; Kontur, S.; Giantomassi, M.; C., D.; Gonze, X. *Sci. Rep.* **2017**, *7*, 7344.

(21) Le Ru, E.; Etchegoin, P., *Principles of Surface-Enhanced Raman Spectroscopy and related plasmonic effects*, 1st ed.; Elsevier: 2009.

(22) Parson, W. W. In *Modern Optical Spectroscopy: With Exercises and Examples from Biophysics and Biochemistry*; Springer Berlin Heidelberg: Berlin, Heidelberg, 2015, pp 513–547.

(23) Efremov, E.; Ariese, F.; Gooijer, C. *Analitica Chimica Acta* **2008**, *606*, 119–134.

(24) Jehlička, J.; Edwards, H. G. M.; Oren, A. *Applied and Environmental Microbiology* **2014**, *80(11)*, ed. by Müller, V., 3286–3295.

(25) Wade, J.; Pugh, H.; Nightingale, J.; Kim, J.-S.; Williams, S. *J Raman Spectrosc.* **2019**, *50*, 1527–1536.

(26) Faurel, X.; Vanderperre, A.; Colomban, P. *J Raman Spectrosc.* **2003**, *34(4)*, 290–294.

(27) Stürzl, N.; Sergei Lebedkin, S.; Klumpp, S.; Hennrich, F.; Kappes, M. *Anal. Chem.* **2013**, *85(9)*, 4554–4559.

(28) Liu, X.-L.; Liu, H.-N.; Tan, P.-H. *Review of Scientific Instruments* **2017**, *88*, 083114.

(29)   Adar, F.; Gouterman, M.; Aronowitz, S. *J. Phys. Chem.* **1976**, *80(20)*, 2184–2191.

(30)   Tuschel, D. *Spectroscopy* **2018**, *33(12)*, 12–19.

(31)   Hassing, S.; Jernshøj, K. *Food Analysis* **2014**, *25(2)*, 63–69.

(32)   López-Peña, I.; Leigh, B.; Schlamadinger, D.; Kim, J. *Biochemistry* **2015**, *54(31)*, 4770–4783.

(33)   Asamoto DK, K. J. *Methods Mol Biol.* **2019**, *2003*, 327–349.

(34)   Wen, Z.; Thomas, G. J. *Biopolymers* **1998**, *45(3)*, 247–56.

(35)   Cheng, J.-X.; Xie, X. *Science* **2015**, *350(6264)*.

(36)   Nebu, J.; Sony, G. In *Spectroscopic Methods for Nanomaterials Characterization Micro and Nano Technologies*; Elsevier: 2017; Chapter 5 - Raman Spectroscopy, pp 95–127.

(37)   https://nam.epfl.ch/research/11.html.

(38)   Freestone, I.; Meeks, N.; Sax, M.; Higgitt, C. *Gold Bull* **2007**, *40(4)*, 270–277.

(39)   https : / / britishmuseum . tumblr . com / post / 120689869617 / the - lycurgus-cup.

(40)   Willets, K.; Van Duyne, R. *Annu.Rev. Phys. Chem.* **2007**, *58*, 267–97.

(41)   Tay, L. In *Encyclopedia of Color Science and Technology*; Springer: New York, NY, 2016.

(42)   Fang, Y.; Sun, M. *Light Sci Appl* **2015**, *4*, e294.

(43)   Englebienne, P.; Hoonacker, A.; Verhas, M. *Journ Spect* **2003**, *17*, 255–273.

(44)   Maier, S., *Plasmonics: Fundamentals and Applications*, 1st ed.; Springer-Verlag US: 2007.

(45)   Maradudin, A.; Sambles, J.; Barnes, W. In *Handbook of Surface Science*; Elsevier: 2014.

(46)   Wang, Y.; Yu, J.; Mao, Y., et al. *Nature* **2020**, *581*, 401–405.

(47) Baburin, A. et al. *Optical Materials Express* **2019**, *9(2)*, 611–642.

(48) Kolwas, K.; Derkachova, A. *Opto-Electronics Review* **2010**, *18(4)*, 429–437.

(49) Rasskazov, I. et al. *J. Phys. Chem. C* **2021**, *40*, 611–642.

(50) Mie, G. *Ann. Phys.* **1908**, *330*, 377–445.

(51) https://nanocomposix.com/pages/silver-nanoparticles-optical-properties#target.

(52) Linic, S.; Christopher, P.; Ingram, D. *Nature Materials* **2011**, *10*, 911–921.

(53) Harris, N.; Blaber, M.; G.C., S. In *Encyclopedia of Nanotechnology*; Springer, Dordrecht: 2016.

(54) Agrawal, A.; Kriegel, I.; Milliron, D. *Chemical Society Reviews* **2015**, *119(11)*, 6227–6238.

(55) Li, X.; Chen, T.; Liu, Y.; Leong, K. *Opt Express.* **2014**, *22(5)*, 5124–32.

(56) Ghosh, S.; Pal, T. *Chem. Rev.* **2007**, *107*, 4797–4862.

(57) Nordlander, P.; Oubre, C.; Prodan, E.; Li, K.; Stockman, M. *Nano Letters* **2004**, *4(5)*, 899–903.

(58) Zhu, W. et al. *Nature Communications* **2016**, *7(11495)*.

(59) Sur, U. *Advances in nano research* **2013**, *1(2)*, 111–124.

(60) Pilot, R.; Signorini, R.; Durante, C.; Orian, L.; Bhamidipati, M.; Fabris, L. *Biosensors* **2019**, *9(57)*.

(61) Jensen, L.; Aikensb, C.; Schatzc, G. *Chem. Soc. Rev.* **2008**, *37*, 1061–1073.

(62) Pérez-Jiménez, A.; Lyu, D.; Lu, Z.; Liu, G.; Ren, B. *Chem. Sci.* **2020**, *11*, 4563–4577.

(63) Fateixa, S.; Nogueira, H.; Trindade, T. *Phys. Chem. Chem. Phys.* **2015**, *17*, 21046–21071.

(64) Guillot, N.; Lamy de la Chapelle, M. *Journal of Quantitative Spectroscopy and Radiative Transfer* **2012**, *113(18)*, 2321–2333.

(65) Stiles, P.; Dieringer, J.; Shah, N.; Van Duyne, R. *Nature Protocols* **2019**, *14*, 1169–1193.

(66) Kovacs, G.; Loutfy, R.; Vincett, P.; Jennings, C.; Aroca, R. *Langmuir* **1986**, *2(6)*, 689–94.

(67) Compagnini, G.; Galati, C.; Pignataro, S. *Phys. Chem. Chem. Phys.* **1999**, *1*, 2351–2353.

(68) Masango, S. et al. *Nano Lett.* **2016**, *16(7)*, 4251–4259.

(69) Ding, S.-Y. et al. *Nature Reviews Materials* **2016**, *1(16021)*.

(70) Wessel, J. *J. Opt. Soc. Am. B* **1985**, *2*, 1538–1541.

(71) Hayazawa, N.; Inouye, Y.; Sekkat, Z.; Kawata, S. *Opt Commun* **2000**, *183*, 333–336.

(72) Pettinger, B.; Picardi G. Schuster, R.; Ertl, G. *Electrochemistry* **2000**, *68(12)*, 942–949.

(73) Stockle, R.; Suh, Y.; Deckert, V.; Zenobi, R. *Chem. Phys. Lett.* **2000**, *318*, 131–136.

(74) Anderson, M. *Appl. Phys. Lett.* **2000**, *76*, 3130–3132.

(75) Zhang, Z.; Sheng, S.; Wang, R.; Sun, M. *Anal. Chem.* **2016**, *88*, 9328–9346.

(76) Vasconcelos, T. et al. *IEEE Journal of Selected Topics in Quantum Electronics* **2020**, *PP*, 1–1.

(77) Shi, X. et al. *Chem. Rev.* **2017**, *117*, 4945–4960.

(78) Novotny, L. *Phys. Rev. Lett.* **2007**, *98(26)*, 266802.

(79) Rendell, R.; Scalapino, D. *Phys. Rev. B: Condens. Matter Mater. Phys.* **1981**, *24*, 3276.

(80) Becker, S. et al. *ACS Photonics* **2016**, *3*, 223–232.

(81) Richard-Lacroix, M.; Yao Zhang, Y.; Dong, Z.; Deckert, V. *Chem. Soc. Rev.* **2017**, *46*, 3922–3944.

(82) Stalder, M.; Schadt, M. *Optics Letters* **1996**, *21(23)*.

(83) Wang, J.; Wu, X.; Wang, R.; Zhang, M. In *Electronic Properties of Carbon Nanotubes*; IntechOpen: 2011.

(84) Kumar, N. et al. *Nature Protocols* **2019**, *14*, 1169–1193.

(85) Stadler, J.; Schmid, T.; Zenobi, R. *Nanoscale* **2012**, *4*, 1856.

(86) Deckert-Gaudig, T. et al. *Chem. Soc. Rev.* **2017**, *46*, 4077–4110.

(87) Green, J. Table Comparison: Physical Vapor Deposition Vs. Chemical Vapor Deposition, https://www.sputtertargets.net/blog/table-comparison-physical-and-chemical-vapor-deposition.html, September 19, 2019.

(88) Baptista, A.; Silva, F.; Porteiro, J.; Míguez, J.; Pinto, G. *Coatings* **2018**, *8(11)*.

(89) https://www.horiba.com/en_en/applications/materials/nonmetallic-minerals/coatings/gdoes-the-analytical-companion-tool-for-magnetron-sputtering-deposition/.

(90) Greene, J. *Journal of Vacuum Science and Technology A: Vacuum, Surfaces, and Films.* **2017**, *35(5)*.

(91) Kelly, P. J.; Arnell, R. D. *Vacuum* **2000**, *56(3)*, 159–172.

(92) https://qd-europe.com/at/en/product/sputter-coater-with-large-sample-chamber/.

(93) Alves, C.; Yang, Y.; Carnes, D.; Ong, J.; Sylvia, V.; Dean, D.; Agrawal, C.; Reis, R. *Biomaterials* **2007**, *28*, 307–315.

(94) De Valence, S.; Tille, J.-C.; Chaabane, C.; Gurny, R.; Bochaton-Piallat, M.-L.; Walpoth, B.; Moller, M. *European Journal of Pharmaceutics and Biopharmaceutics* **2013**, *85(1)*, 78–86.

(95) Jung, C.; Kang, D.; Hwang, I.; Choi, J.; Lee, J.; Jang, J.; Shin, K. *J. Nanosci. Nanotechnol.* **2014**, *14*, 6158–6161.

(96) Kong, X.; Xu, Y.; Cui, Z.; Li, Z.; Liang, Y.; Gao, Z.; Zhu, S.; Yang, X. *Appl. Catal. B* **2018**, *230*, 11–17.

(97) Winkler, K.; Wojciechowski, T.; Liszewska, M.; Gorecka, E.; Fialkowski, M. *RSC Adv.* **2014**, *4*, 12729.

(98) Nishihara, Y.; Chikamatsu, M.; Kazaoui, S.; Miyadera, T.; Yoshida, Y. *Japanese Journal of Applied Physics* **2018**, *57*, 04FS07.

(99) Chen, C. *Journal of Adhesion Science and Technology* **2018**, *32*, 1239–1252.

(100) Lycans, R.; Higgins, C.; Tanner, M.; Blough, E.; Day, B. *Colloid. Surface. B* **2014**, *116*, 687–694.

(101) Mehdizadeh, M., *Microwave/RF Applicators and Probes*, 2nd ed.; Elsevier Inc.: 2015, pp 335–363.

(102) https://belab.ust.hk/images/plasma%20cleaner/plasma_cleaner.htm.

(103) Lieberman, M. A.; Lichtenberg, A. J., *Principles of Plasma Discharge and Materials Processing*, 2nd ed.; John Wiley and Sons Inc.: 2005, pp 461–490.

(104) Okumura, T. *Physics Research International* **2010**.

(105) D'Agostino, R.; Favia, P.; Kawai, Y.; Ikegami, H.; Sato, N.; Arefi-Khonsari, F., *Advanced Plasma Technology*, 2nd ed.; Wiley-VCH: 2008, pp 99–115.

(106) Eaton, P.; West, P., *Atomic Force Microscope*, 1st ed.; Oxford University Press Inc.: 2010.

(107) Sanders, W., *Atomic Force Microscopy: Fundamental Concepts and Laboratory Investigation*, 1st ed.; CRC Press: 2019.

(108) Haugstad, G., *Atomic Force Microscopy: Understanding Basic Modes and Advanced Applications*, 1st ed.; Wiley: 2012.

(109) Taguchi, A.; Yu, J.; Saitoh, K. In *Reference Module in Materials Science and Materials Engineering*; Elsevier Inc: 2008.

(110) Schadt, M.; Helfrich, W. *Appl. Phys. Lett.* **1971**, *18(127)*.

(111) http://www.arcoptix.com\radial_polarization_converter.htm.

(112) https://www.bellevuecollege.edu/wp-content/uploads/sites/140/2014/06/161lab_BeersLawUpdatedPSGF-2-4-2016.pdf.

(113) https://people.bath.ac.uk/gp304/uv/PerkinElmer_Lambda35_manual_EN.pdf.

(114) *Technical Guide: Reflectance Materials and coatings*; Labsphere.

(115) https://www.perkinelmer.com/lab-solutions/resources/docs/APP_UseofUVVisNIRinDevelopmentPV.pdf.

(116) Leng, Y., *Materials Characterization - Introduction to Microscopic and Spectroscopic Methods*, 2nd ed.; Wiley-VCH: 2013.

(117) Altuhaf, F.; O'Sullivan, C.; Cavarretta, I. *Journal of Geotechnical and Geoenvironmental Engineering* **2013**, *139(8)*.

(118) Zhao, C.; Qiao, Y. *Nanoscale* **2016**, *8*, 17658.

(119) https://www.horiba.com/en_en/products/detail/action/show/Product/ters-probes-1634/.

(120) https://www.brukerafmprobes.com/c-322-tip-enhanced-raman-spectroscopy-ters.aspx.

(121) Shao, F.; Zenobi, R. *Anal. Bioanal. Chem.* **2019**, *411(1)*, 37–61.

(122) Taguchi, A.; Yu J. Prabhat Verma, P.; Kawata, S. *Nanoscale* **2015**, *7*, 17424–17433.

(123) Kim, D. et al. *Nanoscale* **2020**, *9(9)*, 2989–2996.

(124) Dill, T. *ACS Nano* **2016**, *10*, 7523–7531.

(125) Geddes, C., *Reviews in Plasmonics*; Springer: 2017.

(126) Thompson, C. *Annu. Rev. Mater. Res.* **2012**, *42*, 99–434.

(127) Ye, J.; Zuev, D.; Makarov, S. *International Materials Reviews* **2019**, *64(8)*, 439–477.

(128) Milewska, A. et al. *Thin Solid Films* **2019**, *10(12)*, 6172–6188.

(129)   Bhalla, N. et al. *Nanomaterials* **2019**, *9(11)*, 1530.

(130)   Pandey, P.; Kunwar, S.; Lee, J. *J. Alloys Compd.* **2020**, *813*, 152193.

(131)   Gentili, D.; Foschi, G.; Valle, F.; Cavallini, M.; Biscarini, F. *Chem. Soc. Rev.* **2012**, *41*, 4430–4443.

(132)   Lkhamsuren, G.; Mochizuki, M.; Suthiwanich, K.; Hayashi, T. *Thin Solid Films* **2017**, *636*, 478–484.

(133)   Phan L.T. andYoon, S.; Moon, M.-W. *Polymers* **2017**, *9(9)*, 417.

(134)   Okeil, S.; Schneider, J. *Beilstein J. Nanotechnol.* **2018**, *9*, 2813–2831.

(135)   Choe, H.; Kwon, S.-H.; Choe, C.; Lee, J.-J.; C.-H., W. *Thin Solid Films* **2016**, *620*, 165–169.

(136)   El Mel, A.-A. et al. *Nanoscale* **2016**, *8*, 141–148.

(137)   Rooij, A. *Mat. Science* **1989**, *13*, 363–389.

(138)   Smigelskas, A.; Kirkendall, E. *Trans. AIME* **1947**, *171*, 130142.

(139)   Nakamura, R.; Nakajima, H. In *Nanowires-Implementations and Applications*, Hashim, A., Ed.; Intech Open: 2011.

(140)   El Mel, A.-A. et al. *J. Phys. Chem. C* **2017**, *121*, 19497–19504.

(141)   Ji, D. et al. *Angewandte Chemie* **2019**, *131(39)*, 13978–13982.

(142)   Tua, K.; Gösele, U. *Appl. Phys. Lett.* **2005**, *86(9)*, 093111.

(143)   El Mel, A.-A.; Ryusuke Nakamura, R.; Bittencourt, C. *Beilstein J. Nanotechnol.* **2015**, *6*, 1348–1361.

(144)   Zhao, Y. et al. *J. Phys. Chem. C* **2019**, *123*, 19572–19578.

(145)   Altomare, M.; Nguyena, N.; Schmuki, P. *Chem. Sci.* **2016**, *7*, 6865.

(146)   Leroy, F. et al. *Surface Science Reports* **2016**, *7*, 391–409.

(147)   Mullins, W. *Journal of Applied Physics* **1957**, *28(3)*, 333–339.

(148)   Srolovitz, D.; Safran, S. *J. Appl. Phys.* **1986**, *60*, 255–60.

(149)   Cahn, J. *Acta Metallurgica* **1961**, *9(9)*, 795–801.

(150)   Vrij, A. *Discuss. Faraday Soc.* **1966**, *42*, 23–33.

(151) Xie, R.; Karim, A.; Douglas, J.; Han, C.; Weiss, R. *Phys. Rev. Lett.* **1998**, *81(6)*, 1251–1254.

(152) Tsui, O. et al. *Proc. 2nd Croucher ASI on Nano Science and Technology* **2003**, *Nano Science and technology: novel structures and phenomena*, 187–192.

(153) Vandenbrouck, F.; Valignat, M.; Cazabat, A. *Phys. Rev. Lett.* **1999**, *82*, 2693.

(154) Herminghaus, S. et al. *Science* **1998**, *282(5390)*, 916–919.

(155) Bischof, J.; Scherer, D.; Herminghaus, S.; Leiderer, P. *Phys. Rev. Lett.* **1996**, *77(8)*, 1536–1539.

(156) Krishna, H. et al. *Nanotechnology* **2010**, *21*, 155601.

(157) Repetto, L. et al. *Appl. Phys. Lett.* **2012**, *100*, 223113.

(158) Jamie, E.; Dullens, R.; Aartsa, D. *J. Chem. Phys.* **2012**, *137*, 204902.

(159) Krishna, H. et al. *ACS Nano* **2010**, *5(1)*, 470–476.

(160) Michalak, W.; Miller, J.; Yolcu, C.; Gellman, A. *Thin Solid Films* **2012**, *522*, 473–479.

(161) Salvalaglio, M. *Phys. Rev. Lett.* **2020**, *125*, 126101.

(162) Singh, R. *Physics in Perspective* **2002**, *4*, 399–420.

(163) Repetto, L. *Nucl. Instrum. Meth. Phys. Res. B* **2015**, *354*, 28–33.

(164) Khanna, R.; Sharma, A. *Journal of Colloid and Interface Science* **1997**, *195(1)*, 42–50.

(165) Craster, R.; Matar, O. *Rev. Mod. Phys.* **2009**, *81*, 1131.

(166) Berni, M. et al. *Applied Surface Science* **2019**, *498*, 143890.

(167) Kesarwani, R.; Dey, P.; Khare, A. *RSC Adv.* **2019**, *9*, 7967.

(168) Singh, U. *Phys. Chem. C* **2016**, *120(10)*, 5755–5763.

(169) Of Thin Film Morphology Modeling, E.; Simulations, *Pelliccione, M. and Lu, T.-M.* Springer-Verlag Newe York: 2008.

(170) Semmlow, J. In, 2nd ed.; Elsevier: 2012; Chapter 4 - The Fourier Transform and Power Spectrum: Implications and Applications, pp 131–165.

(171) Goodman, J., *Statistical Optics*; John Wiley and Sons: 1985.

(172) Youngworth, R.; Gallagher, B.; Stamper, B. *Proc. SPIE Vol. 5869, Optical Manufacturing and Testing VI* **2005**.

(173) Jacobs, T. et al. *Surf. Topogr.: Metrol. Prop.* **2017**, *5*, 013001.

(174) Gircys, M.; Ross, B. *Complexity* **2019**, *21*, 5755–5763.

(175) https://www.nanoworld.com/contact-mode-afm-tip-arrow-cont.

(176) https://www.brukerafmprobes.com/p-3844-tespa-v2.aspx.

(177) Yeo, B.-S.; Schmid, T.; Zhang, W.; Zenobi, R. *Anal Bioanal Chem* **2007**, *387*, 2655–2662.

(178) Kumar, N. et al. *Nanoscale* **2018**, *10*, 1815–1824.

(179) Ma, C.; Trujillo, M.; Camden, J. *ACS Appl. Mater. Interfaces* **2016**, *8*, 23978–23984.

(180) Kumar, N. et al. *Phys. Chem. Chem. Phys.* **2016**, *18*, 13710–13716.

(181) Mahapatra, S.; Bogle, K.; Dhole, S.; Bhoraskar, V. *Nanotechnology* **2007**, *18*, 135602.

(182) Waterhouse, G.; Bowmaker, G.; Metson, J. *Phys. Chem. Chem. Phys.* **2001**, *3*, 3838–3845.

(183) Deegan, R. et al. *Nature* **1997**, *389(6653)*, 827–829.

(184) Morovvati, B.; Malekfar, R. *Int. J. Opt. Photonics* **2019**, *13(2)*, 89–96.

(185) Huang, T.-X. et al. *Nanoscale* **2018**, *10*, 4398–4405.

(186) Wang, R.; Kurouski, D. *J. Phys. Chem. C* **2018**, *122(42)*, 24334–24340.

(187) Lee, C. et al. *ACS NANO* **2010**, *4*, 2695–2700.

(188) Du, Z.; Qi, Y.; He, J.; Zhong, D.; Zhou, M. *WIREs Nanomed Nanobiotechnol* **2021**, *13(2)*, e1672.

(189) Ventura, B. et al. *ACS Sens.* **2020**, *5(10))*, 3043–3048.

(190) Sun, Y.; Xia, Y. *Science* **2002**, *298(5601)*, 2176–2179.

(191) Ciou, S.-H. et al. *J. Phys. Chem. C* **2009**, *113(22)*, 9520–9525.

(192) Xu, H. et al. *Plasmonics* **2016**, *11*, 1645–1652.

(193) Koetz, J. *Nanomaterials* **2020**, *10*, 2187.

(194) Mulvihill, M. et al. *J. Am. Chem. Soc.* **2010**, *132(1)*, 268–274.

(195) Lee, H. et al. *Chem. Soc. Rev.* **2019**, *48*, 731.

(196) Liu, Y. et al. *Nano Micro Small* **2014**, *10(23)*, 4940–4950.

(197) Goh, M. et al. *Langmuir* **2012**, *28(40)*, 14441–14449.

(198) Sharma, B. et al. *MRS Bulletin* **2013**, *38(8)*, 615–624.

(199) Thacker, V. et al. *Nat Commun* **2014**, *5*, 3448.

(200) Prinz, J.; Heck, C.; Ellerik, L.; Merk, V.; Bald, I. *Nanoscale* **2016**, *8(10)*, 5612–5620.

(201) Foti, A. et al. *Materials (Basel)* **2018**, *11(3)*, 440.

(202) Xin, K. et al. *Optics Express* **2020**, *28(6)*, 8734.

(203) Formo, E.; Mahurin, S.; Dai, S. *ACS Appl. Mater. Interfaces* **2010**, *2(7)*, 1987–1991.

(204) Tahghighi, M.; Mannelli, I.; D., J.; Ignes-Mullol, J. *Applied Surface Science* **2018**, *447*, 416–422.

(205) Das, G. et al. *Scientific Reports* **2013**, *3*, 1792.

(206) Sivashanmugan, K.; Liao, J.-D.; You, J.-W.; Wu, C.-L. *Sensors and Actuators B* **2013**, *181*, 361–367.

(207) Irene, M.; Rita, W.; Dubravka, J.-S.; Manfred, S. *e-Preservation Science* **2012**, *9*, 1–8.

(208) Pettinger, B. et al. *Angewandte Chemie International Edition in English* **1994**, *33(1)*, 85–86.

(209) Duta, L. et al. *Intechopen* **2015**, DOI: http://dx.doi.org/10.5772/60808.

(210) Uelzen, T.; Müller, J. *Thin Solid Films* **2003**, *434(1-2)*, 311–315.

(211) Udai, B. et al. *J. Phys. Chem. C* **2016**, *120(10)*, 5755–5763.

(212) Kiss, J. et al. *Catalysis Letters* **2019**, *149*, 1441–1454.

(213) Mirzaeiana, M. et al. *Colloids and Surfaces A: Physicochemical and Engineering Aspects* **2017**, *519*, 223–230.

(214) Bai, W., Dong, P., Wu, X., Eds., Surface wettability studies on aligned gold nanorod array substrate, IEEE: 2020.

(215) Park, S.-G. et al. *Adv. Func. Mater.* **2017**, *27(41)*, 1703376.

(216) Jeon, T. et al. *Adv. Func. Mater.* **2016**, *4(11)*, 1893–1900.

(217) http://www.uskino.com/articleshow_113.html#:~:text=The%20theoretical%20maximum%20contact%20angle,and%20the%20%E2%80%9Clotus%20effect%E2%80%9D.

(218) https://commons.wikimedia.org/wiki/File:Contact_angle_microstates.svg.

(219) De Gennes, P.-G.; Francoise Brochard-Wyart, F.; Quere, D., *Capillarity and Wetting Phenomena: Drops, Bubbles, Pearls, Waves*; Springer: 2003.

(220) Bico, J.; Thiele, U.; Quere, D. *Colloids Surf A* **2002**, *206*, 41–46.

(221) Gao, L.; McCarthy, T. J. *Langmuir* **2007**, *23*, 3762–3765.

(222) Yang, J. et al. *Thin Solid Films* **2014**, *562*, 353–360.

(223) Kabza, K.; Gestwicki, J.; McGrath, J. *J Chem Ed* **2000**, *77(1)*, 63–65.

(224) Hebbar, R.; Isloor, A.; Ismail, A. In *Membrane Characterization*, Hilal, N. et al., Eds.; Elsevier: 2017; Chapter 12 - Contact Angle Measurements, pp 219–255.

(225) Stalder, A. *Colloids and Surfaces A: Physicochemical and Engineering Aspects* **2010**, *364*, 72–81.

(226) Dutheil, P. et al. *Elsevier* **2015**, *347*, 101–108.

(227) Fehlner, F.; Mott, N. *Oxidation of Metals* **1970**, *2*, 59–99.

(228) Mirzaeian, M. et al. *Colloids and Surfaces A: Physicochemical and Engineering Aspects* **2017**, *519*, 223–230.

(229) Li, Z. et al. *Nat. Mater.* **2013**, *12(10)*, 925–931.

(230) Forrest, E.; Schulze, R.; Liu, C.; Dombrowski, D. *International Journal of Heat and Mass Transfer* **2015**, *91*, 311–317.

(231) Guo, W. et al. *ACS Nano* **2019**, *13*, 13430–13438.

(232) Mai, Y.; Eisenberg, A. *Chem. Soc. Rev.* **2012**, *41*, 5969–5985.

(233) Shen, Y.; Kim, Y.; Kim, J. *RSC Adv.* **2016**, *6*, 38716–38723.

(234) Zakia, M. et al. *J. Mater. Chem. C* **2019**, *7*, 5051–5058.

(235) Jin, H. et al. *ACS Appl. Mater. Interfaces* **2018**, *10(51)*, 44660–44667.

(236) Zito, G.; Rusciano, G.; Pesce, G.; Malafronte, A.; Di Girolamo, R.; Ausanio, G.; Vecchione, A.; Sasso, A. *Physical Review E.* **2015**, *92*, 050601 (R).

(237) Cho, W.; Kim, Y.; Kim, J. *ACS Nano* **2012**, *6*, 249–255.

(238) Zito, G.; Rusciano, G.; Pesce, G.; Malafronte, A.; Di Girolamo, R.; Ausanio, G.; Vecchione, A.; Sasso, A. *Phys. Rev. E* **2015**, *92(5)*, 050601.

(239) Zito, G.; Rusciano, G.; Pesce, G.; Dochshanov, A.; Sasso, A. *Nanoscale* **2015**, *7*, 8593–8606.

(240) Szekeresl, G.; Kneipp, J. *Front. Chem.* **2019**, *7(30)*.

(241) Managó, S. et al. *ACS Appl. Mater. and Interfaces* **2018**, *10*, 12406–12416.

(242) Funing, C. et al. *Nanotechnology, Biology, and Medicine* **2016**, *12*, 1445–1451.

(243) Vendrell, M. et al. *Trends in Biotechnology* **2013**, *31*, 249–257.

(244) Ilardi, G. et al. *Curr Med Chem* **2014**, *21*, 1569–1582.

(245) Bakker, J. et al. *J. Cell Sci.* **2017**, *130*, 4087–4096.

(246) Du, Z.; Lovly, C. M. *Mol Cancer.* **2018**, *17*, s12943.

(247) Kim, T.; Eberwine, J. *Anal Bioanal Chem.* **2010**, *397*, 3173–3178.

(248)   Sasso, E. et al. *Biomed Res Int.* **2015**, *10*, 674920.

(249)   https://www.sinobiological.com/category/fcm-facs-facs.

(250)   Jolliffe, I.; Cadima, J. *Phil. Trans. R. Soc. A* **2016**, *374*, 20150–202.

(251)   Thomas, G. *Annu. Rev. Biophys. Biomol. Struct.* **1999**, *28*, 1–27.

(252)   https://doi.org/10.1039/D0NR90295K.